ALPHA EMISSION FROM THE INTERACTIONS OF 14-200 MeV NEUTRONS ON CARBON-12

M.R. NCHODU

A thesis submitted to the
University of Cape Town
for the degree of Master of Science

March 1994

ACKNOWLEDGEMENTS

I wish to express my sincere appreciation and gratitude to:

- Professor F.D. Brooks, my supervisor, for his selfless assistance, untiring encouragement and support.
- Messrs Saalih Allie and Andy Buffler for their assistance and guidance.
- The staff of the National Accelerator Centre for their co-operation and use of their facility.
- The students and staff of the University of Cape Town, in particular, Ms M.J. Oliver for introducing me to GNU.
- My family and friends for their encouragements and support
- The Foundation for Research Development and UCT Bursary office for financial assistance.

Abstract

Cross-sections for the production of alpha particles from the ^{12}C(n,α)^{9}Be$_{gs}$ and ^{12}C(n,n')3α reactions were measured for incident neutrons in the energy range 25 to 52 MeV. The measurements were reduced to absolute cross-sections by simultaneously observing deuteron recoils from n-d elastic scattering in the scintillator using D(n,n)D elastic scattering cross-section as a reference standard. Neutron energy was determined by time-of-flight and pulse shape discrimination (PSD) was used to identify and separate alphas and deuterons from other reaction products. The feasibility of distinguishing different mechanisms for the ^{12}C(n,n')3α reaction by means of PSD was also investigated.

Contents

List of Figures

Chapter 1

Introduction

1.1 Background

The interaction of fast neutrons with carbon-12 is of interest to several fields in basic and applied physics. First and foremost, since alpha particles are prominent among the resulting products, n- ^{12}C interactions are a rich source of information about clustering phenomena in nuclei [Sh60, Br70, Ta71, Bu75], a field which is attracting increasing interest at the present time [Buc90, Bu94]. Knowledge of the cross-sections of these interactions is also of great importance in calculations of neutron detection efficiencies of organic scintillators, particularly for $E_n > 10$ MeV. In turn neutron detection efficiencies are important for neutron dosimetry calculations and for determining the release of energy to tissue or tissue equivalent materials. The interaction of fast neutrons with carbon-12 may furthermore be important in radiotherapy where neutron beams are used to radiate tumors in the body.

The interaction of fast neutrons with carbon often leads to the disintegration of the carbon nucleus. The largest contribution to the cross-section of reactions involving fast neutrons with carbon pertains to reactions with alpha particles in the final channel. Apart from neutron capture, reactions leading to alpha particles in the final channel are the only ones present at neutron energies below ~15 MeV [An91]. The two dominant reactions that yield alpha particles are ^{12}C(n,α)^{9}Be$_{gs}$ and ^{12}C(n,n')3α which have Q-values of -5.79 MeV and -7.65 MeV, respectively. Figure 1.1 is a composite energy level diagram for the participating nuclei in the disintegration of ^{12}C when it interacts with neutrons. With the exception of the ground state and the 2^+ state at 4.44 MeV, all excited states of ^{12}C which are populated by inelastic scattering can decay in one or more steps into alpha-particles [Fin85]. Inelastic neutron scattering to the 3^- state (9.64 MeV) is followed by decay into three alpha-particles with more than 99% probability [Me84]. The 12.71

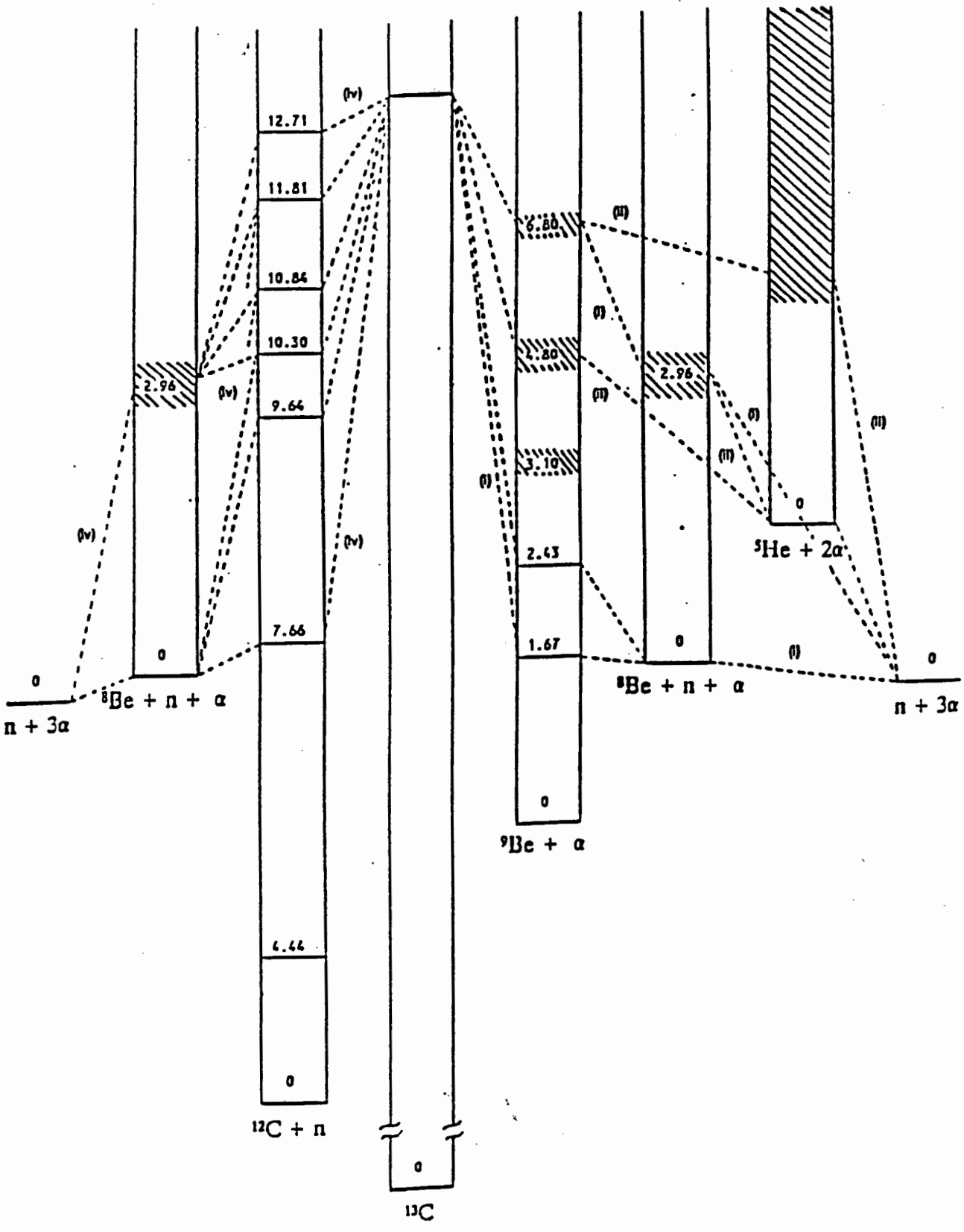

Figure 1.1: *Diagrammatic representation of the energy-levels of the participating nuclei in the neutron-induced sequential break-up of* ^{12}C *showing the possible reaction paths (refer to text). All the energies are in units of MeV.*

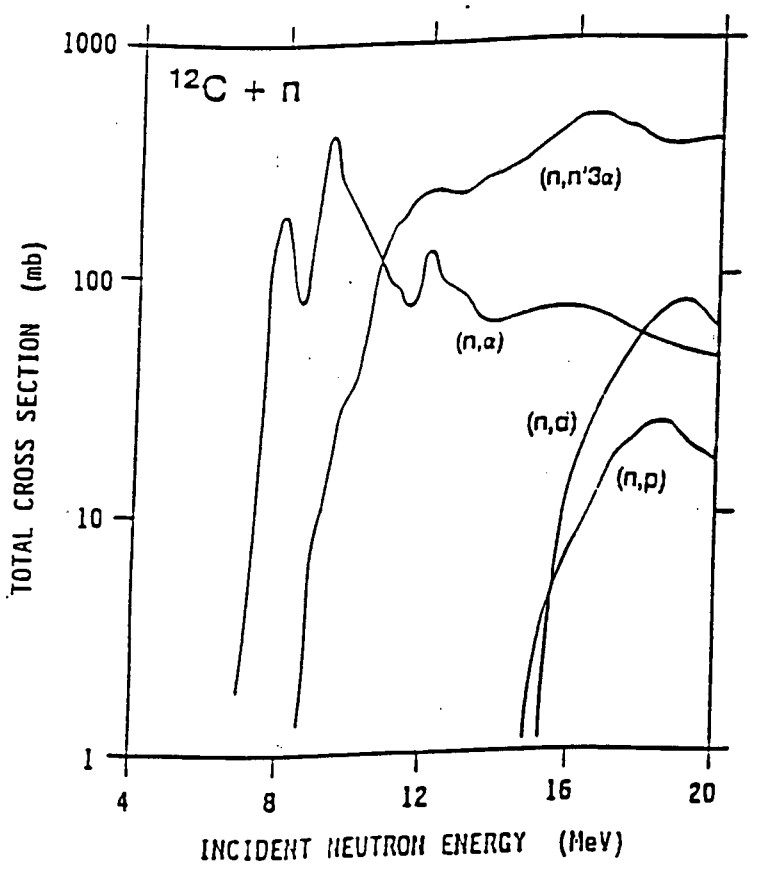

Figure 1.2: *Recommended cross-sections for E_n < 20 MeV for the* ^{12}C(n,p)^{12}B, ^{12}C(n,d)^{11}B, ^{12}C(n,α)^{9}Be *and* ^{12}C(n,n')3α *reactions [La75].*

and 15.1 MeV excited states, however, have a high affinity for gamma decay due to the effect of the tensor force [Ho80]. At neutron-energies below 10 MeV, the ^{12}C(n,α)^{9}Be reaction is dominant [La75, De76]. At higher energies the four-body break-up reaction ^{12}C(n,n')3α contributes strongly to the reaction cross-section. The cross-section for the ^{12}C(n,n')3α reaction is negligible at E_n < 10 MeV, but amounts to more than 20% of the total (n + ^{12}C) cross-section at E_n > 14 MeV [An83]. For E_n > 15 MeV the (n,p) and (n,d) reactions also contribute to the reaction cross-section (see figures 1.2 and 1.3). The large cross-sections of the alpha-producing reactions in the n + ^{12}C interaction may be attributed to the possible existence of alpha clusters in the carbon nucleus.

1.1.1 The Cluster Model of Light Nuclei

It is often useful to describe the structure of light nuclei such as ^{8}Be, ^{12}C, ^{16}O and ^{24}Mg by considering them to be formed of two or more clusters of alpha-particles [Mo56, Ik68, Hor88]. The cluster structure appears generally in the excited states of nuclei. All the excited states in nuclei which are regarded to have the cluster structure have an energy which is near the minimum energy for breakup of the nuclei into clusters [Ik89]. Figure 1.4 is a Ikeda diagram showing some light nu-

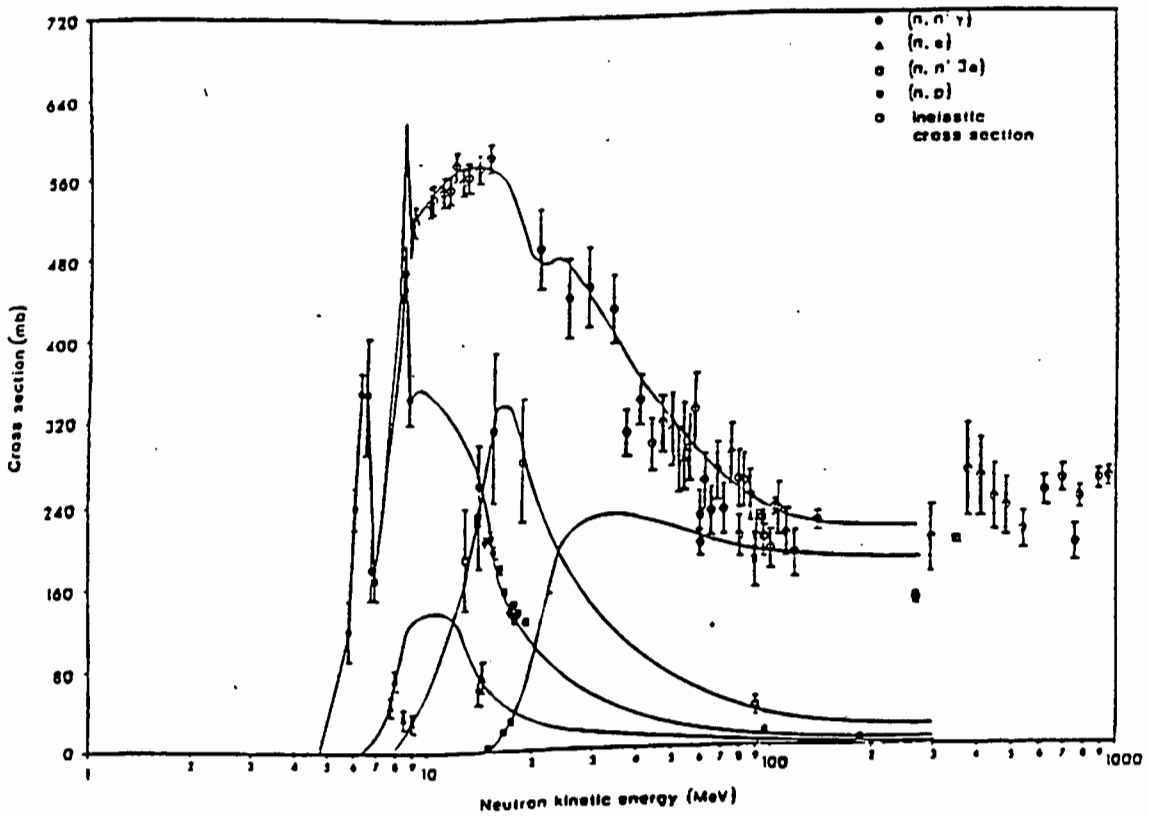

Figure 1.3: *A compilation [De76] of cross-section measurements for neutron-induced reactions on* ^{12}C. *The lines show the cross-section used in a Monte-Carlo program.*

clei with their possible alpha-cluster formations and the minimum energy for the existence of a particular group of clusters. If a well developed cluster structure is to appear, the excitation energy of the nucleus needs to be near or above the minimum energy for breakup of the nucleus into the constituent clusters and be below the top energy of the potential barrier by which the clustering structure is kept to be "loosely bound or quasi-bound" [Ik89]. As the excitation energy gets higher, the probability for formation of clusters also increases (see figure 1.4). The probability of formation of a particular cluster is largely determined by its binding energy. The nucleons will only form a cluster in the nucleus if the internal binding energy of the constituent cluster is stronger than the inter-cluster interaction. This implies that of all possible clusters, the alpha-particle cluster is the most probable. This results from the stabilizing effects of the symmetries in the alpha cluster [Ra88]. The possible existence of these clusters led to the study of the cluster model of nuclei (eg [Sh60, Br70, Ta71, Bu75]). These studies proceed by postulating an appropriate potential for interactions between clusters and then solving the Schrödinger equation to obtain energies of excited states and their wavefunctions. The success of a model is judged by, among other things, its ability to predict the known states of the nuclei [Hod88]. Thus certain excited states of light nuclei, and even the ground state in the case of ^{8}Be, can be thought of as alpha-particles bound together and many of their properties can be accounted for on this assumption. In the cluster model, the ground state of ^{8}Be

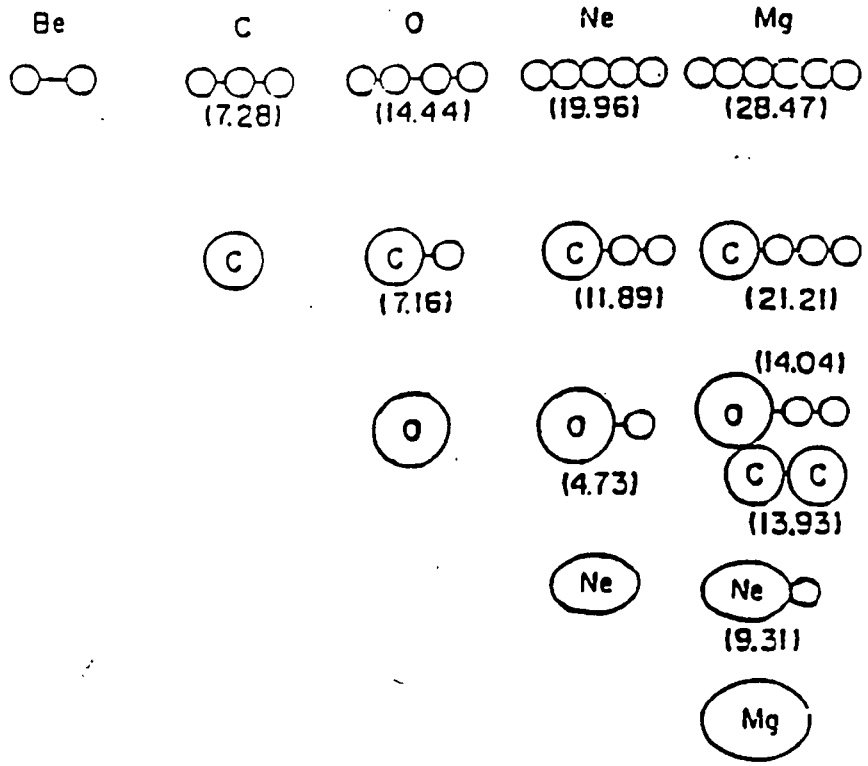

Figure 1.4: *The Ikeda Diagram [Ik68]. The numbers in parenthesis are the minimum energies for the breakup into clusters. All energies are in units of MeV.*

nucleus corresponds to a two-alpha chain, and in ^{12}C, the three-alpha-particle chain has been identified with the 0^+ state at an excitation energy of 7.65 MeV [Br70, Ta71]. The six-alpha-linear chain for the ^{24}Mg nucleus has been predicted by Wuosmaa *et al* [Wu92]. New evidence of alpha clustering in heavy nuclei has also been reported [Buc90, Bu94].

The saturation of the nuclear force turns alpha-clusters into tightly bound groups of four nucleons inside the nucleus. The average binding energy per nucleon between alpha-clusters is much less than that between the nucleons inside such clusters. This reduces the energy required to separate an alpha-cluster from the nucleus. The clustering of alpha-particles will clearly affect cross-section of alpha producing reactions such as (n,α) and (p,α).

1.1.2 Mechanism for Reactions Leading to Alpha Emission from n + ^{12}C

There is only one mechanism which yields a single alpha-particle in the final state of the n + ^{12}C reaction, and that is the ^{12}C(n,α)^{9}Be$_{gs}$ reaction. This reaction,

which has a Q-value of – 5.79 MeV, may be understood as the incident neutron knocking out an alpha particle from the ^{12}C and forming ^{9}Be in the ground state. If ^{9}Be is formed in an excited state it will generally break-up into two alphas and a neutron, rather than de-excite by γ-emission.

The situation regarding the decay to three alpha particles in the final state is less straightforward, however, because it is difficult to separate overlapping reaction channels. There are two main branches of the reaction that proceed via excited states of ^{9}Be and ^{12}C. The alpha particle spectrum for reactions via $^{12}C^{*}$ depends on whether or not the decay proceeds through the ground state or the first excited state of ^{8}Be; this in turn depends upon the state excited in ^{12}C [Pe79]. With reference to figures 1.1 and 1.5 the possible mechanisms leading to triple alpha-emission are:

(i) $^{12}C(n,\alpha)^{9}Be^{*}(n',^{8}Be^{*}(2\alpha))$

(ii) $^{12}C(n,\alpha)^{9}Be^{*}(\alpha,^{5}He^{*}(n',\alpha))$

(iii) $^{12}C(n,^{5}He^{*}(n',\alpha)^{8}Be^{*}(2\alpha)$

(iv) $^{12}C(n,n')^{12}C^{*}(\alpha,^{8}Be^{*}(2\alpha))$

(v) $^{12}C(n,n'\alpha)2\alpha$ (four-body simultaneous break-up)

Due to the emission of four particles in the exit channel, the $^{12}C(n,n')3\alpha$ reaction is rather complex and hence, many details of the reaction will remain hidden unless the kinematic parameters of all the alpha particles are measured simultaneously [An91]. This can be done experimentally with visual detectors such as cloud chambers and nuclear emulsions. A number of experiments have been performed to investigate the mechanism operating in this reaction [Gr49, Pe51, Ja53, Fr55, Br64], and are reviewed in a report by Lachkar *et al* [La75].

Antolkovic *et al* [An75, An76, An83] have investigated the breakup of ^{12}C into three alphas, induced by 10-35 MeV neutrons in a kinematically complete experiment using nuclear emulsions. They calculated the reaction cross-section for the $n + {}^{12}C \rightarrow 3\alpha + n$ break-up and the partial cross-sections for the sequential processes proceeding via the $^{12}C_{9.63}$ and $^{8}Be_{gs}$ intermediate states. The measurement of Antolkovic *et al* [An75] with 14.4 MeV neutrons shows that the 9.64 MeV level of ^{12}C decays entirely through the ground state of ^{8}Be (i and iv

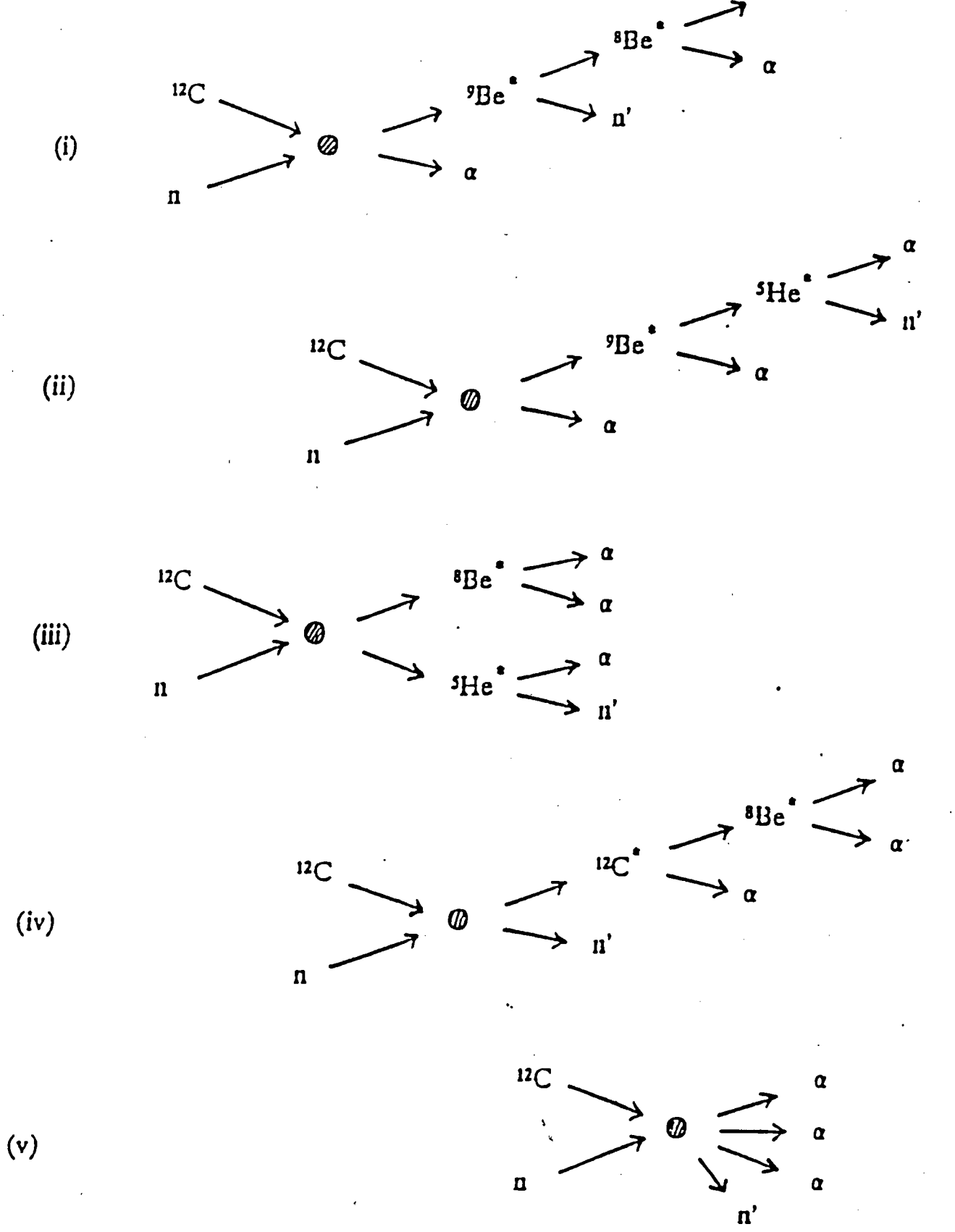

Figure 1.5: *Diagrams representing the neutron-induced sequential break-up of* ^{12}C via: (i) ^{9}Be* *and* ^{8}Be*; (ii) ^{9}Be* *and* ^{5}He*; (iii) ^{8}Be* *and* ^{5}He*; *and* (iv) ^{12}C* *and* ^{8}Be*. *Also shown is the four-body simultaneous break-up* (v).

in figure 1.1). The 12.71 MeV state, on the other hand, decays entirely through the 2.96 MeV level in ^{8}Be, whilst the 10.84 MeV level in ^{12}C decays through both the ground state and 2.96 MeV levels in ^{8}Be (iv in figures 1.1 and 1.5), with the proportions 69% and 31% respectively. The sequential decay ^{12}C(n,α)^{9}Be(n,2α) contributes about 10% at 14.4 MeV and even less at 18.2 MeV [An76]. The conclusions derived in the evaluation by Lachkar [La75] also indicate that the $^{9}Be_{2.43}$ excited state contributes negligibly to the total cross-section for alpha decay of carbon. The percentages of reactions proceeding via this state have been reported [La75, An83] to be 34%, 15%, 11% and 3% for incident neutron energies of 14, 16, 18 and 20 MeV. The three body simultaneous break-up $^{12}C \rightarrow 3\alpha$ cross-section proceeding via the 9.63 MeV state in ^{12}C was measured at neutron energy ranges from 10 to 20 MeV and 20 to 35 MeV [An83] and the contribution to the total alpha production cross-section was found to be (8 ± 4)%. There is no evidence for sequential decay via the ^{5}He states (iii in figure 1.5) [An76, An83].

The sequential decay involving the n + α + $^{8}Be_{gs}$ (or $^{8}Be_{2.9}$) system appears to be the dominant reaction mechanism [An83] in the energy range 10 to 35 MeV. This decay goes hand in hand with the decay through the $^{12}C^{*}$ excited states, since a substantial fraction of the yield proceeding via $^{8}Be_{gs}$ involves an inelastic neutron scattering ^{12}C(n,n')^{12}C and higher excited states of ^{12}C followed by the sequential decay $^{12}C \rightarrow \alpha + {}^{8}$Be. The data from the charge symmetric process ^{12}C(p,p')3α [Ep69] for $E_p = 58$ MeV also show the break-up proceeding mainly by the sequential decay of excited states of ^{12}C.

1.2 Previous Measurements and Calculations

Most of the available ^{12}C(n,α)^{9}Be and ^{12}C(n,n')3α reaction cross-sections come from calculations which utilize nuclear reaction theory. Very few experiments have been performed that provide a test for these calculations. Cloud chamber measurements with 90 MeV neutrons have been made by Kellogg [Ke53] and nuclear emulsion measurements have been made by Frye [Fr55] and Antolkovic *et al* [An75, An76, An83, An91]. Alpha production cross-sections have also been derived indirectly by subtracting the sum of cross-sections for other reactions from the total neutron cross-section (eg [La75, De76, Ha84, An91, Br91]).

Some calculations make use of the optical potential model (eg [Fin85, Me84]), and others use scattering theory in conjunction with the optical model to calculate the alpha production cross-sections. Another calculation is by Brenner

and Prael [Br84] who reanalysed the results of Antolkovic *et al* [An83] and extended the calculation from E_n = 35 MeV to 60 MeV for the ^{12}C(n,n')3α reaction cross-section. They used the intranuclear cascade computer model with Fermi breakup. The details of this model are discussed by Subramanian *et al* [Su83]. This model has been tested and was found to give results which are consistent with the measured experimental results [Br84]. The intranuclear cascade computer model with Fermi breakup is specific to light nuclei in that experimental nuclear structure information (energy, spin, isospin and parity of energy levels, spectroscopic factors and multinucleon clustering, etc) is explicitly included. The overall agreement between the results of Brenner and that of Antolkovic *et al* is good even though the calculated results are systematically lower below ~20 MeV. Figure 1.2 shows the recommended cross-section data for neutron induced alpha production cross-sections up to E_n = 20 MeV. Figure 1.3 shows the cross-section measurements compiled by Del Guerra [De76], and the Monte Carlo fit by Del Guerra [De76] on the data. Figure 1.6 shows the cross-sections measurements and calculations for the ^{12}C(n,n')3α reaction up to E_n = 20 MeV.

1.3 Objectives of This Work

Most of the experiments for the determination of the neutron induced alpha-production cross-sections from carbon-12 are limited to the neutron energy range 7-20 MeV (see figures 1.2, 1.3 and 1.6). There is a shortage of experimental data on the neutron energies above 20 MeV.
The work of Shackleton [Sh70], Stevens [St76] and Buffler [Bu90] has demonstrated the feasibility of using organic scintillators and pulse shape discrimination (PSD) for investigating the neutron-induced alpha-producing reactions from carbon. They used organic scintillators as active targets and PSD to identify and separate the charged particles and reaction products. Figures 1.7a and 1.7b are two parameter plots of counts (vertical) versus pulse height and pulse shape parameter which indicate the use of PSD to identify the different charged particles. The details of this method are presented in section 3.1 and in appendix A. Pauletta [Pa73, Pa75] and Stevens [St76] have shown that the forward recoil deuteron spectra from n-d elastic scattering obtained by utilizing a deuterated organic scintillator can be used to provide accurate calibration in cross-section measurements of this type. In this work the NE230 deuterated liquid scintillator was used as an active target and PSD techniques to measure the neutron-induced alpha production cross-sections.

Figures 1.7a and 1.7b are perspective plots of counts (vertical) versus pulse height, L, and pulse shape parameter, S, measured by an NE213 scintillator for 63 MeV

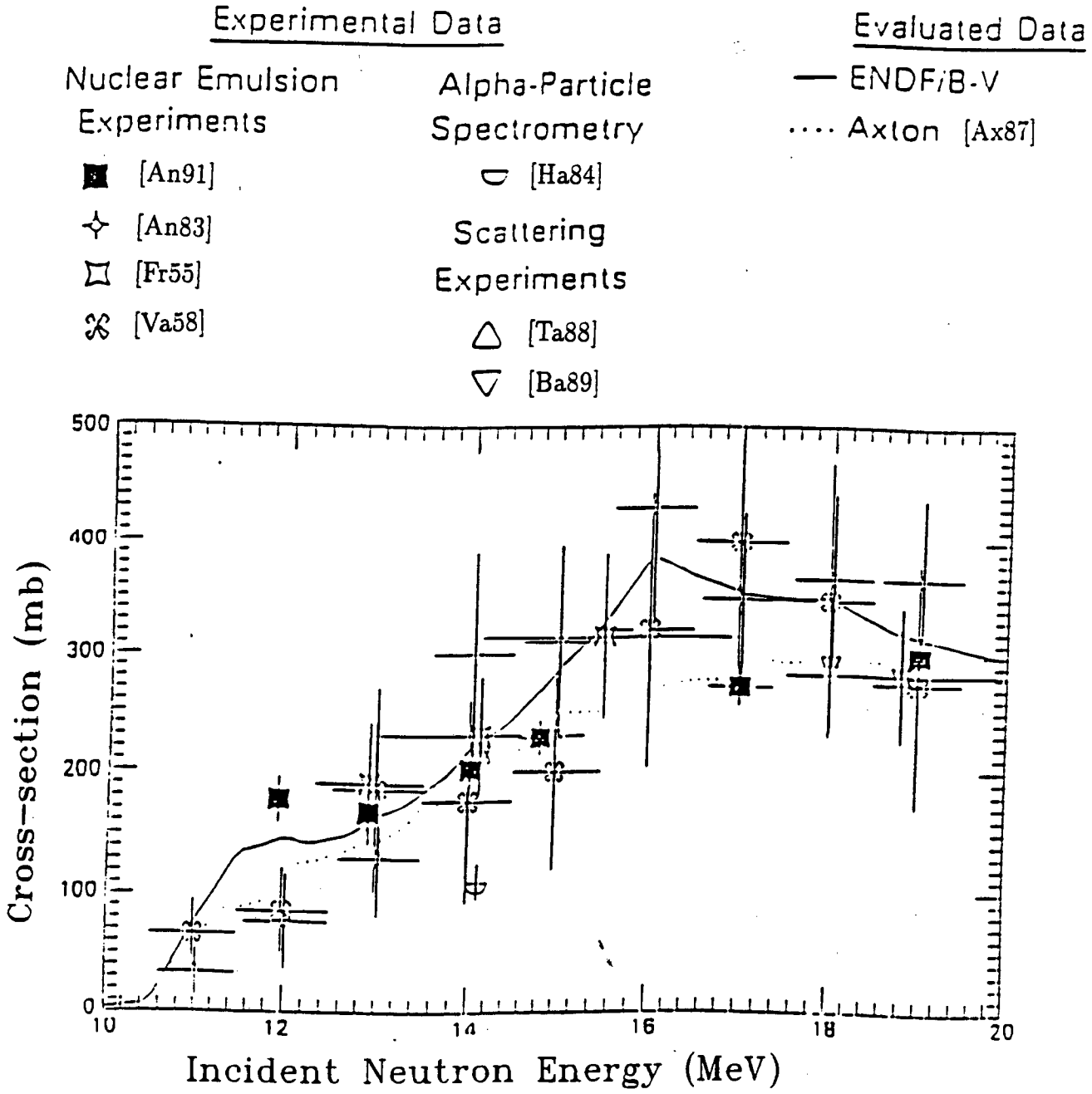

Figure 1.6: *Cross-section [An91] for the* ^{12}C(n,n')3α *reaction with exception of the transition via the 7.65 MeV state.*

neutrons incident on the scintillator. The pulse height is the integral over the fast and the slow component of the scintillation light and the pulse shape parameter relates the ratio of the fast and slow components of the scintillation light. The ridges in figures 1.7a and 1.7b correspond to protons, deuterons and alpha particles. One of the features of the alpha locus is that it is wider than the other loci. The peaks in the alpha locus are associated with the different alpha production reactions. These imply that the alpha particles released from the interaction of neutrons with carbon have different different energy distributions and different pulse shape parameters, S, i.e the alpha particles from the $^{12}C(n,\alpha)^{9}Be$ and $^{12}C(n,n')3\alpha$ reactions have different pulse shape parameters. The scatter plots (see chapter 4) of the pulse height and pulse shape parameter were used in this work to investigate the structure in the loci of the PSD plots.

There is a shortage of experimental data for neutron-induced alpha production from carbon-12 for incident neutron energies above 20 MeV. To the best of our knowledge the only existing experimental data above this energy are the nuclear emulsion measurements of cross-sections for production of alpha particles from the $^{12}C(n,n')3\alpha$ reaction by Antolkovic *et al* [An83] for incident neutron energies up to 35 MeV, which has an uncertainty of about 20% [An83]. There is also the Monte Carlo calculations of Del Guerra [De76] and calculations of Brenner and Prael [Br84] for alpha production cross-sections from $^{12}C(n,n')3\alpha$ reaction using the intranuclear cascade model with Fermi breakup. This experiment will provide a significant increase in data for measurements of alpha production cross-sections from interaction of carbon-12 with neutrons of energy greater than 20 MeV.

The experiment described in this work was conducted to measure the alpha production cross-sections from the $^{12}C(n,\alpha)^{9}Be_{gs}$ and $^{12}C(n,n')3\alpha$ reactions, in the neutron energy range 10-200 MeV. The feasibility of distinguishing different alpha production modes such as $^{12}C(n,\alpha)^{9}Be$ and $^{12}C(n,n')3\alpha$ in the alpha locus in the PSD plane was also investigated. A NE230 deuterated liquid scintillator was used as a ^{12}C and deuteron target and also to measure the pulse height spectra of the alpha particles and deuterons. Measurements were made at different neutron energies to investigate the energy dependence of the reaction cross-section.

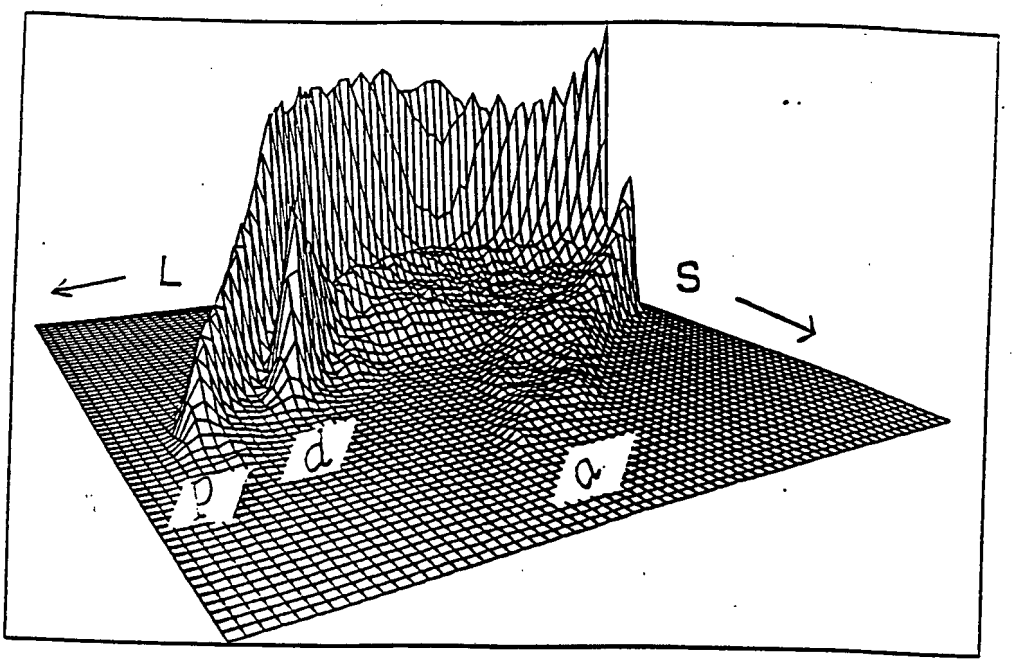

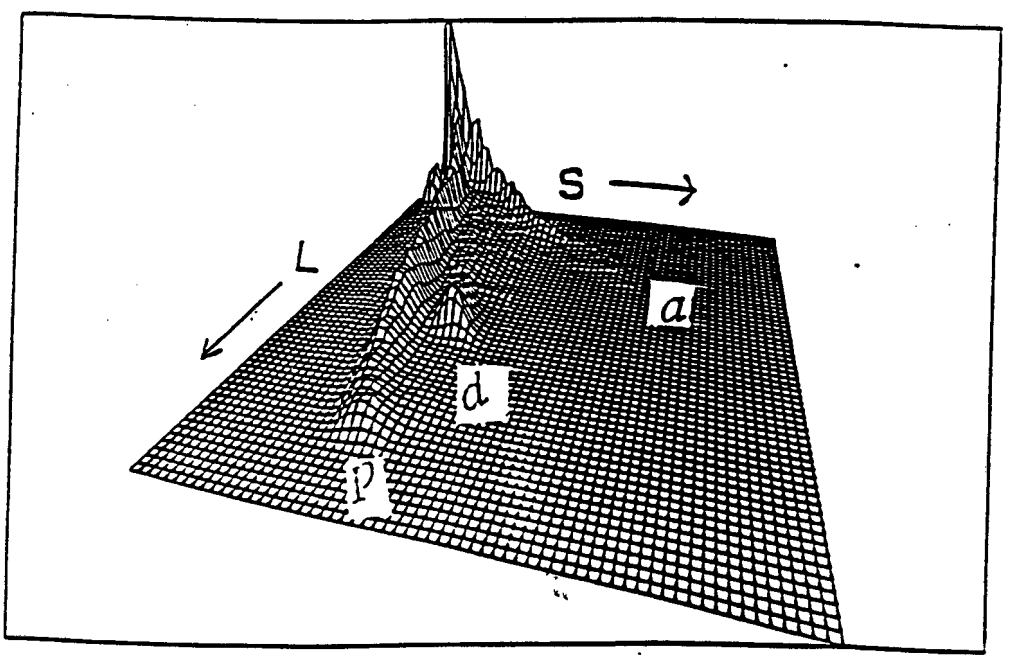

Figure 1.7: *Perspective view of counts (vertical) as a function of pulse height, L, and pulse shape parameter, S, for the events measured by an NE213 scintillator when exposed to quasi-monoenergetic 63 MeV neutrons. The ridges correspond to protons (p), deuterons (d), and alphas (α).*

Chapter 2

The Experimental Set-up

2.1 Experimental Details

2.1.1 Outline

Figure 2.1 is a schematic diagram showing the experimental geometry for the measurement of neutron-induced alpha production cross-sections. Neutrons were produced by the reaction of 66 MeV protons with a 19.6 mm thick ^{9}Be target. Some of these neutrons interacted with nuclei in the NE230 liquid scintillator and some neutrons were scattered out of the NE230 scintillator. Some of the scattered neutrons were detected by the NE213 liquid scintillator (see figure 2.1). The NE230 deuterated liquid scintillator served as a carbon and deuteron target and also as a detector for any charged particles released from the interaction of incident neutrons with nuclei in the scintillator. The energy of neutrons incident on the NE230 scintillator was selected by time-of-flight and the energy of charged particles was deduced from the integrated scintillation output or pulse height (L). A rough measurement of the energy of the scattered neutrons was determined from their times-of-flight between the two scintillators.

The experiment was set up so that singles and coincidence events could be recorded simultaneously. Singles events are those that are detected in the NE230 scintillator regardless of whether a coincidence is detected in the NE213 scintillator. They include events from all possible neutron induced reactions in the scintillator. Some coincidence events arise from ^{12}C(n,n')3α reactions in which the inelastically scattered neutron is detected in the NE213 and the three alphas are detected in the NE230 scintillator (figure 2.2). Another important source of coincidence events is n-d elastic scattering: scattered neutrons are detected in the NE213 scintillator and the associated recoiling deuterons are detected in the NE230. There are also coincidence events from elastically scattered neutrons and recoiling protons from n-p elastic scattering on the small hydrogen content (see

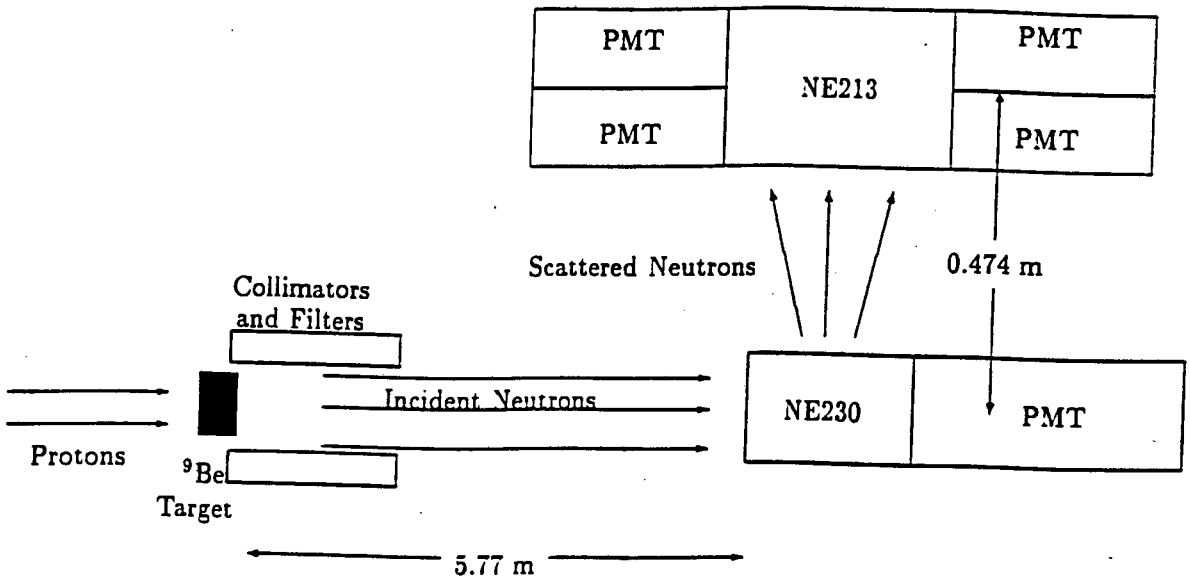

Figure 2.1: *A top view of the experiment (not to scale) showing the geometry of the detectors.*

table 2.1) in the NE230 scintillator. The other source of coincidence involving protons is the deuteron breakup reaction, D(n,2n)H in which NE230 scintillator detects a proton and NE213 scintillator detects a neutron.

The NE213 scintillator was placed out of the well collimated incident neutron beam 0.474 m to the side of NE230 scintillator. The energy resolution for the scattered neutrons was considerably poorer than for the incident neutron because of the shorter flight path used (0.474 m compared to 5.77 m).

2.1.2 Neutron Production

The experiment was conducted in the neutron therapy section of the National Accelerator Centre (NAC), Faure, South Africa. The neutron therapy facility [Nac87, Jo92] consists of an isocentric gantry capable of $\pm 185^0$ rotation and includes a variable aperture collimator providing field sizes from 5 cm x 5 cm to 30 cm x 30 cm at a source to axis distance (SAD) of 150 cm (see figure 2.3). The beamline components in the gantry include 70^0 and 160^0 dipole bending magnets, a quadrupole triplet between the bending magnets, a steering magnet and a beam wobbler system. A beam scanner is fitted between the first two magnets to facilitate beam tuning. The neutrons are produced by the reaction of 66 MeV protons on a 19.6 mm copper-backed ^{9}Be target. The reaction yielding the neu-

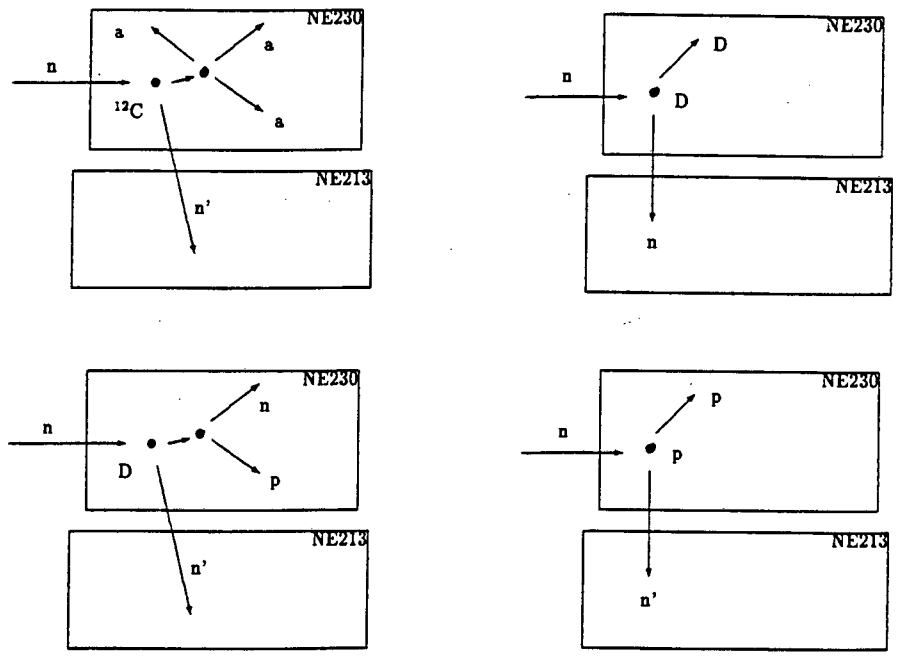

Figure 2.2: *Diagram illustrating the coincidence events in the experiment. The particles shown in the diagram are alphas (a), neutrons (n), protons (p) and deuterons (D).*

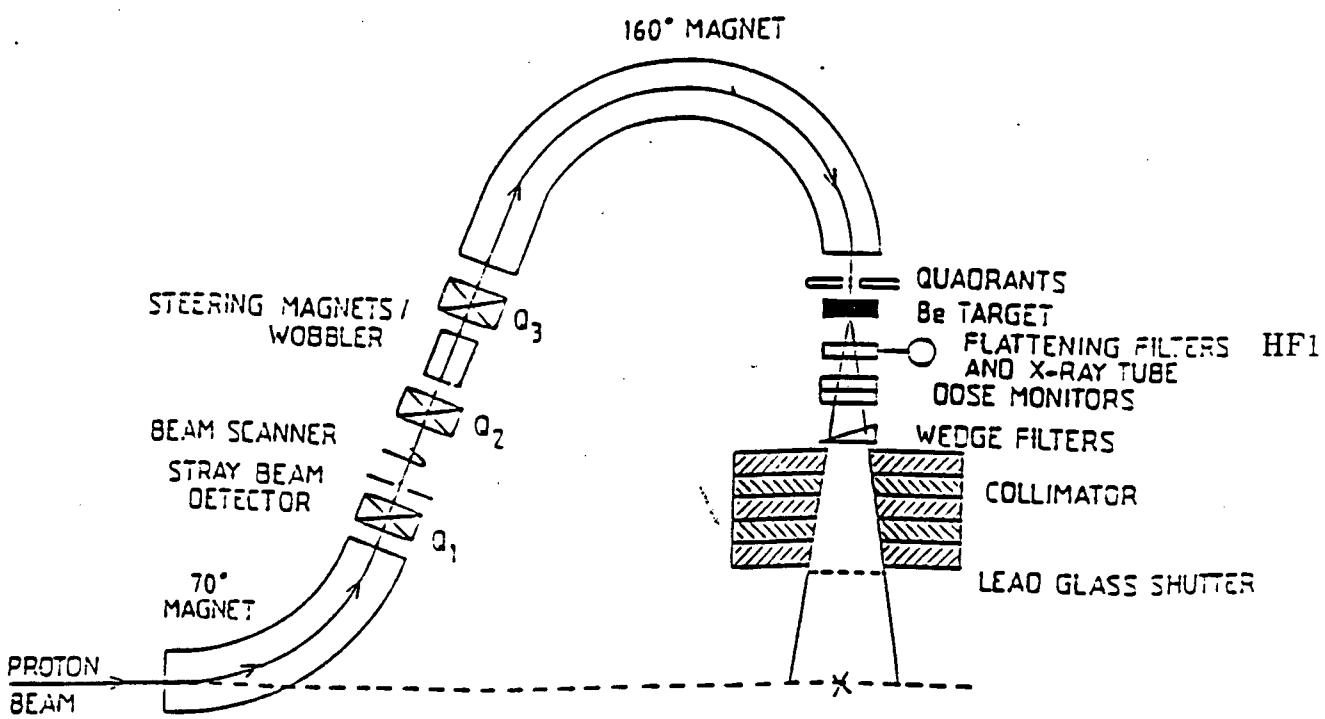

Figure 2.3: *A schematic diagram of the main components of the NAC's neutron therapy system.*

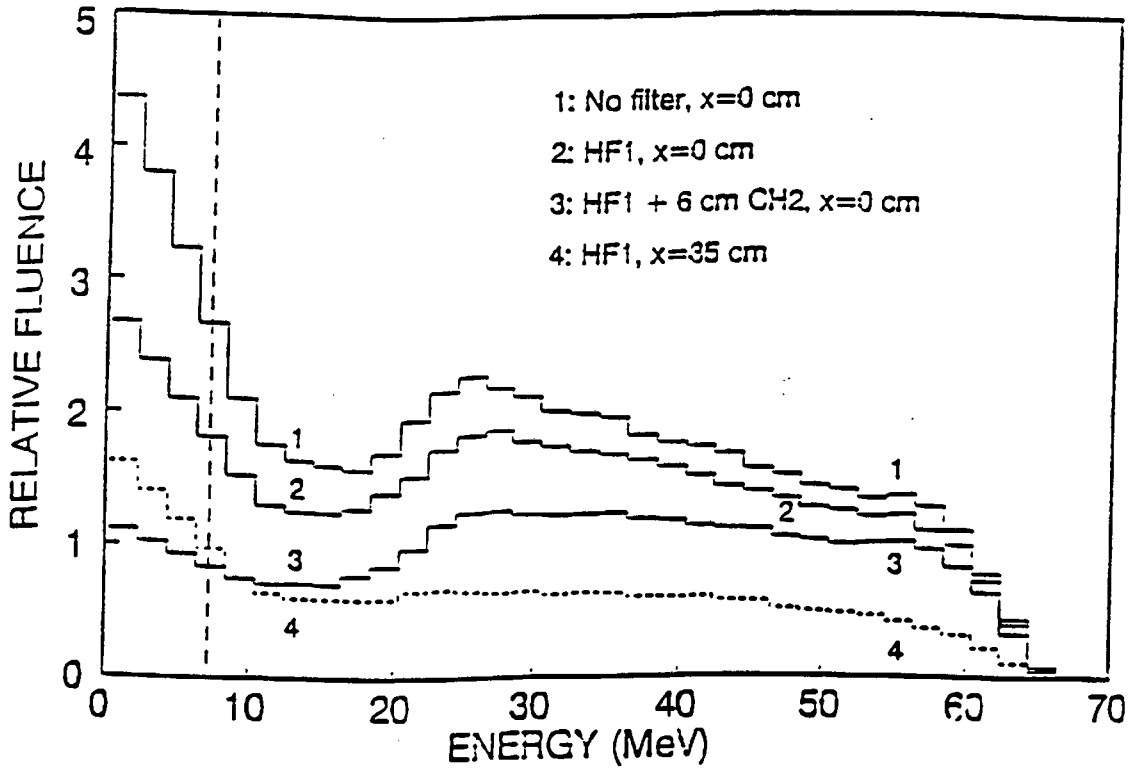

Figure 2.4: *Neutron fluence (number of counts/unit energy) spectrum in a 10 cm* x *10 cm field for various conditions, HF1 is the clinical filter (H = 2.5 cm CH_2, F1 is the iron flattening filter) and* x *is the off-axis distance [Jo92]. The spectra are arbitrarily scaled for clarity. Spectrum 2 is similar to the one used for measurements in this work.*

trons is p + ^{9}Be → n + ^{9}B with the Q-value of -1.85 MeV. The proton beam dissipates 40 MeV of energy in the ^{9}Be target and the remaining energy is deposited on the copper backing. The neutron beam is moderated by 0.8 cm-thick iron flattening filter (F) and a 2.5 cm-thick polyethylene [$(CH_2)_n$] hardening filter (H). The purpose of the flattening filters is to maintain an approximately uniform neutron energy distribution on the field area. The polyethylene filters are used to reduce the number of low energy neutrons (neutrons of energy less than 16 MeV) thereby hardening the beam [Jo92]. Figure 2.4 shows the energy distribution of the neutrons over the energy range and the changes in the neutron distribution for different filters and detection position. In the figure it can be seen that the distribution of the neutrons is almost uniform over the energy range 20-60 MeV and there is a drop in the neutron energy distribution in the region immediately below 20 MeV, and a rise in the region below 10 MeV.

For this experiment the size of the neutron beam was set at 55 mm x 55 mm (at SAD = 150 cm) and the filter combination HF1 (H is a 2.5 cm CH_2 hardening filter and F1 is the iron flattening filter) was used. The neutron energy distribution for this filter combination is almost the same as spectrum-2 in figure 2.4.

Physical Characteristics	NE230	NE213
Mass % of D	14.2	-
Mass % of C	85.7	92.3
Mass % of H	0.1	7.7
No. of H / No. of C Atoms	0.984	1.213

Table 2.1: *Physical Characteristics of the NE230 and NE213 Scintillators [NE].*

The gantry rotation angle was set at 270^0 to provide a horizontal beam. The time reference for the incident neutron time-of-flight was derived from the RF cycle of the injector cyclotron which is operated at a frequency of 16.373 MHz for 66 MeV protons. Pulse selection (1 in 5) was used to give a beam pulse frequency of 3.275 MHz corresponding to pulse separation of 305 ns.

2.1.3 Particle Detection

The NE230 scintillator used in this work was sealed inside a cylindrical capsule of 42 mm diameter and 50 mm length. Since the detector diameter is smaller than the beam width (~55 mm) and, assuming that the beam intensity is uniform across the beam, it can be assumed that the scintillator was being uniformly illuminated by the beam. The relevant physical characteristics of the NE230 scintillator are listed in table 2.1. The window of the capsule was optically coupled to the RCA8850 photomultiplier tube using silicone jelly. The detector was placed 5.77 m from the beryllium target, with front face of the scintillator facing the neutron source.

The NE213 liquid scintillator which is used to detect neutrons scattered by the nuclei in the NE230 scintillator has the dimensions: 7 cm x 13 cm x 13 cm. This scintillator was oriented with the 13 cm x 13 cm side facing the NE230 scintillator, so as to increase the solid angle for accepting neutrons from the NE230. The scintillator was coupled to four RCA8575 photomultiplier tubes to improve light collection. The cables from the anode outputs of the four photomultiplier tubes are connected together to sum the anode signal from the NE213 scintillator. The relevant physical characteristics of this detector are listed in table 2.1.

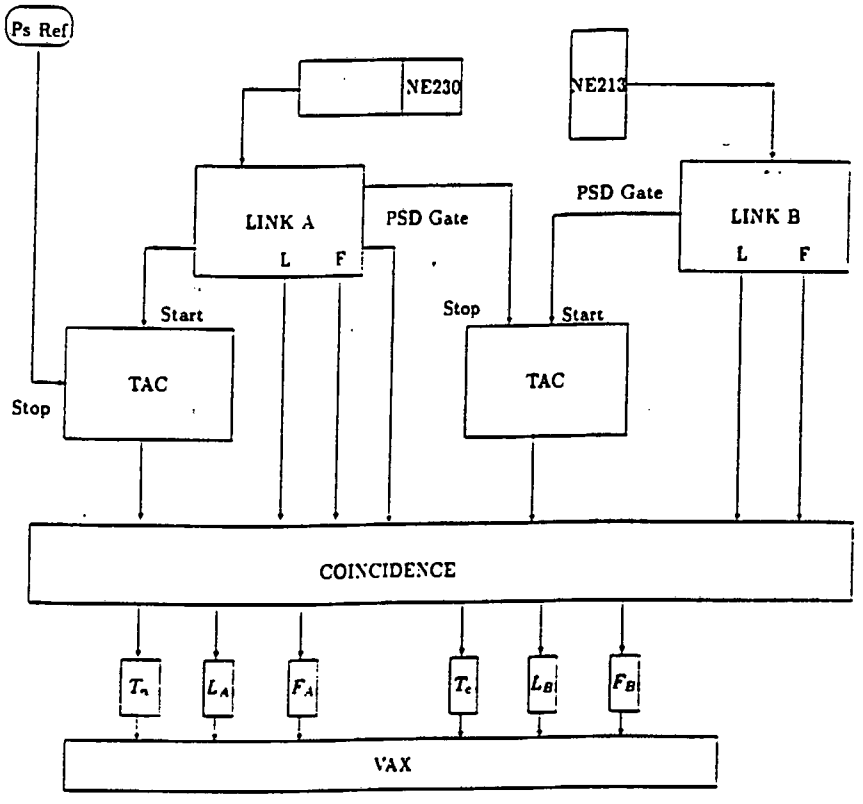

Figure 2.5: *A schematic diagram of the main electronic components for pulse processing in the experiment.*

2.2 Data Acquisition System

Figure 2.5 shows a schematic diagram of the main components of the data acquisition system. A detailed diagram of the electronic configuration of the experiment is shown in figure 2.6. This detector arrangement was used to measure the singles events and the coincidence events simultaneously. For each detector three parameters were recorded: the scintillation pulse height (L) which is the measure of the sum of fast and slow components of the scintillation light, the integral over the fast component of the scintillation pulse (F), and the time-of-flight (T). The output from the anode of the photomultiplier tube of each detector was fed into a LINK model 5010 pulse shape discrimination unit which generated the L and F signals. A modification to the circuit of the LINK has been made in order to provide the F output [Sm86]. The F signal was generated by integrating over the initial 30ns, which is approximately the lifetime of the prompt component of the scintillation decay. The pulse height (L) was generated in the LINK by integrating the scintillation pulse over a period of 500 ns, and thus includes the contribution from both the prompt and the delayed scintillation components. The output from the anode of the photomultiplier tube which is connected to the

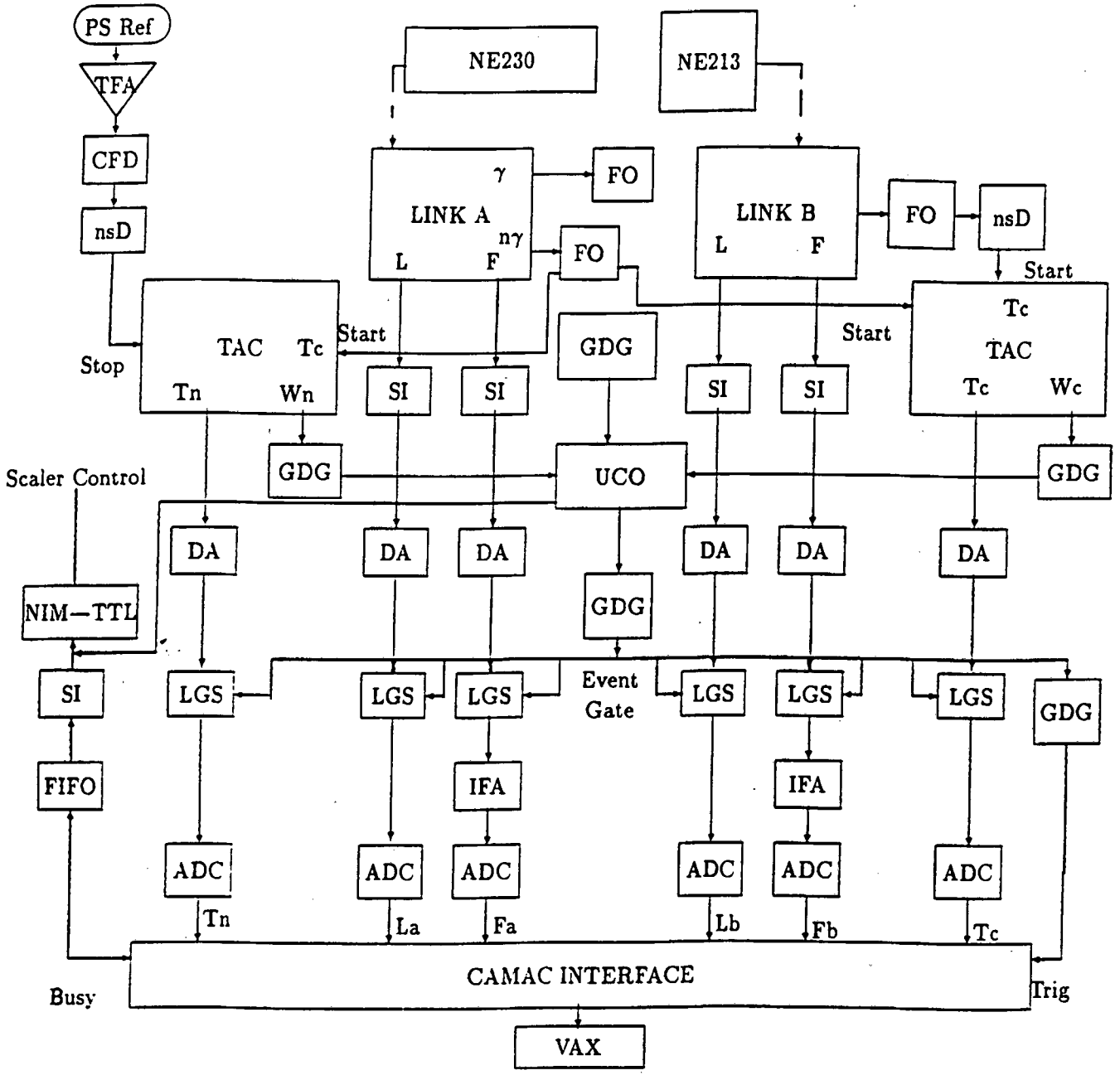

Figure 2.6: *A complete circuit diagram of the electronic configuration for the alpha production experiment. The modules in the diagram are: constant fraction discriminator (CFD), fan out (FO), nanosecond delay (nsD), time to amplitude conveter (TAC), timing filter amplifier (TFA), sum invert (SI), universal coincidence (UCO), gate and delay generator (GDG), delay amplifier (DA), linear gate and stretcher (LGS), fan-in fan-out (FIFO), interface amplifier (IFA), analog to digital conveter (ADC).*

NE230 detector was fed into LINK A, and the anode outputs from the NE213 were fed into LINK B. The outputs γ and n-γ from the LINK modules were used for neutron-gamma discrimination. An event was passed by the coincidence unit whenever there was simultaneously a pulse from the two TAC outputs and the PSD gate from LINK A. The γ logic signal outputs from the LINK modules were used only in the calibration runs.

The incident neutron time-of-flight (T_n) was measured relative to a fixed point in the cyclotron RF cycle. LINK A provided a timing pulse which was used as a start to the time to amplitude converter (TAC), and the beam pulse provided a stop pulse to the TAC. In measuring the scattered neutrons time-of-flight (T_c) spectrum, the timing pulse from the LINK A (the LINK module which processes the pulses from the NE230 scintillator) was used as a start pulse to the TAC and the timing pulse from LINK B (the LINK module which processes pulses from the NE213 scintillator) as a stop pulse.

Six parameters were recorded event by event in the experiment viz. L_A, F_A, T_n (from the NE230) and L_B, F_B (from the NE213) and T_c (coincidence time). These parameters were fed through the ADCs into a VAX computer system where they were recorded on the magnetic tape using the data acquisition code XSYS. All phases of the data were monitored on a system of displays to detect any electronic drifts. The data acquisition was divided into four runs in the same period; three runs of approximately one hour and one run of approximately six hours. There were a number of short calibration runs using gamma ray sources and neutron beam. The analysis of the data was done off-line using the computer program GNU which is available at the University of Cape Town.

The following chapter describes how the measured data were reduced to produce pulse height spectra at different neutron energies, selected by time-of-flight. These spectra were then unfolded into components associated with the emission of different charged particles, identified by pulse shape discrimination to be deuterons and alphas.

Chapter 3

The Experiment

Figure 2.1 shows a schematic diagram of the experiment for measurements of neutron-induced alpha production cross-sections from carbon-12. The energy of the neutrons was determined by the time-of-flight method, with flight paths of 5.77 m and 0.474 m for the incident and scattered neutrons respectively. Pulse shape discrimination was used to identify and to separate the different charged particles and the reaction products. This was achieved by generating L-S spectra (see figure 1.7) for the two detectors and setting up software cuts on the ridges formed in the L-S spectra to separate the different particles. The projections of the events in these cuts onto the L-axis give pulse height spectra of the corresponding particles. Integrals of these spectra were measured for a number of incident neutron energies and used to calculate the alpha production cross-sections relative to the n-d elastic scattering data. Cross-sections were measured for the production of alpha particles from the ^{12}C(n,α)^{9}Be and the ^{12}C(n,n')3α reactions.

The coincidence system was used to identify events from the ^{12}C(n,n')3α reaction by distinquishing them from those due to the ^{12}C(n,α)^{9}Be$_{gs}$ reaction. This was achieved by imposing the coincidence condition that will only accept events when there are signals in both detectors as explained in chapter 2. The selection of the ^{12}C(n,n')3α reaction was further enhanced by using pulse shape discrimination to select events in the NE213 scintillator which are associated with the scattered neutrons.

Prior to the runs the high voltages for the detectors were adjusted to optimise pulse shape discrimination using the cathode ray oscilloscope display ouputs produced by the LINK units, while not introducing notable saturation distortion. This was done using both the weak neutron and gamma ray source (AmBe source) and the neutron beam. The energy calibrations (in units of MeV electron equiv-

alent) were done using the AmBe source under the same conditions as those for the actual measurements.

3.1 Particle Identification

The particles detected were identified by pulse shape discrimination (PSD) (see appendix A). This was achieved by generating the pulse shape parameter (S) from the L and the F outputs from the LINK module. The pulse shape parameter was generated using:

$$S = L - kF + C \tag{3.1}$$

where: L : Sum of the fast and slow components of the scintillation pulse
F : fast component of the scintillation pulse
k,C : arbitrary constants

The constants k and C are chosen to optimise the display. The value of k determines the angle of the loci in the LS distribution as detailed in appendix A, and the value of C determines the position of these loci along the S-axis.

Each type of ionizing particle detected has a particular set of L and S values, and when these are plotted on a plane, the different particles form unique loci, which depend on the type and energy of the particle. The heavier particles are observed to have higher pulse shape parameters (S) than the lighter particles. Figure 3.1 is a perspective plot of counts (vertical) versus L and S, for events measured by the NE230 scintillator for incident neutron energies of 10 to 63 MeV. The events arising from different charged particles detected are seen to lie on well-defined ridges which are resolved on the L-S plane. These ridges are clearly distinguished at higher values of L and S , however with decreasing pulse height, this separation diminishes due to poorer photomultiplier statistics. These ridges as labelled in figure 3.1 are associated with protons from the breakup of the deuterons and carbon nuclei, deuterons from the n-d elastic scattering and from the ^{12}C(n,d)^{11}B reaction and alphas from the reactions (i) ^{12}C(n,α)^{9}Be and (ii) ^{12}C(n,n')3α.

Figure 3.3 is an event scatter plot of counts versus pulse height (L) and pulse shape (S) for the scattered neutrons detected by the NE213 scintillator in coincidence with the events detected in the NE230 scintillator. The ridge with the lower S value (γ in figure 3.3) is associated with gamma rays from the decay of the excited states of carbon populated by inelastic scattering or reaction of incident

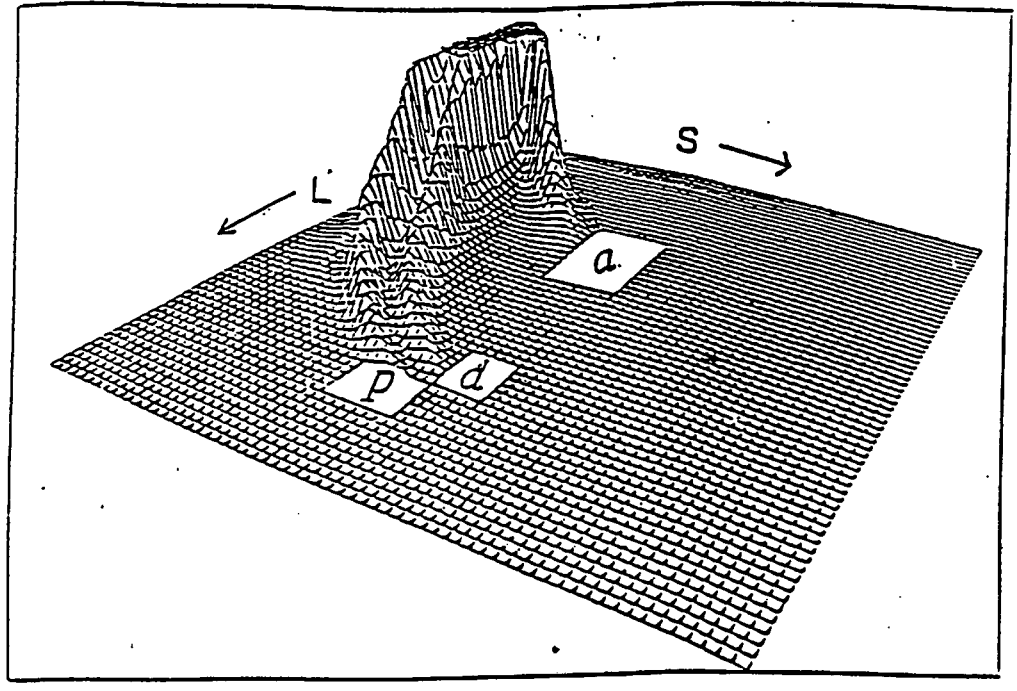

Figure 3.1: *Perspective view of counts (vertical) as a function of pulse height (L) and pulse shape parameter (S) for the singles events measured by an NE230 scintillator when exposed to neutrons of energy range 10-63 MeV. The ridges correspond to protons, p, deuterons, d, and alphas, a. The cut off in the counts scale is caused by limit (max of 8000 counts) imposed on the counts scale when plotting the data.*

neutrons in the NE230 scintillator. The other ridge (p in figure 3.3) is associated with the events in which neutrons which have been inelastically scattered by the nuclei in the NE230 scintillator and then detected in the NE213 scintillator. The events in this ridge are thus mainly recoil protons from elastic scattering of these neutrons in the NE213. The LS spectrum (figure 3.3) for coincidence events detected by the NE213 scintillator is inferior to that of singles events detected by the NE230 scintillator. This could have been caused by bit dropping in the ADC module processing pulses from the L_B parameter (figure 2.5).

3.2 Charged Particle Separation

A computer program GNU - available in the Physics Department, University of Cape Town - allows the user to select events from two parameter spectra such as figures 3.1 and 3.3. A series of points is specified to define the upper and lower limits of the region of interest on the 2D spectrum. The code then fits a smooth curve through these points and the events lying within the region may be selected. Two dimensional corridors were chosen to bound ridges on the L-S spectrum corresponding to alpha particles, deuterons and protons respectively. Figure 3.2

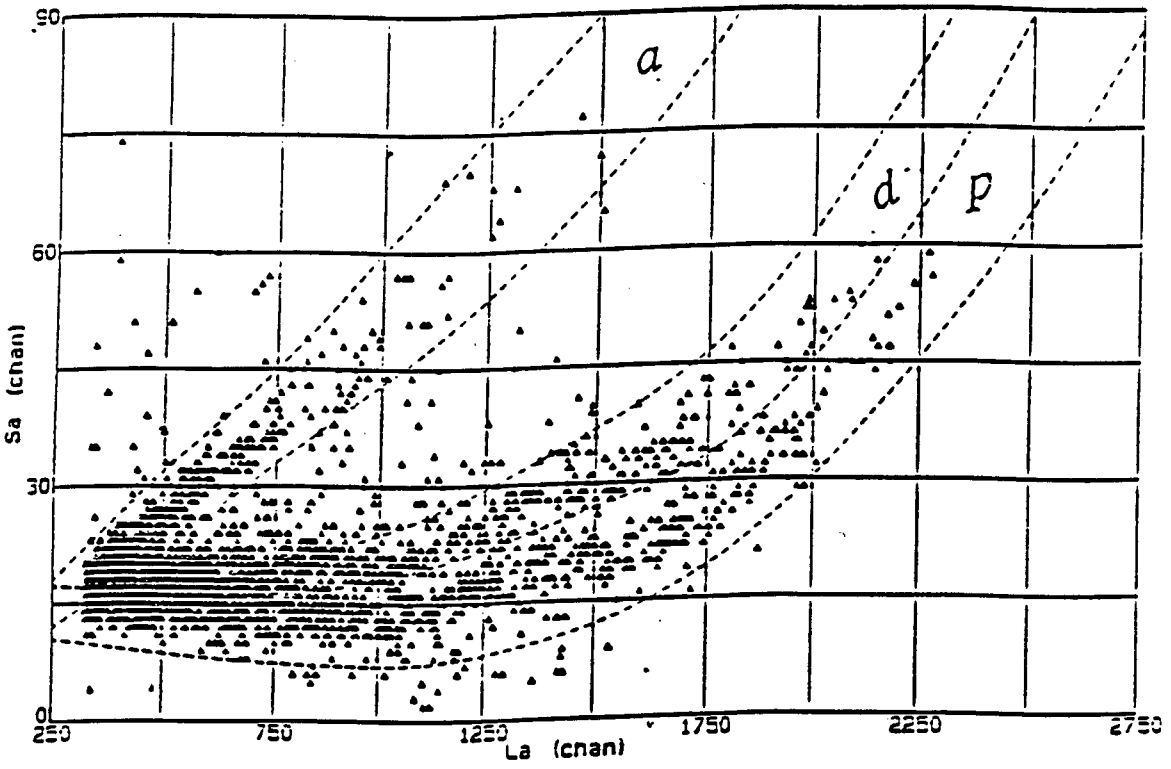

Figure 3.2: *Scatter plot of singles events detected by the NE230 scintillator as a function of pulse height, L, and pulse shape, S. Also shown are the corridors that were set to select events which were identified as protons, deuterons and alphas by pulse shape discrimination.*

illustrates the corridors that were chosen to separate the proton, deuteron and alpha loci, for events measured by the NE230 scintillator. From figure 3.2, it can be seen that the separation between the protons and the deuterons is poor especially at lower pulse heights. The separation between the deuterons and the alpha particles is also poor at lower pulse heights. This could also be due to bit dropping in the ADC module. Thus we expect to find some deuterons in the lower pulse height region of the projected alpha particle spectra and vice versa for the projected deuterons spectra. Figure 3.3 illustrates the corridors that were chosen to separate different types of events indicated by p and γ.

3.3 The Time-of-Flight Spectrum

3.3.1 Incident Neutron Time of Flight Spectrum

Figure 3.4 shows the incident neutron time-of-flight spectrum measured by the NE230 scintillator in this work. The neutrons were produced by the reaction of 66 MeV protons with a 19.66 mm ^{9}Be target, through the ^{9}Be(p,n)^{9}B reaction. The main feature of the spectrum is the broad energy distribution of the neutrons (n in figure 3.4). The neutron edge (t_{nm} in figure 3.4) corresponds to

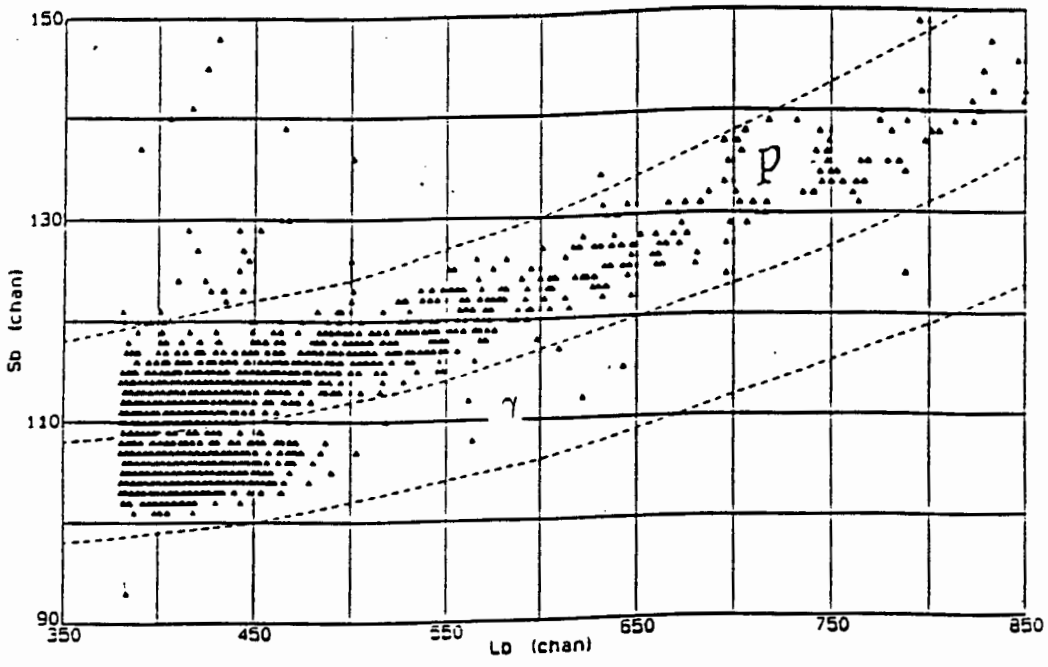

Figure 3.3: *Scatter plot of coincidence events detected by the NE213 scintillator as a function of pulse height, L, and pulse shape, S. These events correspond to particles which are scattered out of the NE230 scintillator and are detected by the NE213 scintillator in coincidence with events detected by the NE230 scintillator. Also shown is the corridor that was set to select events associated with recoil protons from elastic scattering by neutrons which have been scattered out of the NE230 scintillator from the gamma ray events.*

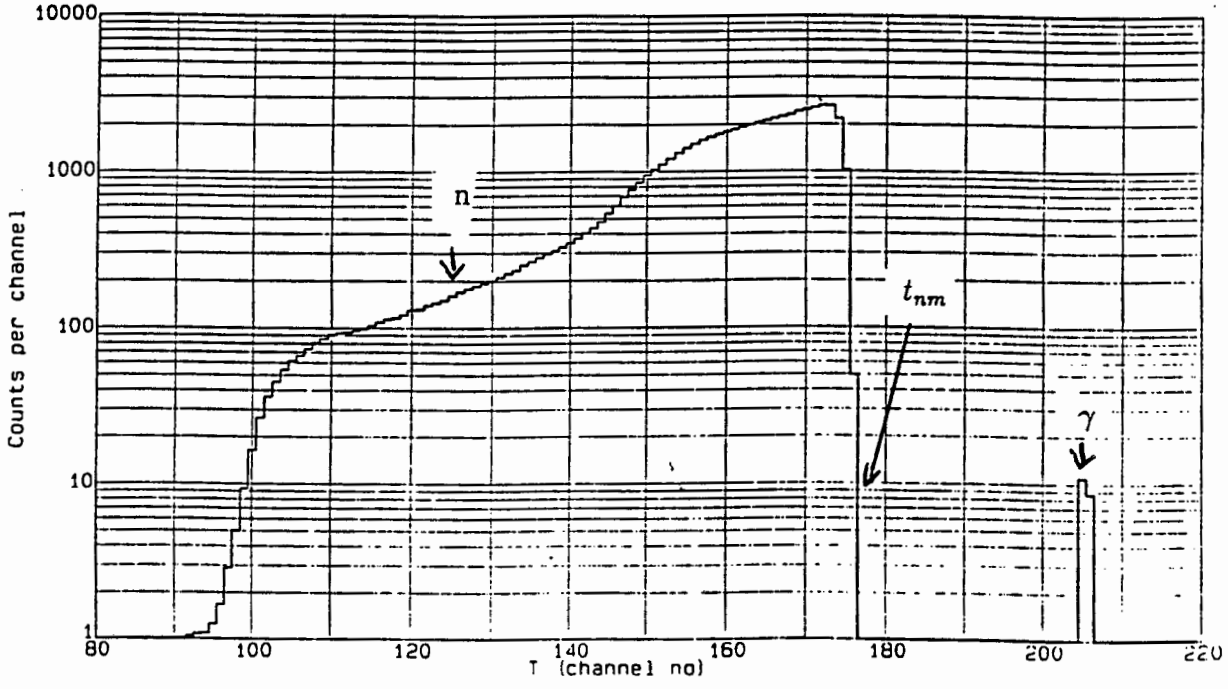

Figure 3.4: *The time-of-flight spectrum measured by an NE230 scintillator at a distance of 5.77 m from the* ^{9}Be *target. See text for details.*

highest energy neutrons which are released from the ground state transition of the ^{9}Be(p,n)^{9}B reaction. Some protons lose energy due to scattering in the target. This energy loss ranges from zero to a maximum value, which depends on the energy of the incident protons and the target thickness. The maximum energy loss for 66 MeV protons in the 19.6 mm beryllium target was calculated to be 38.15 MeV. Using the Q-value of the ^{9}Be(p,n)^{9}B reaction of -1.85 MeV, the maximum energy of the neutrons emerging from the reaction ^{9}Be(p,n)^{9}B$_{gs}$ was calculated using the standard reaction kinematic equations (Appendix B) to be 63 MeV.

There is also a gamma peak to the right of the neutrons at channel number 2060 in figure 3.4. This peak arises from the low energy gamma rays emitted in the proton induced reactions in the beryllium target. These gamma rays reach the detector at a fixed time, t_{γ}, defined by the speed of light, c, and the flight path, d. The full width at half maximum (FWHM) of the gamma peak (0.68 ns) provides a measure of the intrinsic timing resolution of the system.

The absence of counts in the time-of-flight spectrum between the gamma peak (γ) and the neutron distribution (n) indicates that the background is negligible. The sharp decrease in the count rate below ADC channel number 1000 in the time-of-flight spectrum is caused by the electronic threshold on the pulse height parameter (L_A). This is the threshold for the acceptance of events from recoil deuterons resulting from n-d elastic scattering in the scintillator.

3.3.2 Scattered Neutron Time of Flight Spectrum

Figure 3.5 shows the scattered neutron time-of-flight spectrum measured in this work. This spectrum, like the incident neutron time-of-flight spectrum, has a broad neutron energy distribution (n) and sharp gamma peak (γ). The gamma peak is produced by gamma rays released from the decay of the excited states of the NE230 scintillator constituents. The gamma peak is dominated by the decays of the 2^{+} state at 4.44 MeV and the 1^{+} states at 12.7 MeV and 15.1 MeV of ^{12}C in the NE230 scintillator. The 2^{+} state can only decay by gamma ray emission since this state is below the threshold energy for decay by alpha emission.

The neutrons (n) in figure 3.5, are neutrons which have been scattered out of the NE230 scintillator. These are the neutrons from (i) n-d scattering, (ii) n-p scattering from the small hydrogen content in the scintillator (see table 2.1), (iii) inelastically scattered neutrons from the ^{12}C(n,n')3α reaction and (iv) neutrons from deuteron breakup in the NE230 scintillator.

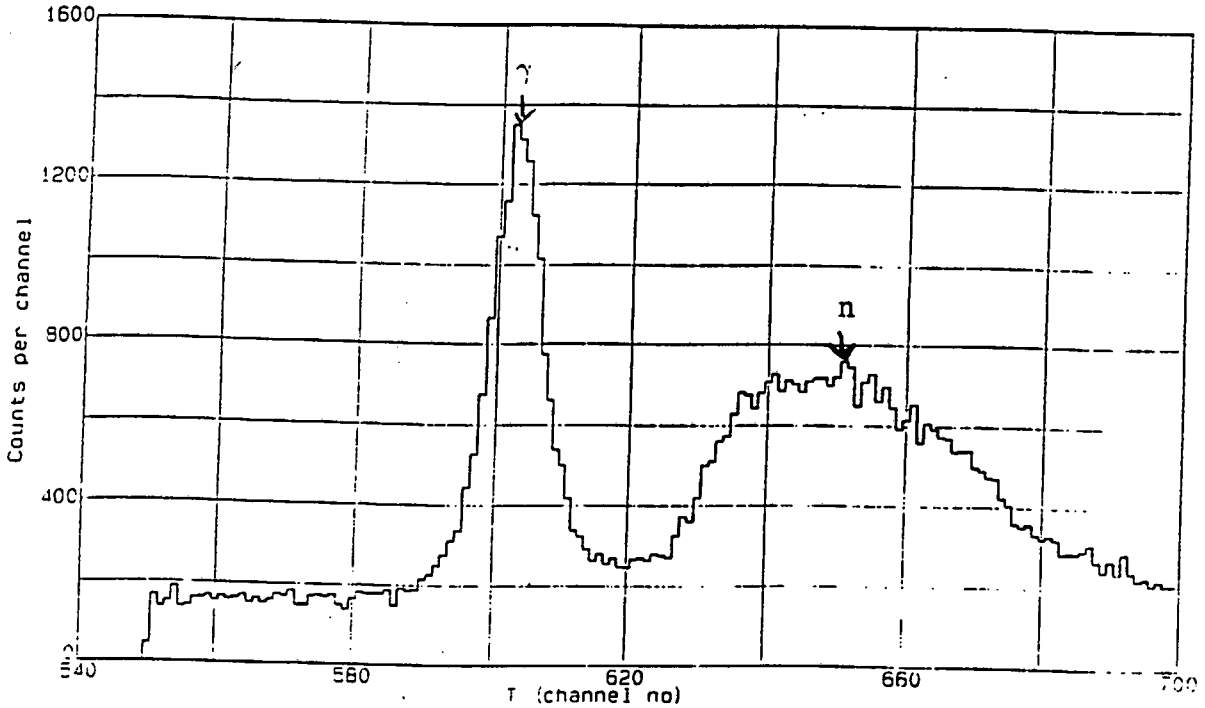

Figure 3.5: *The time-of-flight spectrum measured by an NE213 liquid scintillator at a centre to centre distance of 0.474 m from the NE230 scintillator.*

3.4 The L-T_n Spectra

Figures 3.6 and 3.7 show the L versus T_n plots for singles events in the NE230 scintillator, identified as deuterons and alphas respectively by PSD. The ridge (D_f) in figure 3.6 corresponds to the forward recoiling deuterons from the n-d elastic scattering, and the second ridge which starts at higher T_n (D_1 in figure 3.6) corresponds to the deuterons from the ground state transition of the $^{12}C(n,d)^{11}B$ reaction. In figure 3.7 (for alphas) two distinct components from the interaction of the neutron with carbon can be identified. These are the alphas from the two reactions: (i) $^{12}C(n,\alpha)^9Be_{gs}$ and (ii) $^{12}C(n,n')3\alpha$. The alphas from the ground state transition of the $^{12}C(n,\alpha)^9Be$ reaction have higher energies and larger pulse heights and thus form a ridge at the high pulse height region of the L-T_n plot. The alphas from the $^{12}C(n,n')3\alpha$ reaction on the other hand have lower energies and therefore lower pulse heights (since the energy released from the reaction is shared by the three alpha particles, whereas in the first reaction all the energy is taken by the single alpha and only a little bit by the heavier recoiling ^9Be nucleus). These alpha particles form two ridges at lower pulse heights, one broad ridge is formed at lower L and higher T_n values, and the second smaller ridge is

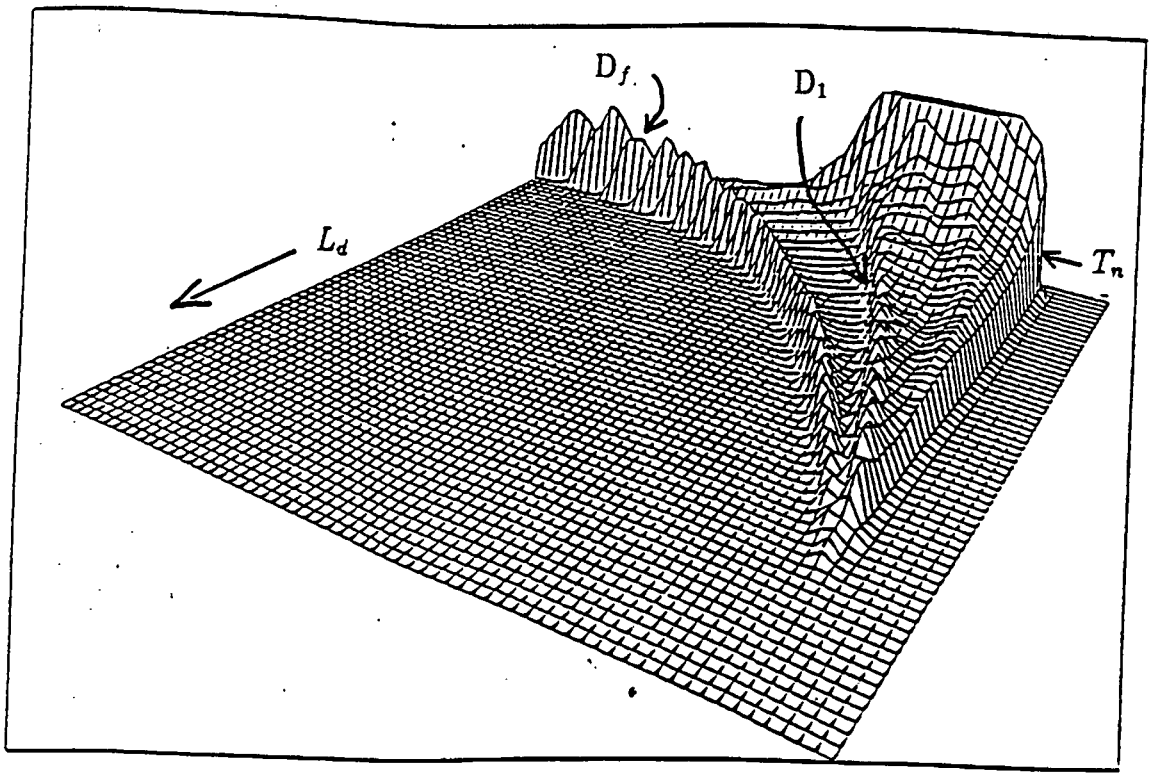

Figure 3.6: *Perspective view of counts (vertical) versus pulse height (L) and time-of-flight, T_n, measured by the NE230 scintillator for events identified as deuterons by PSD.*

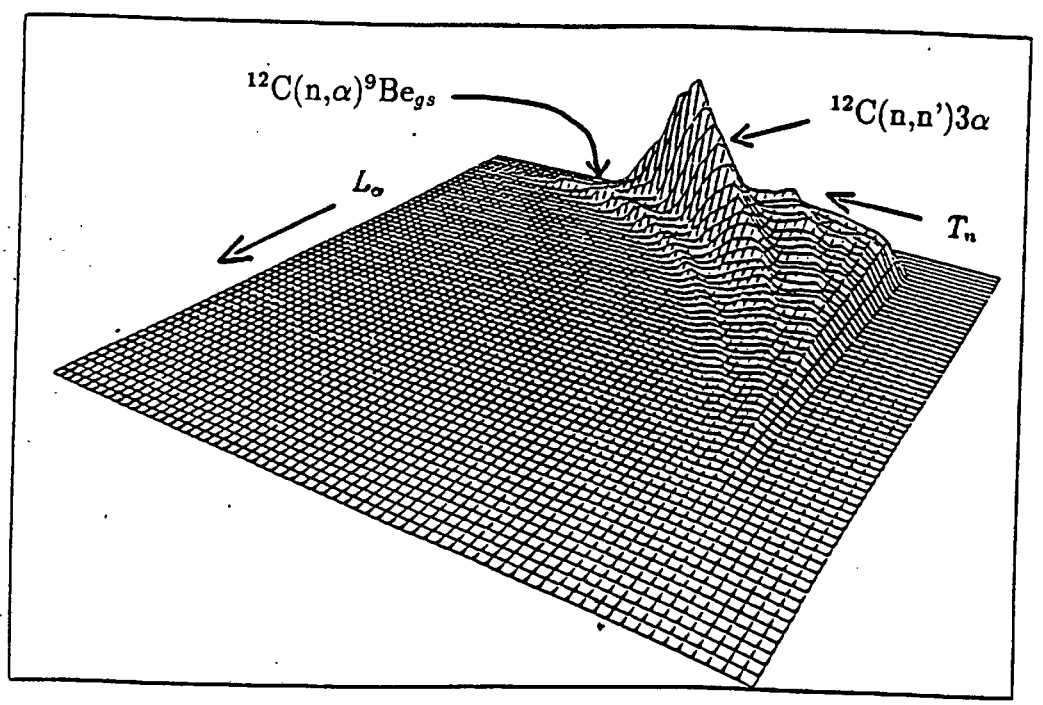

Figure 3.7: *Perspective view of counts (vertical), pulse height (L) and time-of-flight, T_n, measured by the NE230 scintillator for events identified as alphas by PSD. There is a clear distinction of the events corresponding to the two alpha producing reactions.*

formed at the lower T_n values (see figure 3.7). This could be interpreted to mean that there is difference in the energy distribution of the alpha particles released from the $^{12}C(n,n')3\alpha$ reaction (see sections 4.1.1 and 5.1.1).

Figures 3.8a and 3.8b show scatter plots of L-T_n for the events identified as alphas measured by the NE230 scintillator for singles and coincidence events respectively. As expected the edge corresponding to the alpha particles from the $^{12}C(n,\alpha)^9Be_{gs}$ reaction is absent in the coincidence scatter plot (figure 3.8b).

After setting appropriate T_n to select discrete (quasi-monoenergetic) neutron energies, the events in each window were projected onto the L-axis. Figures 3.9 and 3.10 are the projected spectra for the events identified as deuterons and alphas respectively, at different incident neutron energies for singles events measured by the NE230 scintillator. The peaks in the alpha pulse height spectrum are attributed to alpha particles from the $^{12}C(n,\alpha)^9Be_{gs}$ reaction (A_o in figure 3.10), and alpha particles from the $^{12}C(n,n')3\alpha$ reaction (A_1) reaction (see section 5.1.1). At the incident neutron energy of 15 MeV only the tail end of the peak corresponding to the $^{12}C(n,\alpha)^9Be_{gs}$ reaction is seen on the spectrum, the other part is below the detector and electronic threshold. The counts scale in figure 3.10 was multiplied by the factors shown in the figure for clarity. The peaks in the deuteron spectrum in the deuteron pulse height spectrum are attributed to deuterons from the $^{12}C(n,d)^{11}B_{gs}$ reaction (D_1 in figure 3.9) and the forward recoil deuterons from n-d elastic scattering (D_f) (see section 5.1.2). The continua (D_c) is formed by the deuterons from the $^{12}C(n,nd)^{10}B$ reaction and recoil deuterons from n-d elastic scattering. The width of the T_n window was limited to 0.68 ns to match the timing resolution of the incident neutron time-of-flight measurements (see figure 3.11).

3.5 Detector Calibrations

The details of the methods used for the calibration of the two detectors are in appendix C, this section gives a summary of the calibrations.

3.5.1 Energy Calibration for the NE230 Detector

The time of flight channel scale was calibrated in nanoseconds by using the differences in the positions of the gamma peak and the most energetic neutrons, and the differences in their flight times. The neutron time of flight T_n was calculated using:

$$T_n = k\,(T_e - n) + 52.6\ ns \tag{3.2}$$

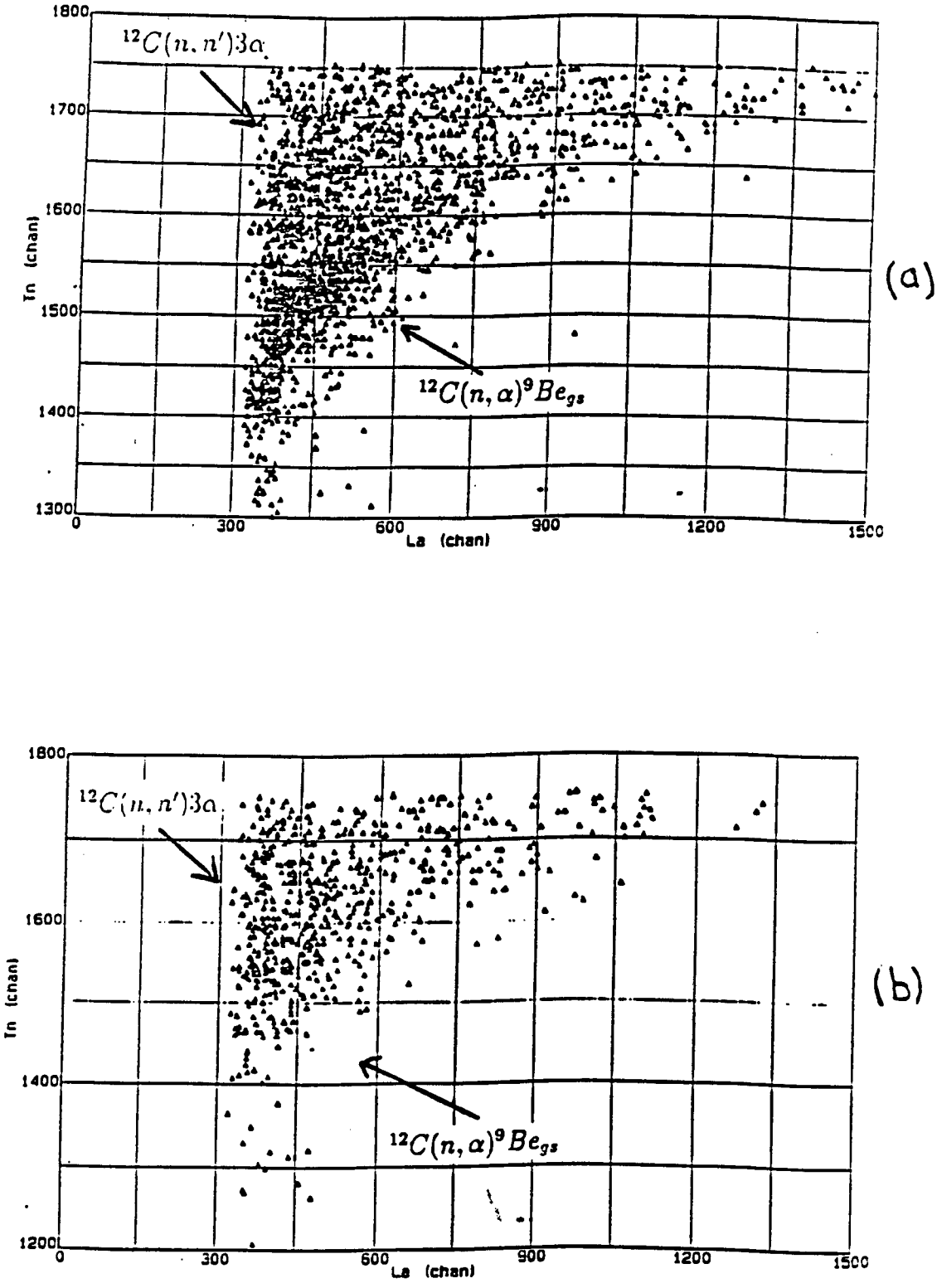

Figure 3.8: *(a) Density plot for the singles events identified as alpha particles by PSD, measured by the NE230 scintillator. (b) Density plot for the coincidence events identified as alpha particles by PSD, measured by the NE230 scintillator. There is an absence of events corresponding to alphas from the* $^{12}C(n,\alpha)^9Be_{gs}$ *reaction in (b). The few events which are observed in this region are caused by the accidental coincidences.*

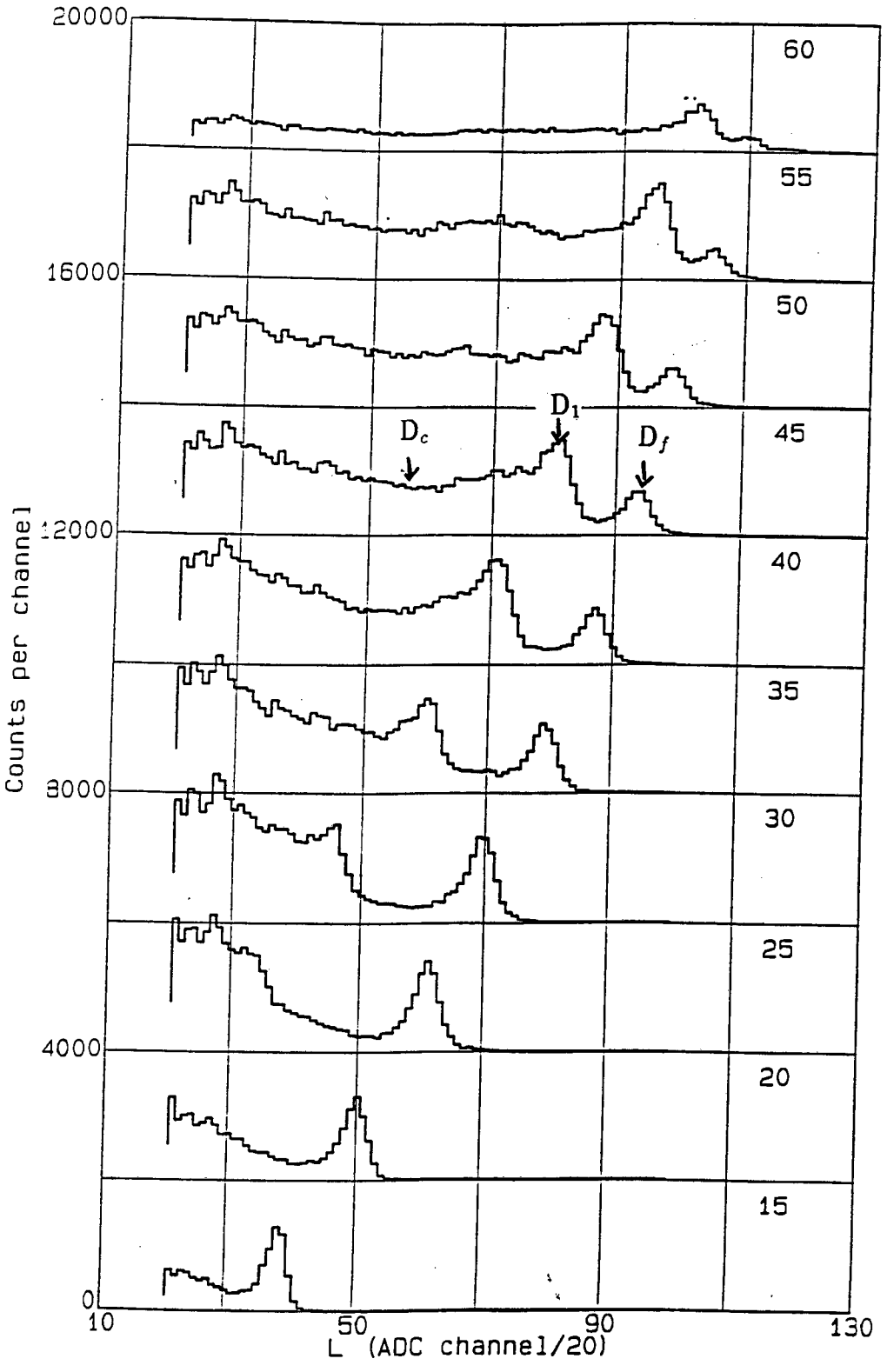

Figure 3.9: *Counts versus pulse height for the singles events identified as deuterons by PSD at different incident neutron energies (all energies are in units of MeV). The peaks in the spectrum correspond to deuterons released from the interaction of neutrons with the nuclei in the scintillator. See text for details. No zero correction has been applied, true zero lies at ADC channel number 200.*

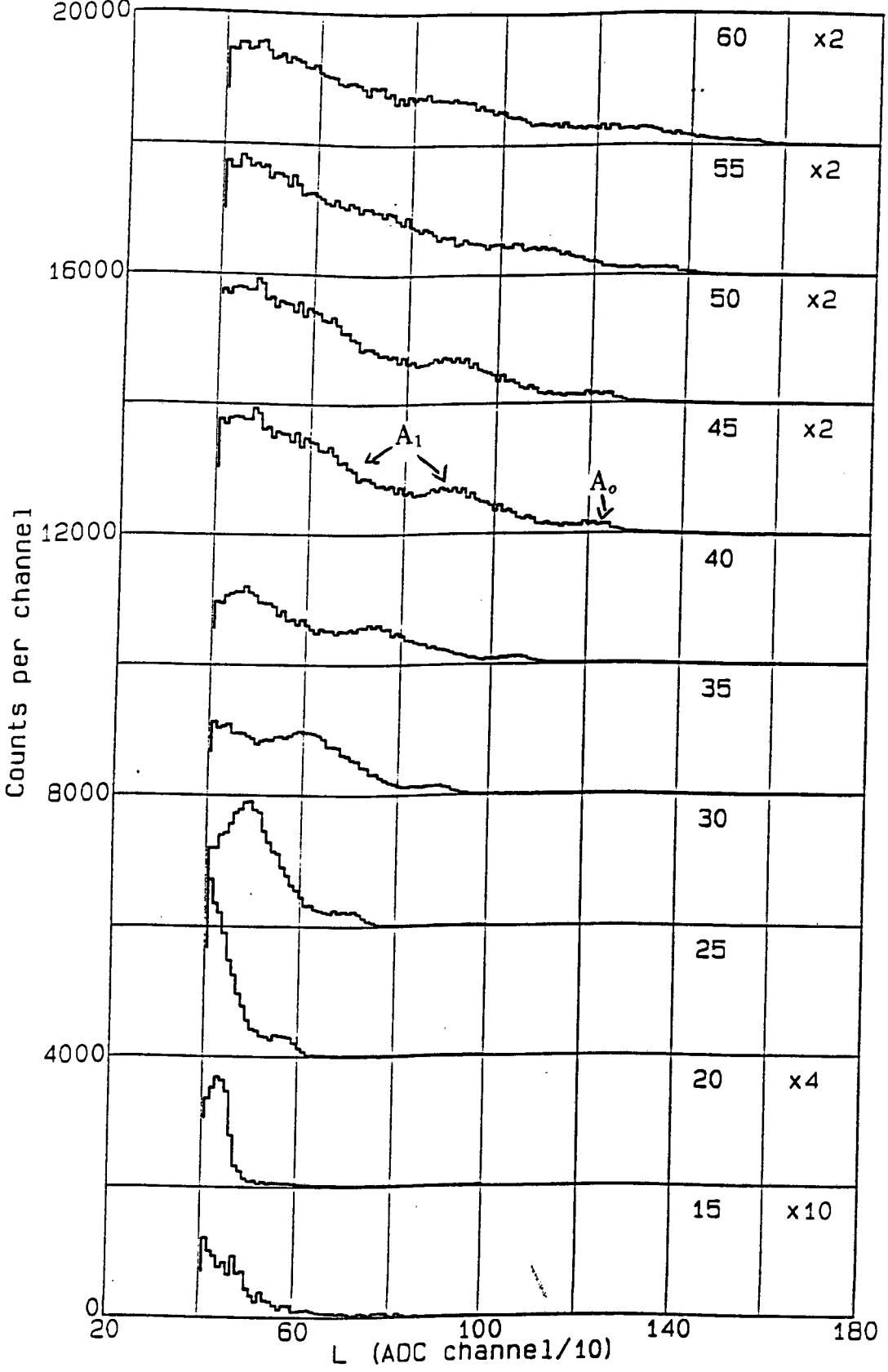

Figure 3.10: *Counts versus pulse height for the singles events identified as alpha particles by PSD, at different incident neutron energies (all energies are in units of MeV). The peaks in the spectrum correspond to alphas from the different alpha producing reactions. See text for details. No zero correction has been applied, true zero lies at ADC channel number 200. Some count scales are multiplied by the factors shown for clarity.*

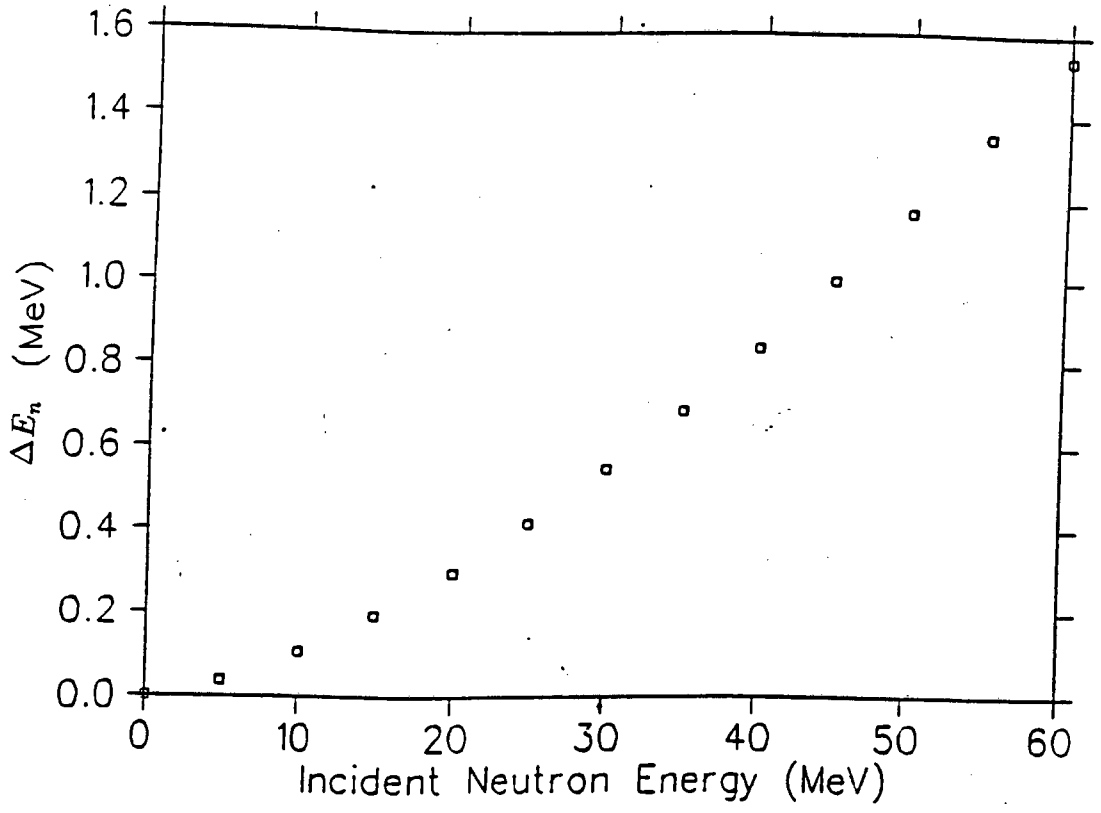

Figure 3.11: *The FWHM energy resolution, ΔE_n, as a function of E_n for the incident neutron energies considered in this work.*

where: n : ADC channel number
T_e : position of the most energetic neutrons (ADC channel number)
k : 0.111 nanosecond/channel (time calibration)
52.6 ns : flight-time of the most energetic neutrons

The neutron energy E_n (in MeV) corresponding to the time of flight T_n (in ns), was calculated by using the non-relativistic time-of-flight equation:

$$E_n = \left\{ \frac{72.3\ d}{T_n} \right\}^2 \tag{3.3}$$

where: T_n : as in equation 3.2 above
d : flight path of the neutrons (in metres)

The uncertainty in the neutron energy measurement, ΔE_n was determined by using the timing resolution, ΔT_γ (FWHM of the gamma peak), of the system. Figure 3.11 shows FWHM energy resolution, ΔE_n, as a function of E_n for the incident neutron energies considered in this work.

3.5.2 Calibration for the NE213 Detector

The time of flight channel scale was calibrated to a nanosecond scale by changing the time delay of the stop signal going into the the TAC by a known amount, and observing the change in the position of the neutron edge in the time of flight spectrum. The neutron time-of-flight T_c was given by the relationship:

$$T_c = k\,(n - T_\gamma) + \frac{d}{c} \qquad (3.4)$$

where:
- n : ADC channel number
- d : detector centre to centre distance (0.474 m)
- c : speed of light
- k : 0.11 nanosecond/channel (time calibration)

The neutron energy E_c corresponding to the time of flight T_c, was calculated by using the non-relativistic time-of-flight equation (equation 3.3).

3.5.3 Pulse Height Calibrations

The pulse heights from the two LINK modules were corrected for true zero by using the preamplifier connected to the LINK input to generate a dynode signal, D, (see appendix C for details). The scintillators were calibrated in terms of equivalent electron energy by using gamma ray sources. The scintillators were calibrated by recording the pulse height for the 4.44 MeV γ-rays from an AmBe source and the 2.75 MeV γ-rays from ^{24}Na. Figure 3.12a shows the pulse height spectra for gamma rays from the AmBe source and ^{24}Na recorded by the NE230 scintillator. The features in the spectra are (i) the 3.42 MeV double escape peak (De),(ii) the 2.75 MeV compton edge ($C_{2.75}$) from the gamma rays from ^{24}Na and (iii) the 4.2 MeV compton edge ($C_{4.2}$) corresponding to the 4.44 MeV γ-rays from the AmBe source. For the NE213 scintillator we can only identify the compton edge associated with the 4.44 MeV γ-rays of the AmBe, which is sufficient for our purpose (figure 3.12). The three measurements of the two Compton edges and the double escape peak in the NE230 scintillator are plotted in figure 3.13. A fit on the data indicate that there is a linear relation between the scintillation light output and the electron energy.

The pulse height for the different charged particles can also be calibrated as a function of the energy (in units of MeV) deposited by the these particles. The pulse height spectra for deuterons have two peaks which have been identified as (i) deuterons from the forward recoil n-d elastic scattering and (ii) deuterons

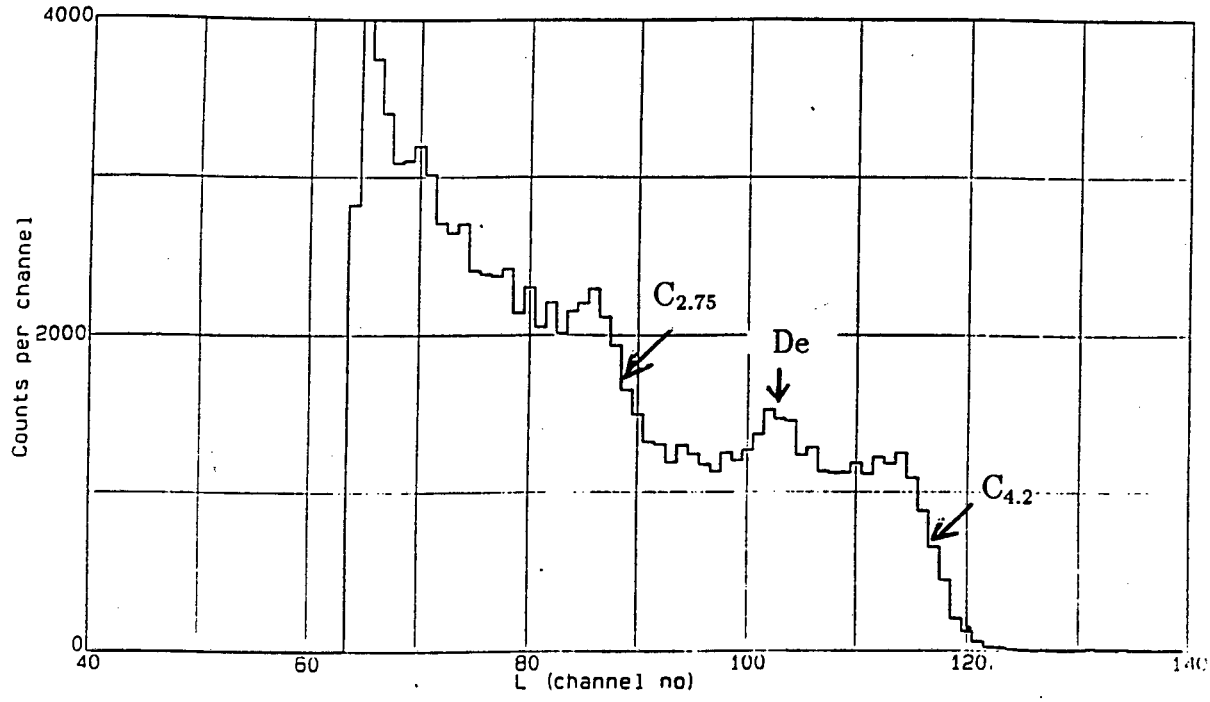

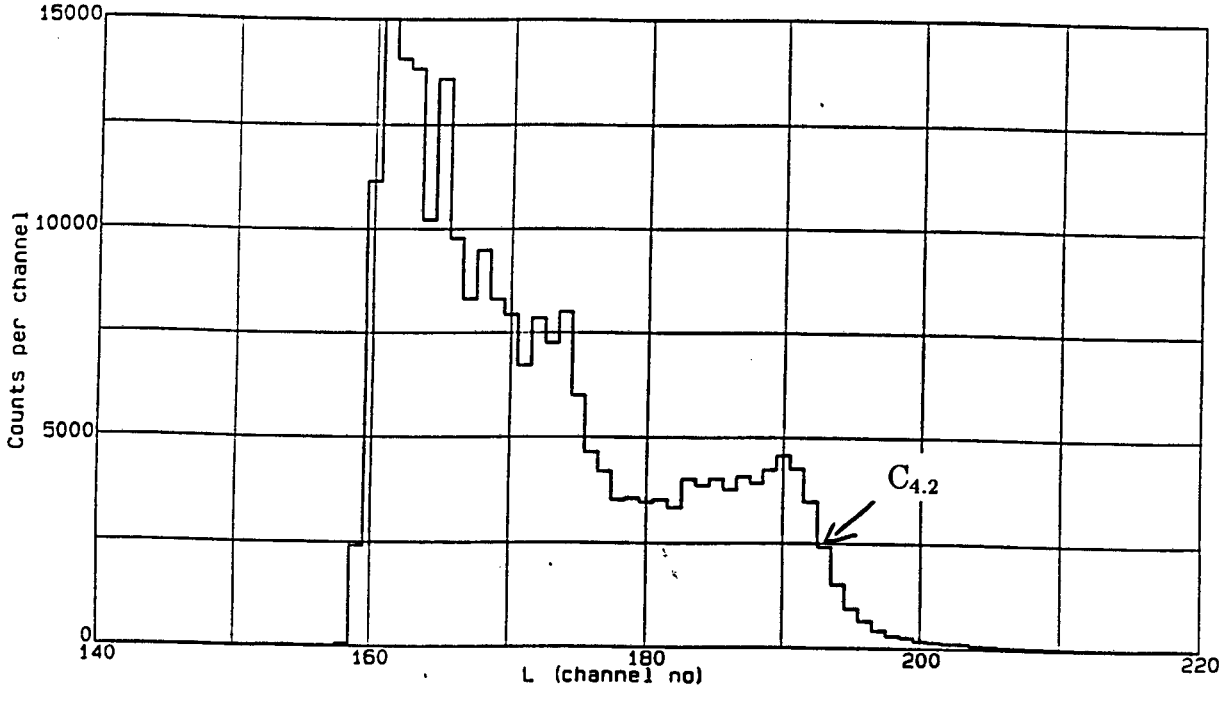

Figure 3.12: *(a) Pulse height spectrum recorded with the NE230 scintillator for the gamma rays from the AmBe source and* ^{24}Na. *(b) Pulse height spectrum recorded with the NE213 scintillator for the gamma rays from the AmBe source.*

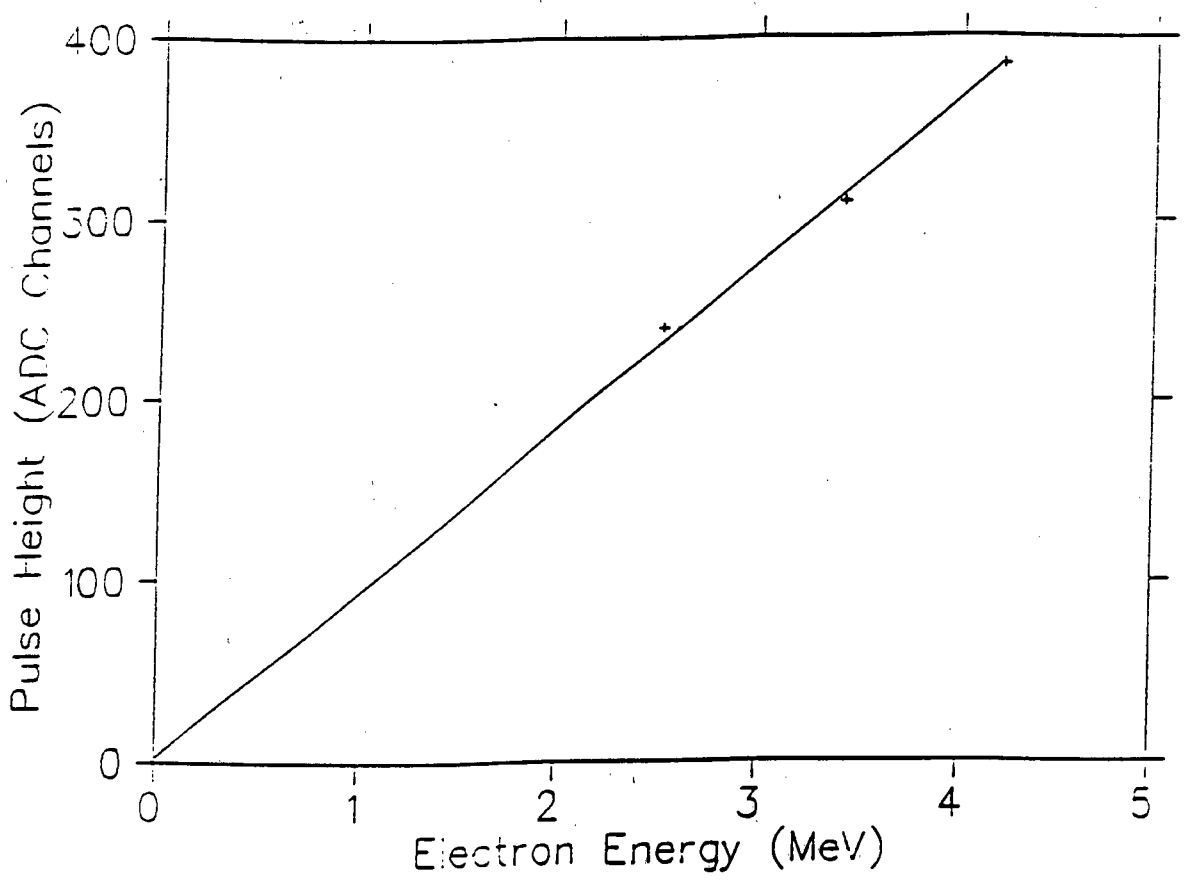

Figure 3.13: *Calibration of pulse height channel to electron energy for the NE230 scintillator.*

from the $^{12}C(n,d)^{11}B$ ground state transition (figure 3.9). The energy of these deuterons was calculated using the kinematics of the scattering and the non-relativistic kinematic equation (appendix B) respectively. Figure 3.14 shows the pulse height (in units of MeVee) as a function of the deuteron energy (in units of MeV) for all the deuteron events detected in the NE230 scintillator. The deuteron and alpha particles response data deviate from the expected linear dependence [Br79] at higher pulse heights. This effect is caused by space charge saturation in the photomultiplier.

The alpha particle pulse height spectrum (figure 3.10) has a peak at the higher pulse height region which was identified as the ground state transition of the reaction $^{12}C(n,\alpha)^{9}Be$. The outgoing alpha particle energy for the alphas produced in this reaction was calculated as a function of incident neutron energy using the kinematic equations. The pulse height (in units of MeVee) as a function of alpha energy for the alphas detected in the NE230 scintillator is also shown in figure 3.14.

In summary the experiment was conducted using the NE230 and NE213 organic scintillators to record the singles and coincidence events simultaneously. The time

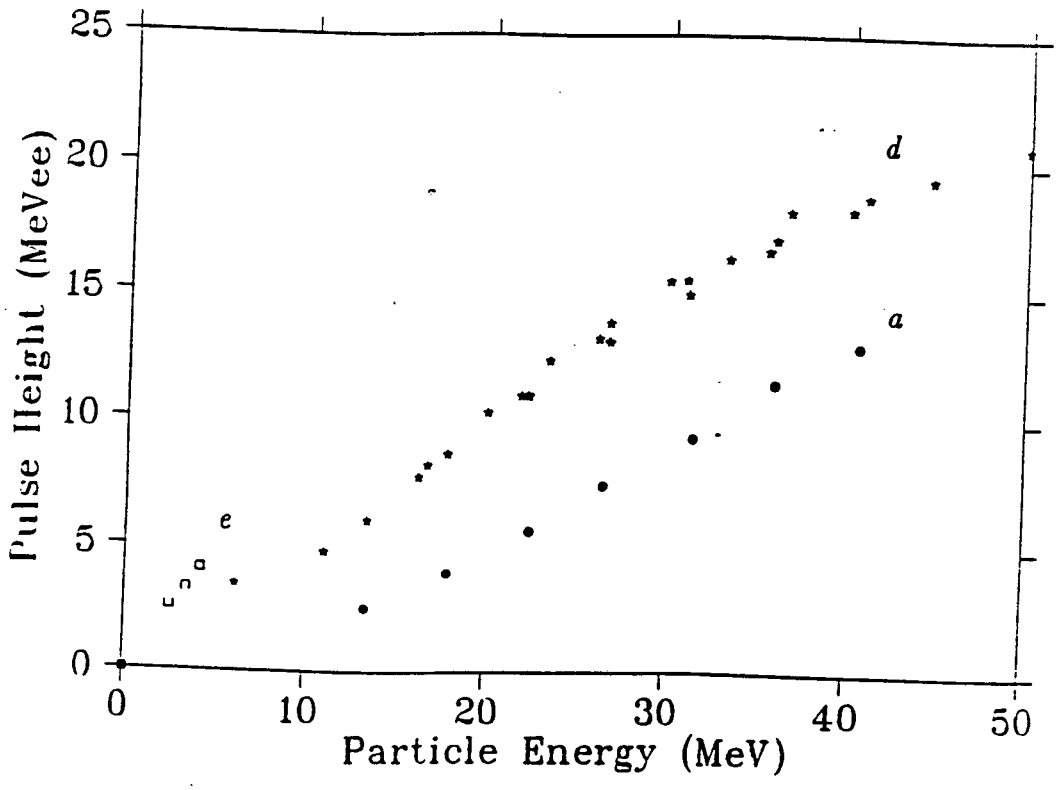

Figure 3.14: *Measurements of the response (pulse height) of the NE230 detector as a function of charged particle energy for the electrons (e), deuterons (d) and alphas(a).*

of flight method was used to determine the energy of the incident and scattered neutrons. Pulse shape discrimination was used to identify and to separate the different charged particles and the reaction products. Software cuts were applied on the time of flight parameter in the L-T_n plots and the events on these windows were projected onto the L-axis to provide the pulse height spectrum for the alpha particles and deuterons as a function of neutron energy.

The next chapter deals with pulse shape discrimination at different neutron energies to analyse the structure in the loci in the PSD plots.

Chapter 4

Pulse Shape Discrimination at Different Neutron Energies

In chapter 3, the use of pulse shape discrimination to identify and separate different charged particles and reaction products was described. Figure 4.1 is a perspective plot of counts as a function of pulse height and pulse shape for neutrons of energy 63 MeV incident on the NE213 liquid scintillator. As explained in Chapter 3 and Appendix B, each ionizing particle detected has particular L and S values, which when plotted on a plane, form unique loci which depend on the type and energy of the particles. The event signals corresponding to different charged particles detected are seen to lie on well-defined ridges which are resolved on this L-S plane. These ridges correspond to alpha-particles, *a*, deuterons, *d*, and protons, *p*. The alpha locus in the LS spectrum of figure 4.1 has structure which may be attributed to the different reaction pathways in the decay of the carbon-12 nucleus. The feasibilty of distinguishing the two alpha producing reactions, viz $^{12}C(n,\alpha)^{9}Be$ and $^{12}C(n,n')3\alpha$ was investigated using the pulse shape dicrimination technique.

The LS spectrum was analysed at neutron energies ranging from 10 to 200 MeV to investigate the changes in the spectrum as the incident neutron energy changes. This was done by analysing the LS spectrum using the events scatter plots for the singles and the coincidence conditions and comparing the spectra. One set of measurements was made using the NAC radiotherapy facility providing a neutron beam of energy ranging from 10 to 66 MeV. A NE230 deuterated liquid scintillator was a carbon target for these measurements. The other measurement was made with the neutron beam with a time-of-flight window set to select neutrons with an energy of 195 MeV using an NE213 liquid scintillator. This neutron beam is produced from the $^{7}Li(p,n)^{7}Be$ reaction with a pulsed proton beam of energy E_p = 197 MeV from the separated-sector cyclotron at the NAC.

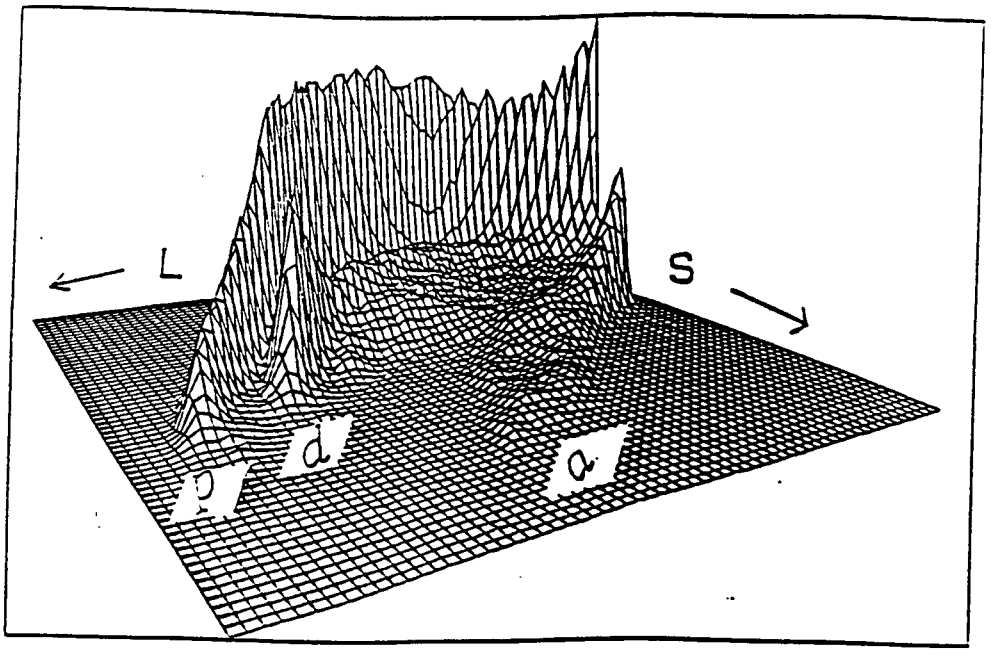

Figure 4.1: *Perspective view of counts (vertical) as a function of pulse height, L, and pulse shape parameter, S, for the singles events measured by an NE213 scintillator when exposed to quasi-monoenergetic neutrons of energy E_n = 63 MeV. The ridges correspond to protons, p, deuterons, d, and alphas, a.*

4.1 The Singles Spectra at Low Incident Neutron Energies

The analyses in this section are for neutron energies in the range 10 to 66 MeV. Figure 4.2 is a perspective plot of counts as a function of pulse height and pulse shape for the singles events measured by the NE230 scintillator, for an incident neutron energy of 40 MeV. The ridges correspond to protons, *p*, escaping protons, *e*, deuterons, *d*, and alphas, *a*. The ridges are clearly distinguished at higher values of L, however with decreasing pulse height, this separation diminishes. The structure in the alpha locus of figure 4.1 is clearer than in figure 4.2 due to the difference in dispersion of the plots and the superior pulse shape discrimination properties of the NE213 scintillator compared to the NE230 scintillator.

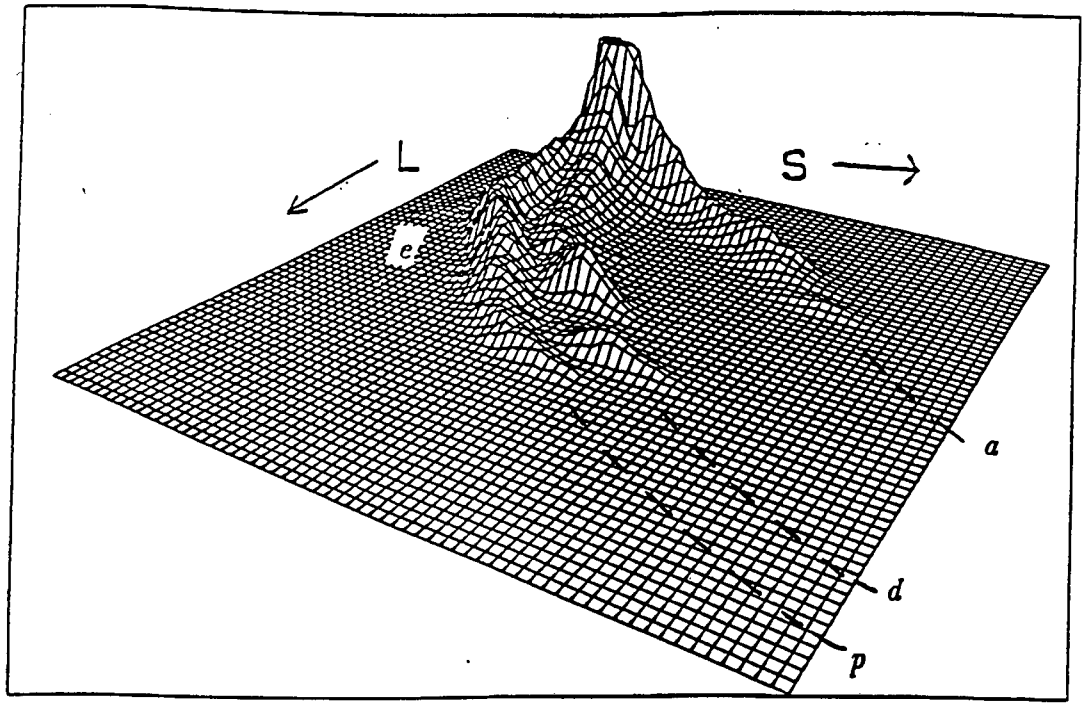

Figure 4.2: *Perspective view of counts (vertical) as a function of pulse height, L, and pulse shape parameter, S, for the singles events measured by an NE230 scintillator when exposed to neutrons of energy E_n = 40 MeV. The ridges in the spectrum correspond to alpha-particles, a, deuterons, d, protons, p, and escaping protons, e.*

4.1.1 The Alpha Locus

The alpha locus (*a* in figure 4.2) is made up mainly of alpha particles from the ^{12}C(n,α)^{9}Be and ^{12}C(n,n')3α reactions. The events at the high L region of the locus are attributed to the ground state transition of the ^{12}C(n,α)^{9}Be reaction. Each scintillation pulse processed by the NE230 detection system is the sum of the scintillations produced by all the outgoing charged particles emitted in that scintillator for the event. If the alpha particle from the ^{12}C(n,α)^{9}Be$_{gs}$ has an enegry 3E, then each alpha particle from the ^{12}C(n,n')3α will have an energy E. It is expected that the scintillator light output for an alpha of energy 3E (released in an ^{12}C(n,α)^{9}Be$_{gs}$ event) will be greater than that for three alphas released from a ^{12}C(n,n')3α interaction. This is in accordance with the Birks' formula [Bi59] for the scintilating light output of organic scintilators:

$$\frac{dL}{dx} = \frac{S\frac{dE}{dx}}{1 + kB\frac{dE}{dx}} \tag{4.1}$$

where S is the scintillation efficiency and kB is a parameter that is adjusted to fit experimental data for a specific scintillator. The alpha particles from the ^{12}C(n,n')3α will thus lie in the low pulse height region.

The light output of alpha particles from the two alpha producing reactions have different pulse shape parameters, S. This is caused by the difference in the contributions to the light output from the two reactions. In the $^{12}C(n,\alpha)^{9}Be_{gs}$ reaction the alpha particle is the major contributor to the light output "seen" by the photomultiplier tube and the heavily ionizing ^{9}Be contributes a negligible amount to the light output for the event. As dicussed in chapter 1, the sequential decay involving n + α + $^{8}Be_{gs}$ (or $^{8}Be_{2.9}$) system appears to be the dominant reaction mechanism for the decay of ^{12}C into three alpha particles [An83]. The decay paths which go via this system are the $^{12}C(n,\alpha)^{9}Be^{*}(n',^{8}Be^{*}(2\alpha))$ and $^{12}C(n,n')^{12}C^{*}(\alpha,^{8}Be^{*}(2\alpha))$ decay paths. In these decay paths one alpha particle is released first followed by the release of the other two alpha particles. The first alpha particle is released with the large proportion of the available energy, while the rest of the energy will be shared by the other two alpha particles. The two lower energy alpha particles contribute a large proportion of the slow component to the light output of the event. The excitation of states in the molecules of the scintillator depends on the rate of energy loss, dE/dx, of the ionising particle. Particles with a large rate of energy loss, dE/dx, have a larger slow component. The alpha particles from the $^{12}C(n,n')3\alpha$ reaction have a higher average dE/dx than alpha particles from the $^{12}C(n,\alpha)^{9}Be$ reaction. The alpha particles from the $^{12}C(n,n')3\alpha$ reaction are expected to have a larger pulse shape parameter, S, than the alpha particle from the $^{12}C(n,\alpha)^{9}Be_{gs}$ reaction, producing a partial separation in the alpha locus in the LS spectrum. The alpha particles from the $^{12}C(n,n')3\alpha$ reaction lie on the higher S region of the alpha locus and the alpha particles from the $^{12}C(n,\alpha)^{9}Be_{gs}$ reaction lie on the lower S region of the alpha locus. This separation in the alpha locus can be seen in the figure 4.1.

Figures 4.3 and 4.4 show event scatter plots of LS spectra for the singles events measured by the NE230 scintillator at 10 different incident neutron energies in the range 15 to 60 MeV. The ridges in the figure correspond to the protons, *p*, deuterons, *d*, alphas, *a*, and escaping protons, *e*. Events in the escaping protons locus, *e*, correspond to protons which do not stop in the scintillator. At incident neutron energies less than 15 MeV no distinct alpha locus is visible. At energies 15 to 25 MeV a distinct alpha locus appears but a clear distinction between the two alpha producing reactions is not possible. At neutron energies above 25 MeV, the peak corresponding to the $^{12}C(n,\alpha)^{9}Be_{gs}$ reaction can be distinguished at the tip of the alpha locus. As the incident neutron energy increases the valley between the peak due to the alpha particles from the $^{12}C(n,\alpha)^{9}Be_{gs}$ reaction and the events from the other alpha particles diminishes. This can be interpreted to mean that as the incident neutron energy increases the peak corresponding to alpha particle in the $^{12}C(n,n')3\alpha$ emerges and shifts in pulse height towards the high pulse height peak until it overlaps with it at incident neutron energies above 50 MeV. This may be caused by the possible changes in the distribution

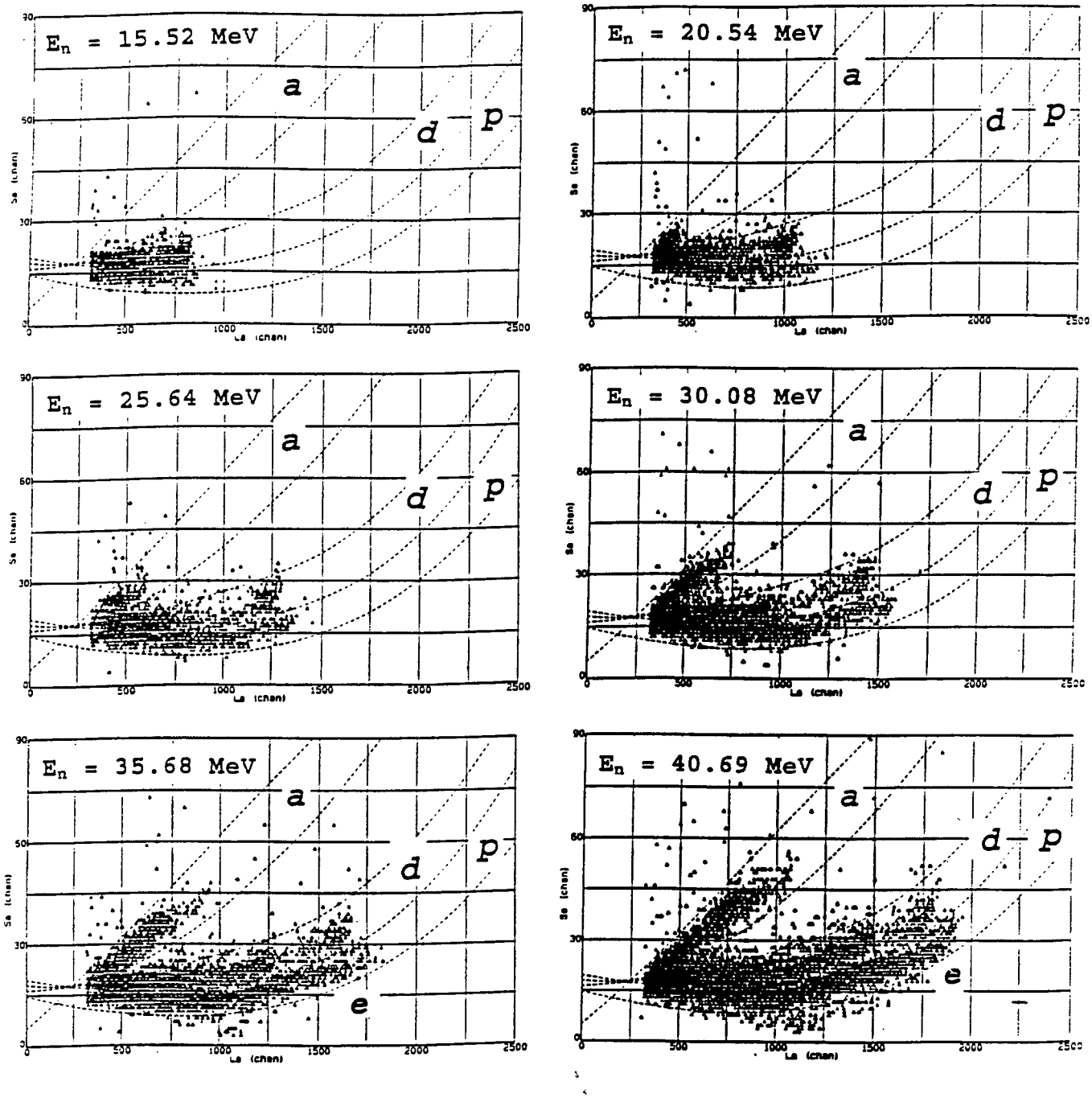

Figure 4.3: *Scatter plots of "singles" events detected by the NE230 scintillator as a function of pulse height , L, and pulse shape, S, at different incident neutron energies. The ridges correspond to the alphas, a, deutrons, d, protons, p, and escaping protons, e. No zero correction have been applied. True zero is located at* $L_\alpha = 200$ *channels.*

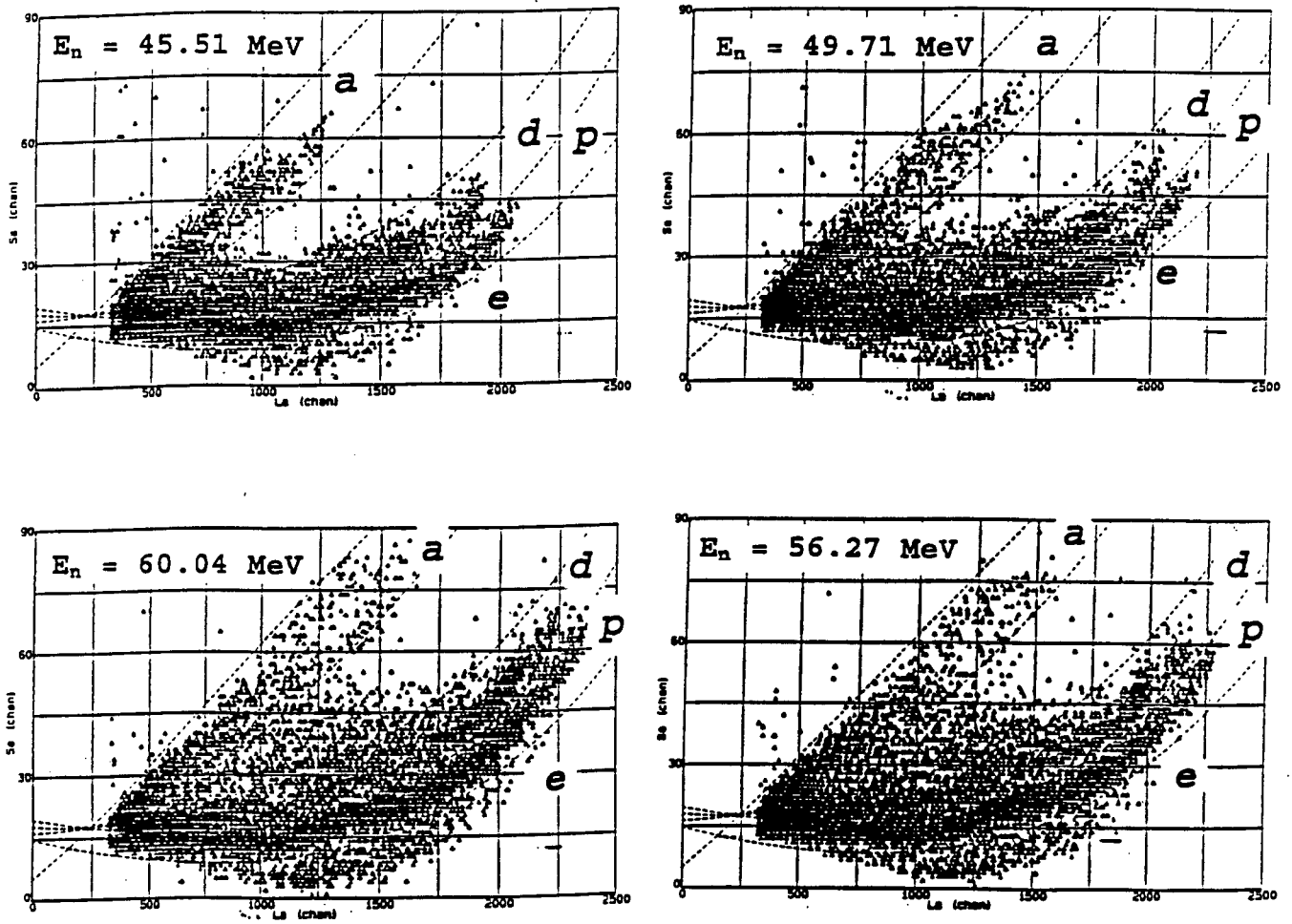

Figure 4.4: *Same as in figure 4.3 for higher incident neutron energies.*

of the available energy between the alpha particles produced in the ^{12}C(n,n')3α reaction in favour of the first alpha particle released i.e as the incident neutron energy increases the first alpha particle is released with an increasingly larger fraction of energy relative to the other two alpha particles. This suggests that at high incident neutron energy ($E_n > 50\ MeV$) the first alpha particle is released with almost all the available energy; the remaining energy is just enough for the breakup of the ^{8}Be nucleus into the other two alpha particles. Thus at high E_n the first alpha particle released from the ^{12}C(n,n')3α reaction will have approximately the same energy and thus same pulse height as the alpha particle from the ^{12}C(n,α)^{9}Be$_{gs}$ reaction. In some cases, however, the energy available for the breakup of the ^{8}Be is high enough for the released alpha particles to have a significant scintillation pulse. Since the scintillation pulse processed by the detection system is the sum of the scintillation produced by all the outgoing charged particles in the event, the total scintillation for some alpha particles released from the ^{12}C(n,n')3α reaction will have a higher pulse shape parameter. A full Monte Carlo simulation of the breakup mechanism and the resulting energy deposition is needed to confirm this hypothesis.

4.1.2 The Deuteron Locus

The deuteron locus (*d* in figure 4.2)) is due to recoil deuterons from n-d elastic scattering and the deuterons released from n-^{12}C interactions. The deuterons from n-^{12}C interactions are released mainly through the ^{12}C(n,d)^{11}B and ^{12}C(n,nd)^{10}B reactions. The deuteron locus has a peak at the higher pulse height region which is attributed to the n-d backward elastic scattering. From figure 4.5, which shows the differential n-d elastic scattering cross-section, it can be seen that the n-d elastic cross-section is peaked in the forward and backward directions. The forward recoil deuterons have higher energies compared with the other deuterons from n-d elastic scattering, and therefore have a higher pulse height. The other peak in the deuteron locus corresponds to the deuterons from the ^{12}C(n,d)^{11}B$_{gs}$ reaction. Deuterons from the ^{12}C(n,nd)^{10}B reaction form a continuum which stretches down to the low pulse height region. Deuterons from n-d elastic scattering also contribute to this continuum.

In figures 4.3 and 4.4, it can be seen that as the incident neutron energy increases the peak corresponding to the deuterons from the ^{12}C(n,d)^{11}B reaction shifts in pulse height towards the peak associated with the forward elastically scattered deuterons until they overlap at high neutron energies. This is a kinematic effect caused by the relatively larger increase in the energy of the outgoing deuterons from the ^{12}C(n,d)^{11}B$_{gs}$ reaction with increasing incident neutron energy com-

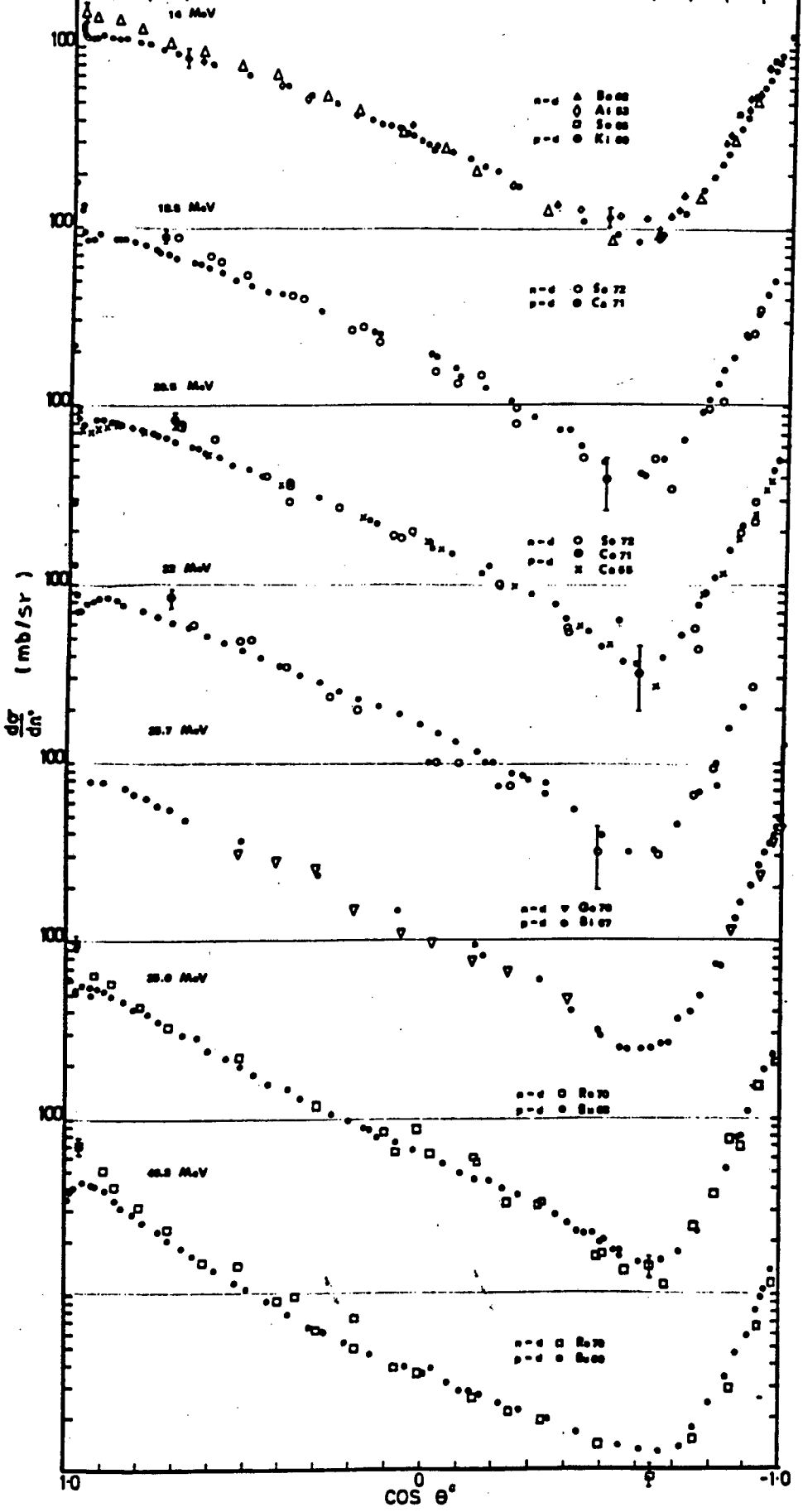

Figure 4.5: *Differential cross-section data for* n-d elastic scattering [Pa73].

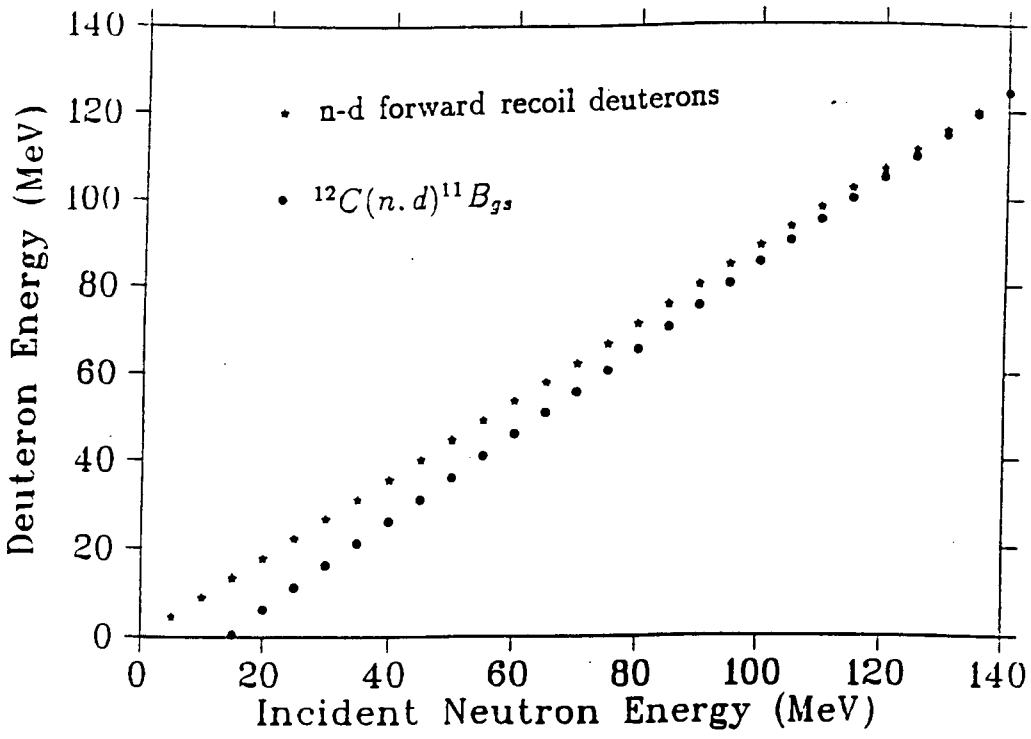

Figure 4.6: *Energy of the outgoing deuterons from the* ^{12}C(n,d)^{11}B$_{gs}$ *reaction and* n-d *elastic scattering as a function of incident neutron energy*

pared to the increase in the energy of the forward recoil deuterons. This can be seen in figure 4.6 which shows the energy of the forward recoil deuterons from n-d elastic scattering and the deuterons from ^{12}C(n,d)^{11}B$_{gs}$ reaction energy as a function of incident neutron energy.

4.1.3 The Proton Loci

The NE230 scintillator has a low content (see table 2.1) of free hydrogen nuclei (protons) i.e protons available for elastic scattering, therefore there is negligible n-p scattering in this scintillator unlike in the NE213 scintillator which has protons in the place of deuterons. A negligible proportion of the proton locus (p) in figures 4.3 and 4.4 is therefore made up of protons from n-p scattering. Nearly all of these protons are from neutron-induced breakup of the deuterons in the scintillator and from n-^{12}C interactions in the scintillator. Protons from the n-^{12}C interactions are released mainly from the ^{12}C(n,p)^{12}B, ^{12}C(n,np)^{11}B, ^{12}C(n,2np)^{10}B, and ^{12}C(n,2n2p)^{9}Be reactions. The protons in the escaping protons locus (e) are those which have a high energy and thus do not stop in the scintillator. Figure 4.7 shows the differential cross-section for the ^{12}C(n,p)^{12}B reaction measured at E_n = 56 MeV [Mc75]. From figure 4.7, it can be seen that this

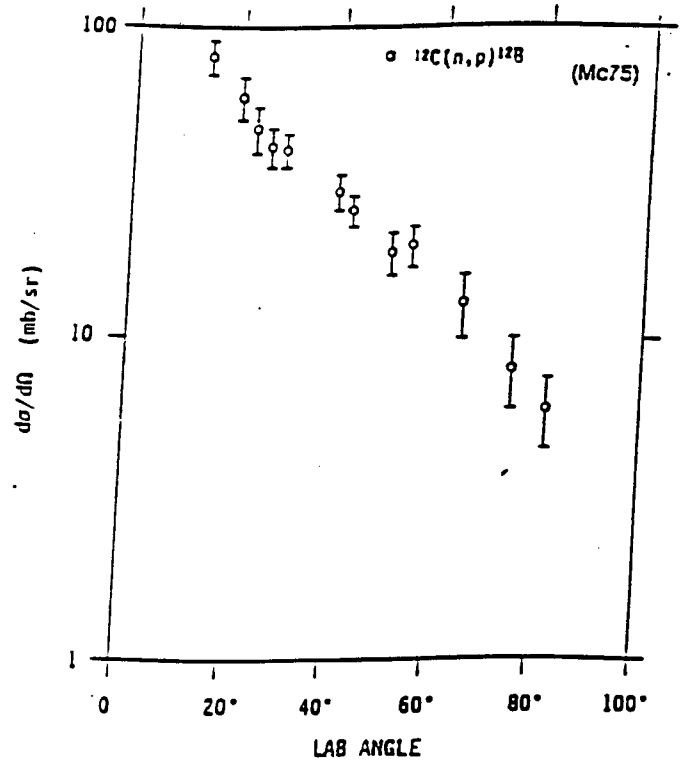

Figure 4.7: *Differential cross-section data for the* ^{12}C(n,p)^{12}B *reaction measured at* E_n = 56 *MeV.*

reaction is forward peaked in the laboratory frame at these energies, thus most of the escaping protons escape through the rear of the scintillator, as opposed to the sides.

4.2 The Coincidence Spectra

The coincidence system (see figure 2.2) was primarily used to collect the events from the ^{12}C(n,n')3α reaction selectively and to exclude the ^{12}C(n,α)^{9}Be$_{gs}$ reaction. The selection of the ^{12}C(n,n')3α reaction was enhanced by using pulse shape discrimination to select events in the NE213 scintillator which are associated with detection of the inelastically scattered neutrons. The NE213-NE230 coincidences also included events from n-^{12}C interactions in the NE230 scintillator, and n-d coincidences from neutrons elastically scattered by the deuterons in the NE230.

Figure 4.8 is a scatter plot of events as function of L and S, for coincidence events measured by the NE213 scintillator. The ridges correspond to gamma rays (γ) and neutrons labelled (p) in figure 4.8. The gamma rays detected by this scintil-

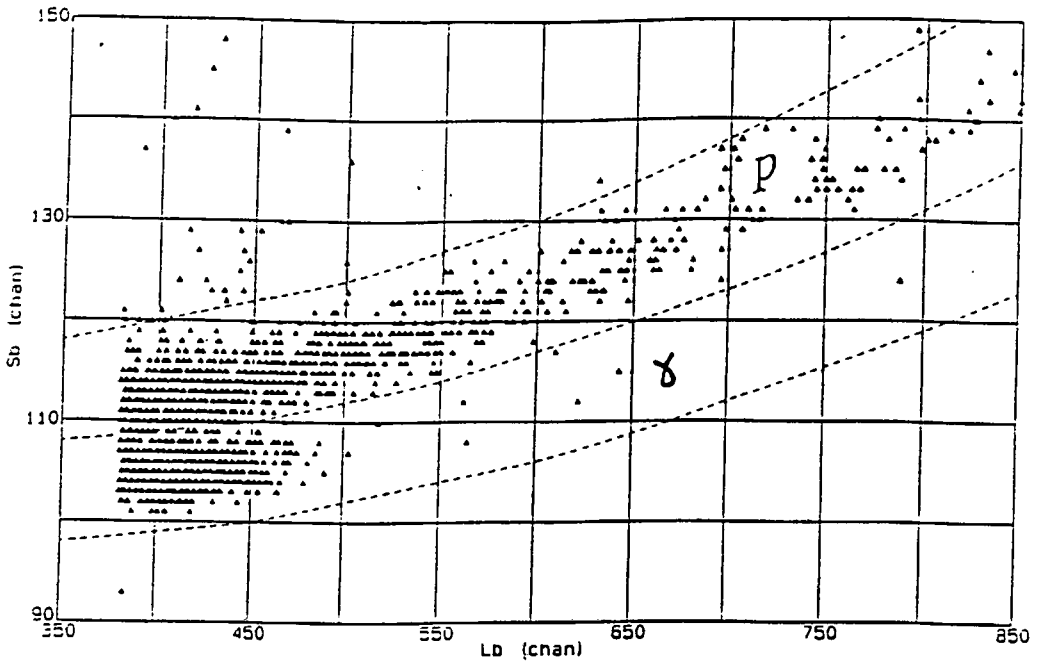

Figure 4.8: *Scatter plot of the "coincidence" events detected by the NE213 scintillator as a function of pulse height, L, and pulse shape, S.*

cidence events measured by the NE230 scintillator at different incident neutron energies in the range 20 to 56 MeV. The scatter plots for the singles already shown in figures 4.3 and 4.4 are reproduced in figures 4.9 and 4.10 to facilitate the comparison of singles and coincidences. The alphas, deuterons, protons and escaping proton loci in these spectra are the same as those in the singles LS spectra (figure 4.3). The corridors selecting the ridges in the coincidence LS spectra are also the same as those in the singles LS spectra in order to simplify the comparison of the spectra.

The events in the alpha locus of the coincidence scatter plots are mainly from the alpha particles released in ^{12}C(n,n')3α reactions. These events are concentrated at the high S region of the alpha locus. There are fewer events in the lower S region of the alpha locus, however, the number of these events increases as the incident neutron energy increases. This increase in the number of alpha particles with a lower pulse shape implies that there is a change in the scintillation output pulse of the alphas from the ^{12}C(n,n')3α reaction as the incident neutron energy increases. The change in the scintillation pulse height corresponds to the change in the distribution of the available energy amongst the alpha particles from this reaction as the incident neutron energy increases as explained in section 4.1.1. As E_n increases the first alpha particle is released with almost all the available

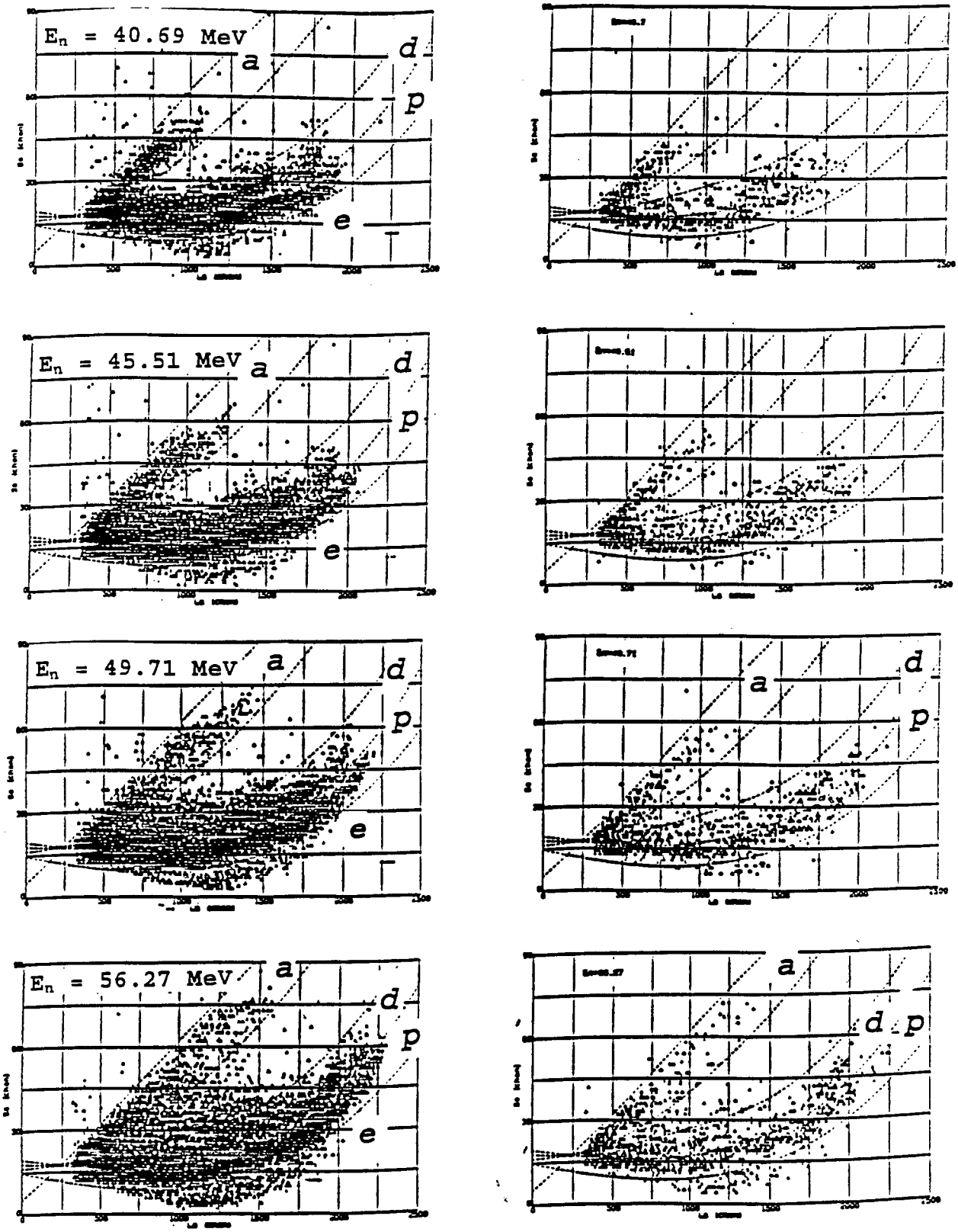

Figure 4.9: *Scatter plots of singles events (left) and coincidence events (right) as a function of pulse height and pulse shape at different incident neutron energies. The loci correspond to alphas, a, deuterons, d, protons, p, and escaping protons, e. True zero is located at $L_a = 200$ channels.*

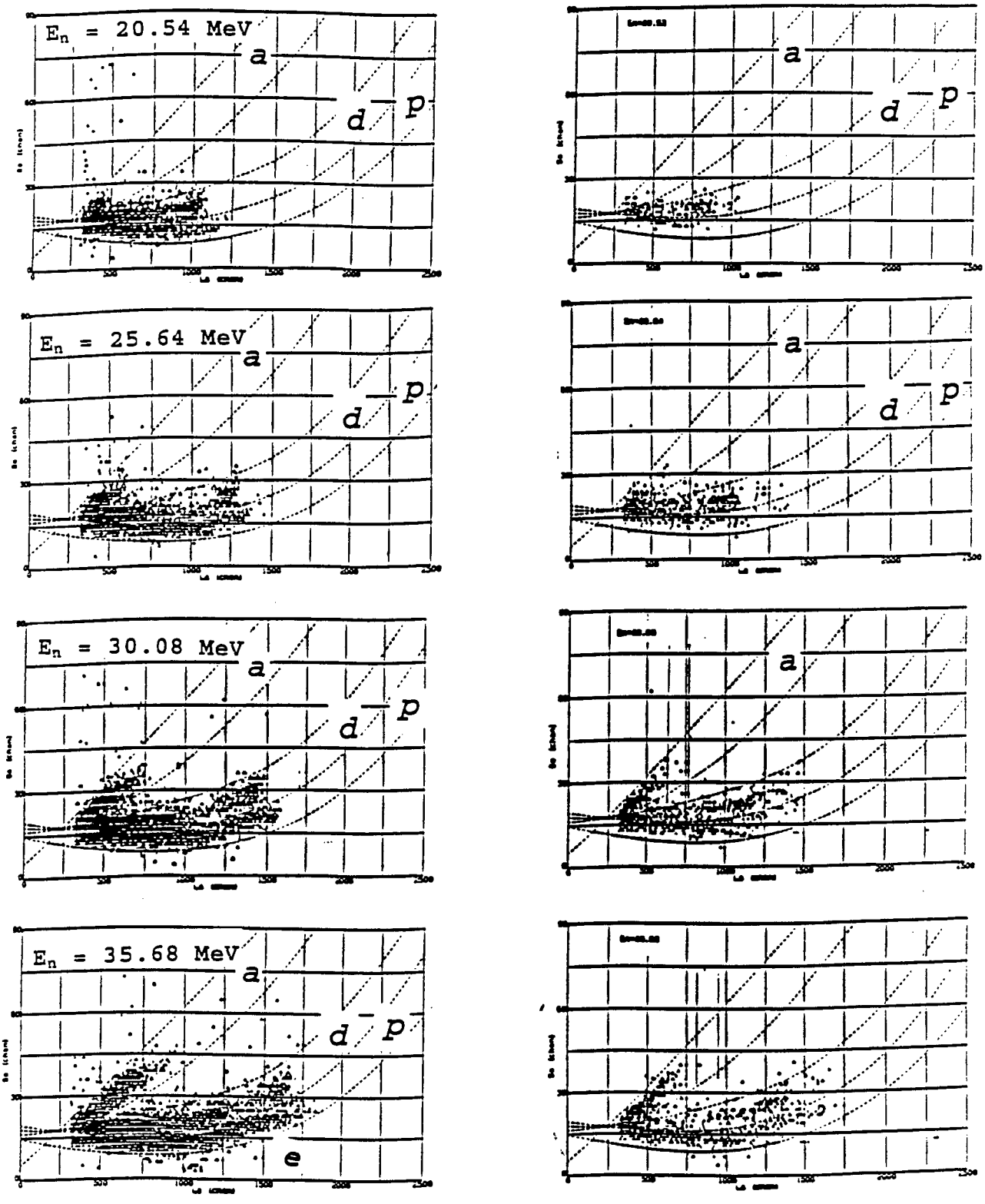

Figure 4.10: *Same as in figure 4.9 for incident neutron energies in the range 40-56 MeV.*

region of the alpha locus, however, the number of these events increases as the incident neutron energy increases. This increase in the number of alpha particles with a lower pulse shape implies that there is a change in the scintillation output pulse of the alphas from the ^{12}C(n,n')3α reaction as the incident neutron energy increases. The change in the scintillation pulse height corresponds to the change in the distribution of the available energy amongst the alpha particles from this reaction as the incident neutron energy increases as explained in section 4.1.1. As E_n increases the first alpha particle is released with almost all the available energy, the remaining energy is just enough for the breakup of the ^{8}Be nucleus into two alpha particles. The scintillation output pulse of the two alphas will approach that of the ^{8}Be nucleus as the incident neutron energy increases. Since the ^{8}Be nucleus is heavily ionizing, it contributes a negligible amount to the scintillation pulse height for the event, the first alpha particle is therefore the major contributor to the scintillation pulse height. Thus for incident neutron energies above 30 MeV, some alpha particles produced from the ^{12}C(n,n')3α reaction will have the same scintillation pulse height as those produced in the ^{12}C(n,α)^{9}Be$_{gs}$ reaction. This behaviour can be seen in figures 4.9 and 4.10 at $E_n > 40\ MeV$.

The deuteron locus has a peak at the high pulse height region which is attributed to the n-d elastic scattering at an angle of 90^0 in the NE230 scintillator. The other events in the deuteron locus are attributed mainly to the deuterons from the ^{12}C(n,nd)^{10}B reaction in the NE230 scintillator. The events in the proton locus are attributed mainly to the protons from the ^{12}C(n,np)^{11}B, ^{12}C(n,2np)^{10}B, and ^{12}C(n,2n2p)^{9}Be reactions in the NE230 scintillator.

4.3 The Singles Spectra at E_n = 195 MeV

Figure 4.11 is a perspective plot of counts versus pulse height, L, and pulse shape, S, for the events measured by the NE213 liquid scintillator, for incident neutrons of energy 195 MeV. The NE213 liquid scintillator used was in a 5 cm x 5 cm cylindrical capsule. From figure 4.12, which shows the range of the different charged particles in the NE213 liquid organic scintillator, it can seen that most alpha particles will stop in the scintillator and only a negligible amount will not stop in the scintillator. A large percentage of deuterons and protons will escape through the rear of the detector. The alpha particles will thus have the same features as those discussed in section 4.1.1 above.

The deuterons lying in the deuteron locus are those released mainly from the

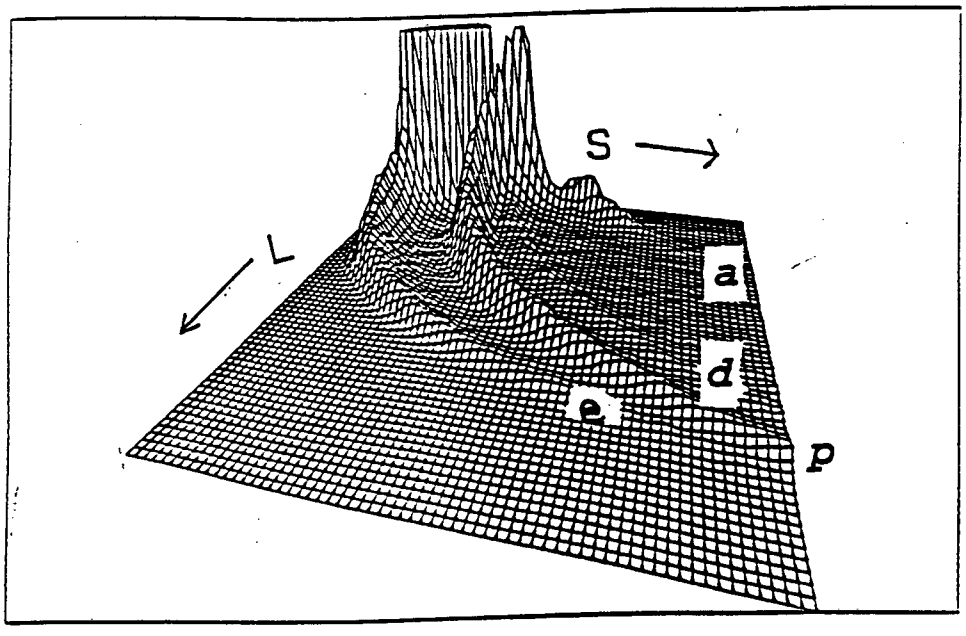

Figure 4.11: *Perspective view of counts (vertical) as a function of pulse height, L, and pulse shape parameter, S, events measured by an NE213 scintillator when exposed to neutrons of energy E_n = 195 MeV. The ridges corresponds to protons, p, escaping protons, e, deuterons, d, and alphas, a.*

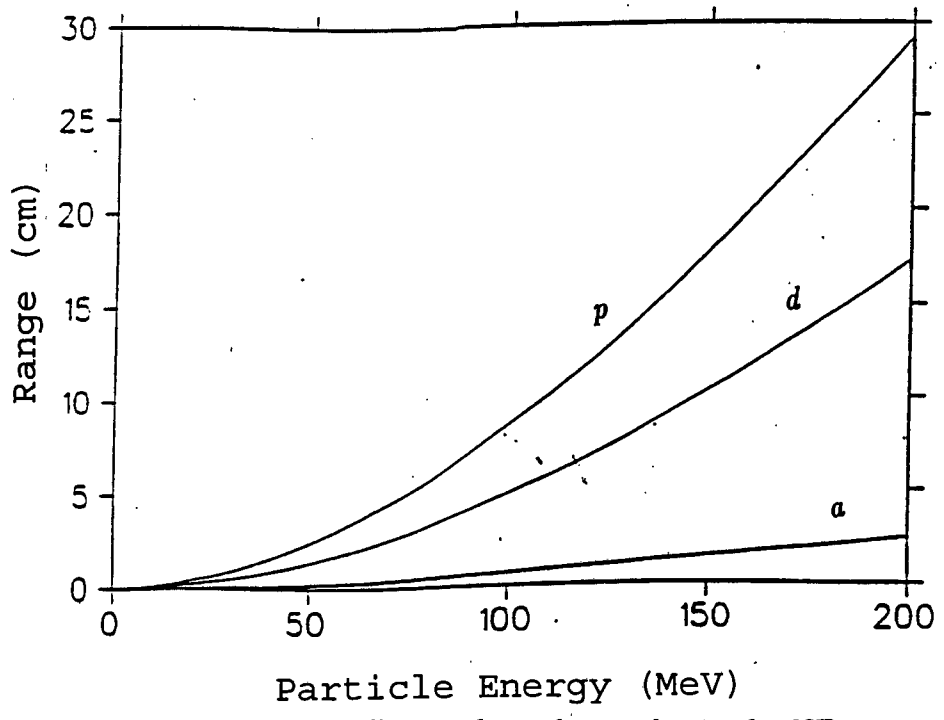

Figure 4.12: *Ranges of the different charged particles in the NE213 scintillator.*

$^{12}C(n,d)^{11}B$ and the $^{12}C(n,nd)^{10}B$ reactions. There is also a small fraction of deuterons from (n,p) capture reaction. A large fraction of the deuterons from $^{12}C(n,d)^{11}B$ reaction do not stop in the detector, since this reaction goes through to the ground state of the ^{11}B nucleus [Me67]. At this incident neutron energy (195 MeV) there are many escaping protons. This can be seen by the large number of events in the escape protons locus in figure 4.11, compared to that in figure 4.2.

The analysis in this chapter showed that the alpha particles released from the $^{12}C(n,\alpha)^{9}Be$ and $^{12}C(n,n')3\alpha$ reactions have different pulse shape parameters. The alpha particles from these reaction could therefore be separated by setting up subcuts in the alpha locus in the PSD plane.

Chapter 5

Calculation of Cross-sections

The measurements and data reduction described in chapters 2 and 3 have resulted in L-S spectra from which pulse height distributions for alpha particles (figure 3.11) and forward recoil deuterons (figure 3.10) from n-d elastic scattering were obtained. Pulse height spectra for alpha particles and deuterons were analysed and peaks corresponding to various reactions and interactions identified. Integrals of peaks corresponding to alpha particles from two alpha producing reactions in the alpha pulse height spectra and integrals of peaks from the forward recoil deuterons from n-d elastic scattering were measured for different incident neutron energies. Ratios of these integrals were used in conjunction with known cross-sections for n-d backward elastic scattering to calculate alpha production cross-sections. Cross-sections were measured for production of alpha particles from $^{12}C(n,\alpha)^{9}Be_{gs}$ and $^{12}C(n,n')3\alpha$ reactions.

5.1 Analysis of Pulse Height Spectra

Pulse height spectra for alpha particles (figure 3.11) and deuterons (figure 3.10) were measured for different incident neutron energies by setting appropriate T_n windows to select E_n and cuts on the L-S spectra to select alphas and deuterons (see figure 3.3 and 3.4), and projecting the events in the 2D spectrum cut onto the L-axis.

5.1.1 Alpha Spectra

From the discussion in section 1.1.2 on the mechanism for alpha production from ^{12}C following interaction with neutrons, it was shown that major reaction path-

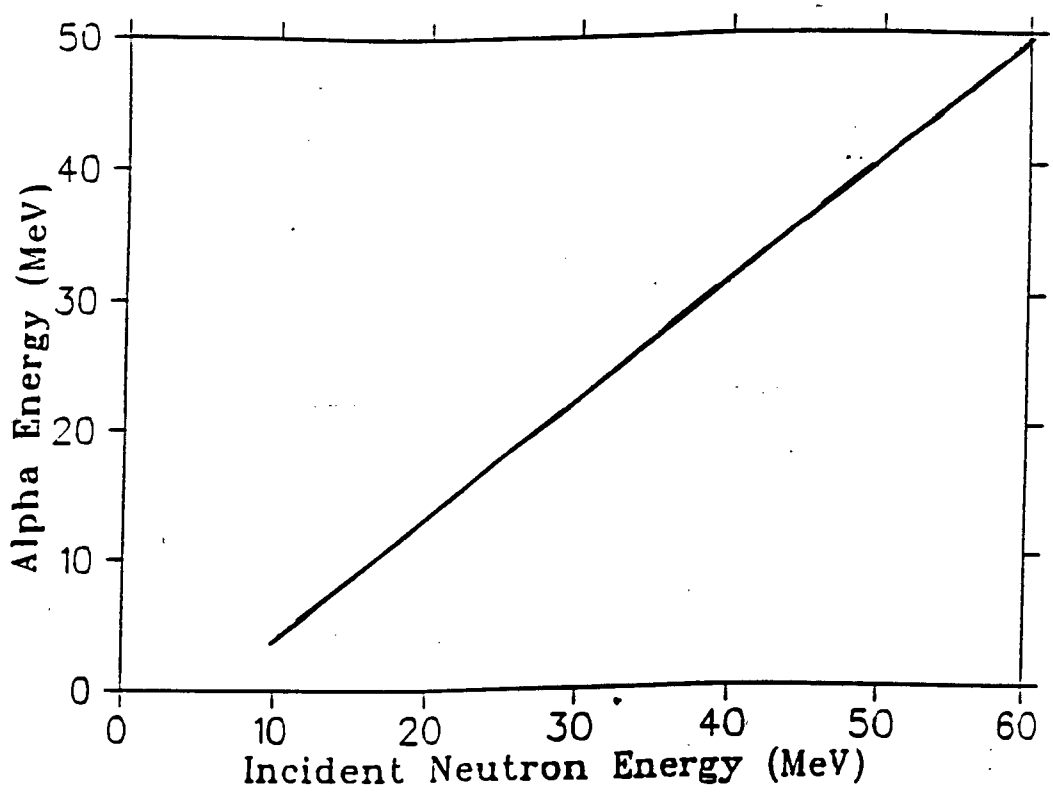

Figure 5.1: *Energy of the outgoing alpha particle from the* $^{12}C(n,\alpha)^{9}Be_{gs}$ *reaction as a function of the incident neutron energy.*

ways for alpha production are $^{12}C(n,\alpha)^{9}Be$ (Q = -5.79 MeV) and $^{12}C(n,n')3\alpha$ (Q = -7.65 MeV). It was also shown that the only mechanism which produces a single alpha particle is the ground state transition of the $^{12}C(n,\alpha)^{9}Be$ reaction. If the ^{9}Be is left in any of its excited states, it decays to two alpha particles and a neutron. Previous work [An83] has indicated that the dominant mechanisms for the decay of ^{12}C into three alpha particles are the $^{12}C(n,\alpha)^{9}Be^{*}(n',^{8}Be^{*}(2\alpha))$ and $^{12}C(n,n')^{12}C^{*}(\alpha,^{8}Be^{*}(2\alpha))$ decay paths.

The alpha particles released from the n-^{12}C interaction have energies which vary from zero to approximately (E_n - E_{th}), where E_{th} is the threshold neutron energy for the production of the alpha particles from the $^{12}C(n,\alpha)^{9}Be_{gs}$ reaction. From the reaction kinematics, the alpha particles with the maximum energy will be from $^{12}C(n,\alpha)^{9}Be_{gs}$ reaction. Figure 5.1 shows the maximum possible alpha energy as a function of the incident neutron energy. The energy of the alpha particles was calculated using the standard non-relativistic kinematic equations (appendix B).

Figure 5.2 shows the pulse height spectrum of the alpha component at the incident neutron energy of 45 MeV, measured in the NE230 scintillator for the

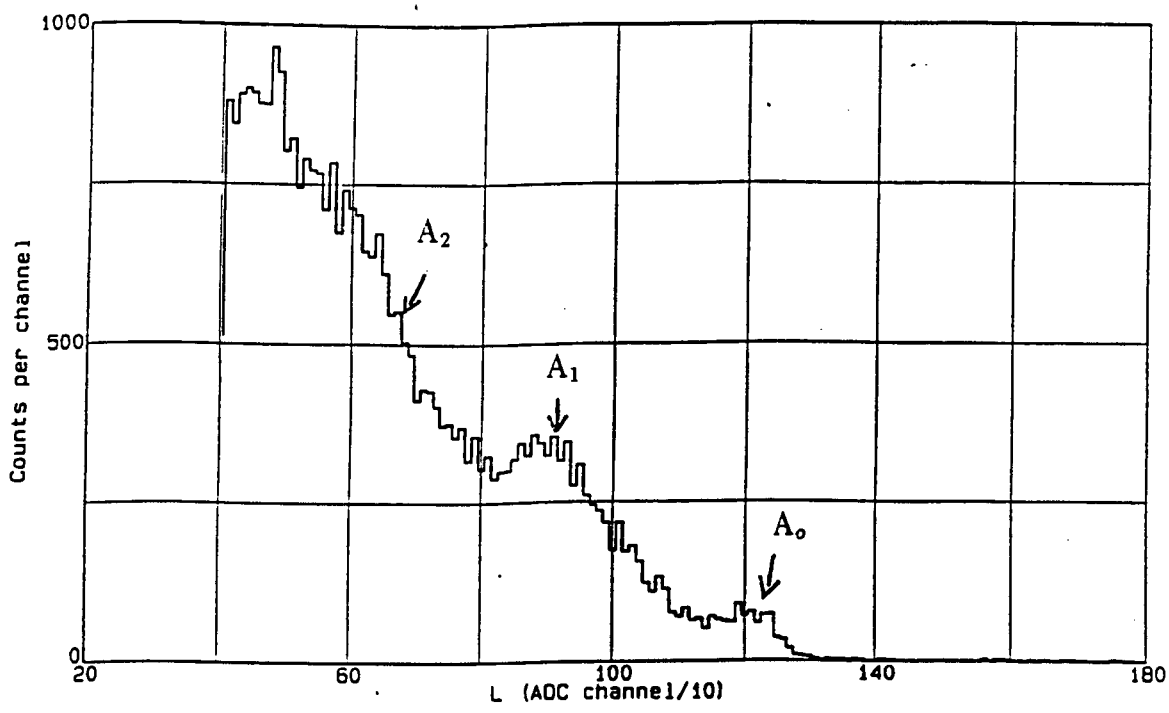

Figure 5.2: *Counts versus pulse height for singles events identified as alpha particles by PSD at an incident neutron energy of 45 MeV. See text for details.*

singles events. The spectrum was obtained by setting a window on the T_n parameter and an LS cut on the L-S spectrum (see figure 3.2) for singles events measured by the NE230 scintillator, and projecting the events onto the L-axis. The spectrum (see figure 5.2) has several peaks which are attributed to the different alpha particles from the carbon-12 decay. The existence of these peaks is attributed to the difference in the scintillation light output of the alpha particles emitted through the different reaction mechanisms. These alpha particles have different energies and thus different scintillation light outputs (pulse heights) in accordance to Birks' formula (see equation 4.1). The peak labeled A_o in figure 5.2 has been identified with the alpha particle released from the ground state transition of the $^{12}C(n,\alpha)^9Be$ reaction. The peaks labeled A_1 and A_2 in figure 5.2 are attributed to the alpha particles from the $^{12}C(n,n')3\alpha$ reaction. The existence of two peaks might be attributed to different ways in which the available energy could be distributed between the three alpha particles. The peak labeled A_2 is attributed to the case in which the energy is equally distributed between the three alpha particles. The peak labeled A_1 in the spectrum results from the situation in which the first alpha particle is released with a larger fraction of the available energy than the other two alpha particles in the $^{12}C(n,\alpha)^9Be^*(n',^8Be^*(2\alpha))$ and $^{12}C(n,n')^{12}C^*(\alpha,^8Be^*(2\alpha))$ decay paths. As the incident neutron energy increases (see figures 3.10, 4.3 and 4.4) this peak moves closer to peak A_0 until they overlap at E_n >50 MeV. As explained in section 4.1.1, this is caused by the change

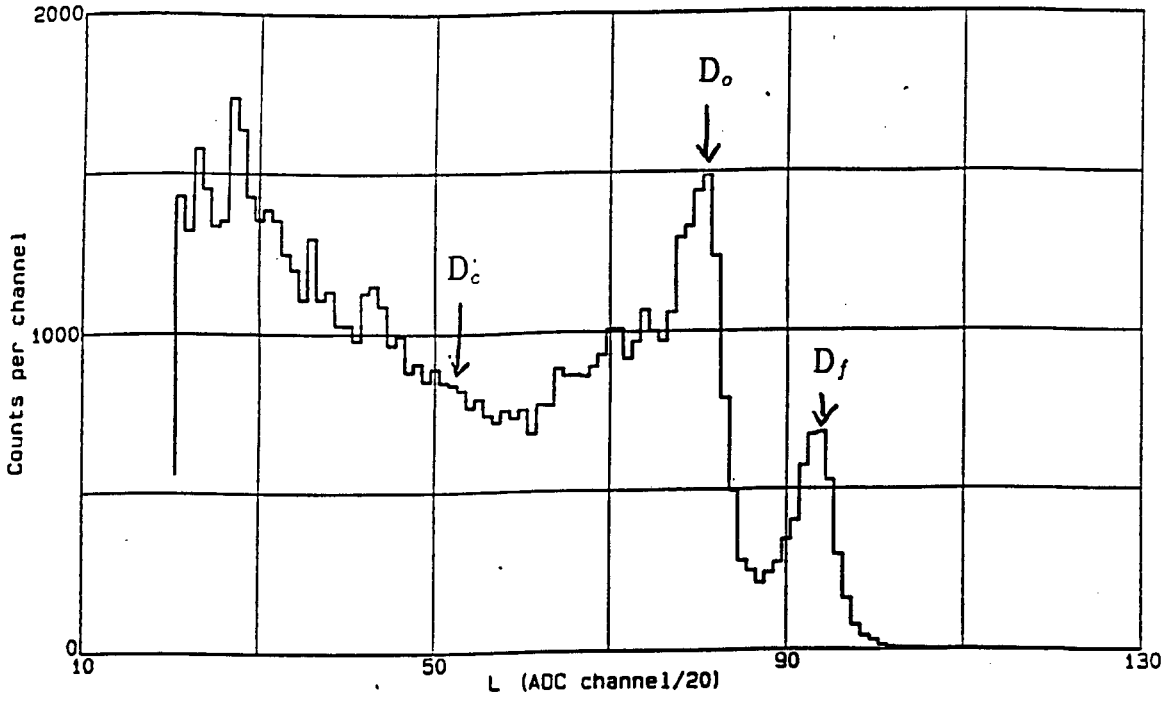

Figure 5.3: *Counts versus pulse height for singles events identified as deuterons, at an incident neutron energy of 45 MeV. See text for details.*

in the energy distribution amongst the three alpha particles produced from the ^{12}C(n,n')3α reaction. As the incident neutron energy increases, the first alpha particle is released with an increasingly higher fraction of the available energy (thus having a higher pulse height), and the remaining energy is shared by the other two alpha particles. The continuum at a lower pulse height region is attributed to the other two alphas released via this decay path. This continuum starts as a broad peak at low incident neutron energies and broadens as the incident neutron energy increases.

5.1.2 Deuteron Spectra

Figure 5.3 shows the pulse height spectrum of the deuteron component at the incident neutron energy of 45 MeV, measured by the NE230 scintillator for the singles events. This spectrum was obtained by setting a window on the T_n parameter and an LS cut on the L-S spectrum (see figure 3.3), for singles events measured by the NE230 scintillator, and projecting the events onto the L-axis. The dominant features of the spectrum are the two peaks (D_f and D_o in figure 5.3). The peak at the higher pulse height region (D_f) is attributed to deuterons recoiling forward from the D(n,n)D backward scattering. The other peak (D_o) is attributed to the

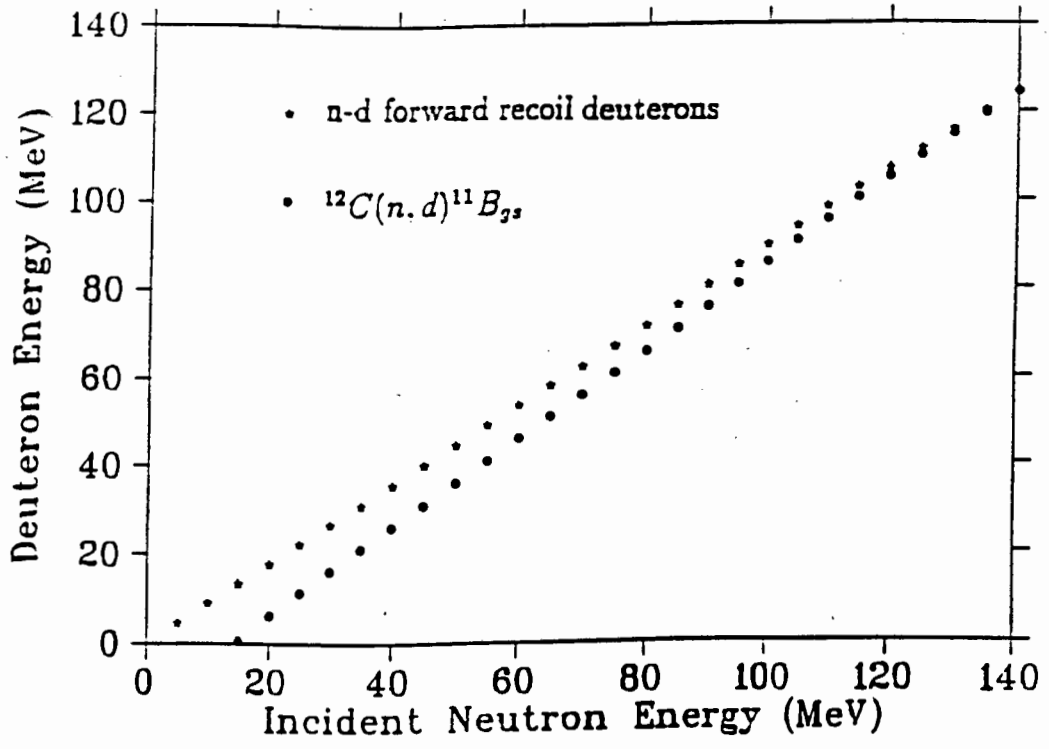

Figure 5.4: *Energy of the outgoing deuterons from* D(n,n)D *backward scattering and* ^{12}C(n,d)^{11}B *reaction as a function of the incident neutron energy.*

deuterons from the ground state transition of the ^{12}C(n,d)^{11}B reaction [Me67]. There is also a continuum (D_c in figure 5.3), arising from the deuterons released from the ^{12}C(n,nd)^{10}B and ^{12}C(n,d)^{11}B reactions to the excited states of ^{11}B, which stretches down to the lower pulse height region. Deuterons from n-d elastic scattering also contribute to the continuum. As the incident neutron energy increases (see figures 4.2 and 4.3) the peak corresponding to the ^{12}C(n,d)$^{11}B_{gs}$ reaction moves closer to the n-d forward elastic scattering peak until they overlap at E_n >50 MeV. This is due to the differences between the kinematics for D(n,n)D and ^{12}C(n,d)^{11}B. Figure 5.4 shows the variation of deuteron energy with incident neutron energy for these two categories of deuterons. The deuteron energies were calculated using the standard non-relativistic kinematic equations (appendix B). Figure 5.4 shows that as the incident neutron energy increases, the energy of the deuterons released from the ^{12}C(n,d)$^{11}B_{gs}$ reaction increases at a faster rate than that of the deuterons recoiling forward from the n-d elastic scattering. At E_n >117 MeV the energy of the deuterons from the n-^{12}C interaction is greater than that of the forward recoil deuterons from the n-d elastic scattering.

5.2 Calculation of Cross-sections

Cross-sections for the production of alpha particles were calculated by using the method similar to that used by Stevens [St76]; i.e. comparing the yield of alpha particles with the yield for forward recoiling deuterons from n-d elastic scattering. The integrals of peaks corresponding to alpha particles from the two reactions producing alpha particles and that of the forward recoil deuteron peak from n-d elastic scattering were measured as a function of incident neutron energy. The ratio of these integrals was used together with the cross-section data for n-d backward elastic scattering data to calculate alpha production cross-sections from ^{12}C(n,α)^{9}Be$_{gs}$ and ^{12}C(n,n')3α reactions. The differential cross-section data for n-d elastic scattering has a minimum at neutron centre-of-mass scattering angle (θ_{com}) of about 120^0 (see figure 4.5). There is a corresponding minimum ("b" in figure 5.7) in the deuteron pulse height spectrum for singles events. The integral of the differential cross-section for n-d elastic scattering at $\theta_{com} > 120^0$ gives the cross-section, σ_{fwd}, for deuterons in the forward recoil deuteron peak (D_f in figure 5.3). At incident neutron energies above 14 MeV there is no appreciable difference due to Coulomb scattering [Va67] between the n-d and p-d data except for Coulomb interference at small forward scattering angles. Consequently, both n-d and p-d data may be used to obtain the integral σ_{fwd} as a function of incident neutron energy. Values of σ_{fwd} used in this work are from the calculations of Pauletta [Pa73]. Figure 5.5 shows the σ_{fwd} values as a function of incident nucleon energy from the work of Pauletta. Also shown in figure 5.5 are the values of σ_{fwd} obtained using Ludin's parameterisation [Lu70] of the differential elastic cross-section.

Figures 5.6 and 5.7 show schematic plots of the expected pulse height spectra for singles events identified as alpha particles and deuterons by PSD respectively in the NE230 scintillator. Figure 5.6a is a schematic plot of the expected pulse height spectrum for singles events identified as alpha particles by PSD in the NE230 scintillator. The plot can be separated into two components as shown in figure 5.6. The component in (b) is attributed to alpha particles from the ^{12}C(n,n')3α reaction and the component in (c) is attributed to alpha particles from the ^{12}C(n,α)^{9}Be$_{gs}$ reaction. From figure 5.6 it can be seen that the peak corresponding to alpha particles from the ^{12}C(n,α)^{9}Be$_{gs}$ reaction includes some events from the ^{12}C(n,n')3α reaction and vice versa. The shaded regions in figure 5.6 show the area that would be integrated to find the number of events in the peaks. The cut-off points in the integrated areas are determined by estimating the lowest point in the region between the two peaks. The point marked "b_1" in figure 5.6 show the estimated cut off point of the two peaks. This point ("b_1") is chosen in such a way that the events in the peak which have been "left out" are compensated for by the events from the adjacent peak. The shaded regions in

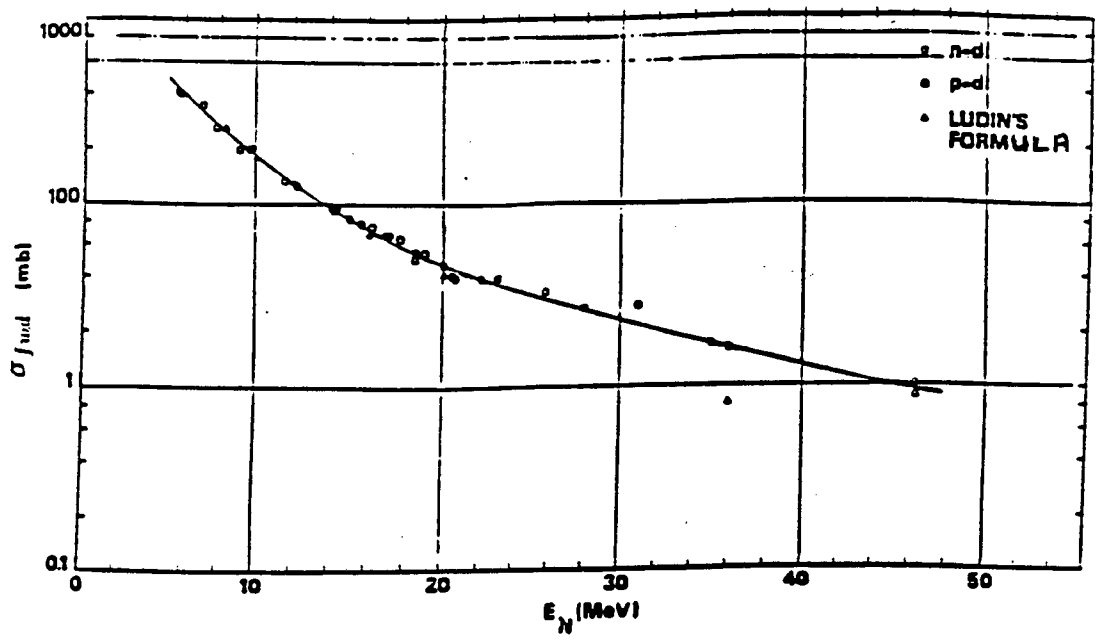

Figure 5.5: *Cross-section data for the forward recoil deuterons from* n-d *and* p-d *elastic scattering as a function of incident nucleon energy. Also shown are values obtained using Ludin's formula [Pa73].*

figure 5.6 show areas in the spectrum which when integrated yield the observed number of alpha particles (N_α and $N_{3\alpha}$) corresponding to alpha particles from ^{12}C(n,α)^{9}Be$_{gs}$ and ^{12}C(n,n')3α reactions respectively. The compensation is not exact, it depends on the accuracy of choosing point b_1 and thus there is a systematic uncertainty in the estimation of the observed number of alpha particles N_α and $N_{3\alpha}$. This systematic uncertainty is estimated to be less than 1%. Similarly figure 5.7a is a schematic plot of the expected pulse height spectrum for singles events identified as deuterons by PSD in the NE230 scintillator. The component in (b) is attributed to the forward recoil deuterons from n-d elastic scattering. This component includes some events from the ^{12}C(n,d)^{11}B reaction. The integral of the shaded region in figure 5.7 gives the observed number of forward recoil deuterons (N_d) from n-d elastic scattering in the NE230 scintillator.

When N_o neutrons per unit area are incident on the deuterated organic scintillator, the numbers of charged particles measured by the scintillator for different interactions are given by the following relations:

$$N_\alpha = \epsilon_\alpha N_o (1 - T) \frac{n_c \sigma_\alpha}{(n_c \sigma_{nc} + n_d \sigma_{nd})} \tag{5.1}$$

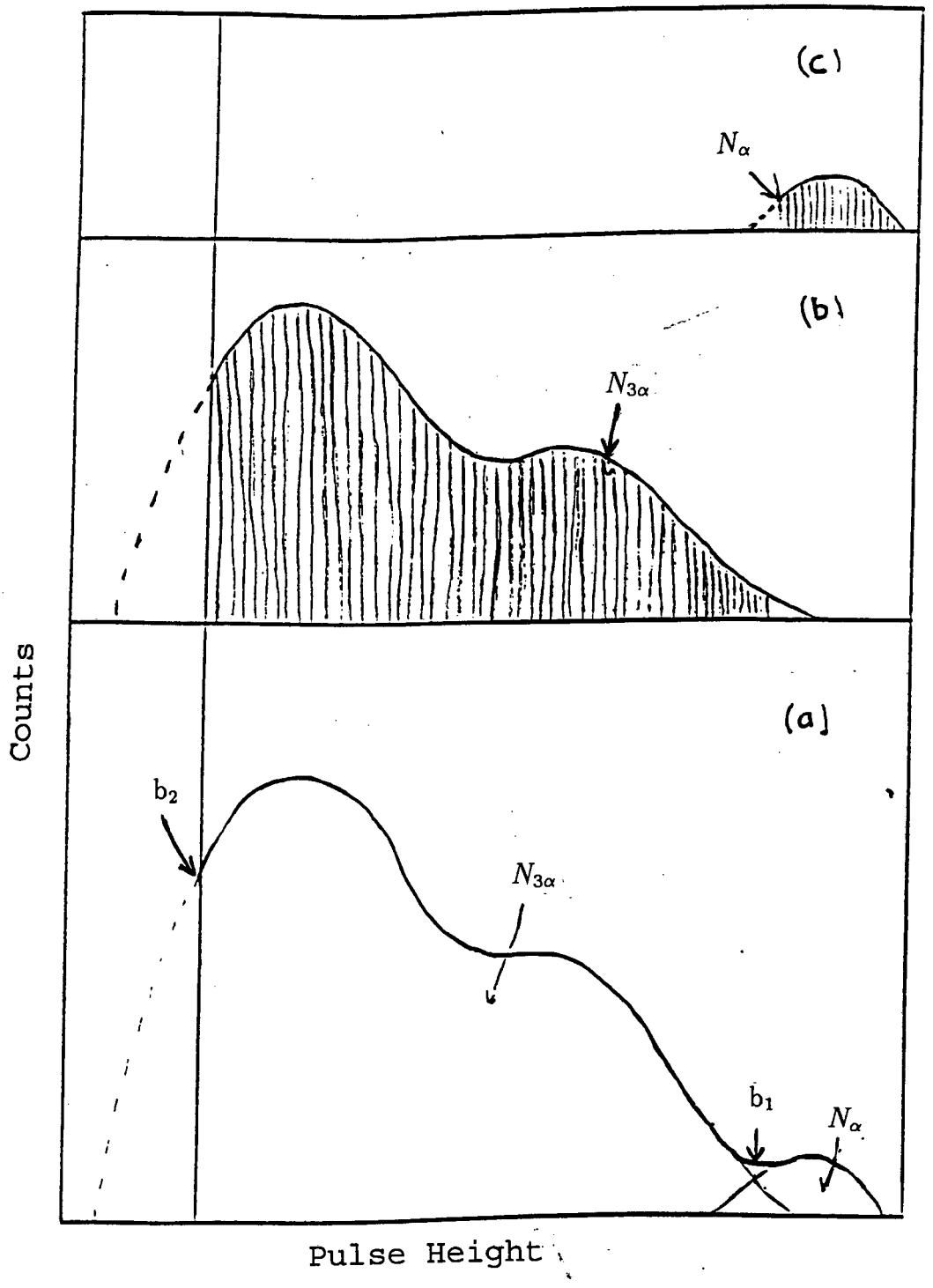

Figure 5.6: *Schematic plot of the expected pulse height spectrum for singles events identified as alpha particles by PSD in the NE230 scintillator. Shown in (a) is the overall pulse height spectrum which would be observed for alpha particles, (b) shows the component of the spectrum which is attributed to alpha particles from the* ^{12}C(n,n')3α reaction. *(c) shows the component of the spectrum which is attributed to alpha particles from the* ^{12}C(n,α)^{9}Be$_{gs}$ *reaction. The integrals of the shaded regions in the spectra would give the number of alpha particles (N_α and $N_{3\alpha}$), see text for details.*

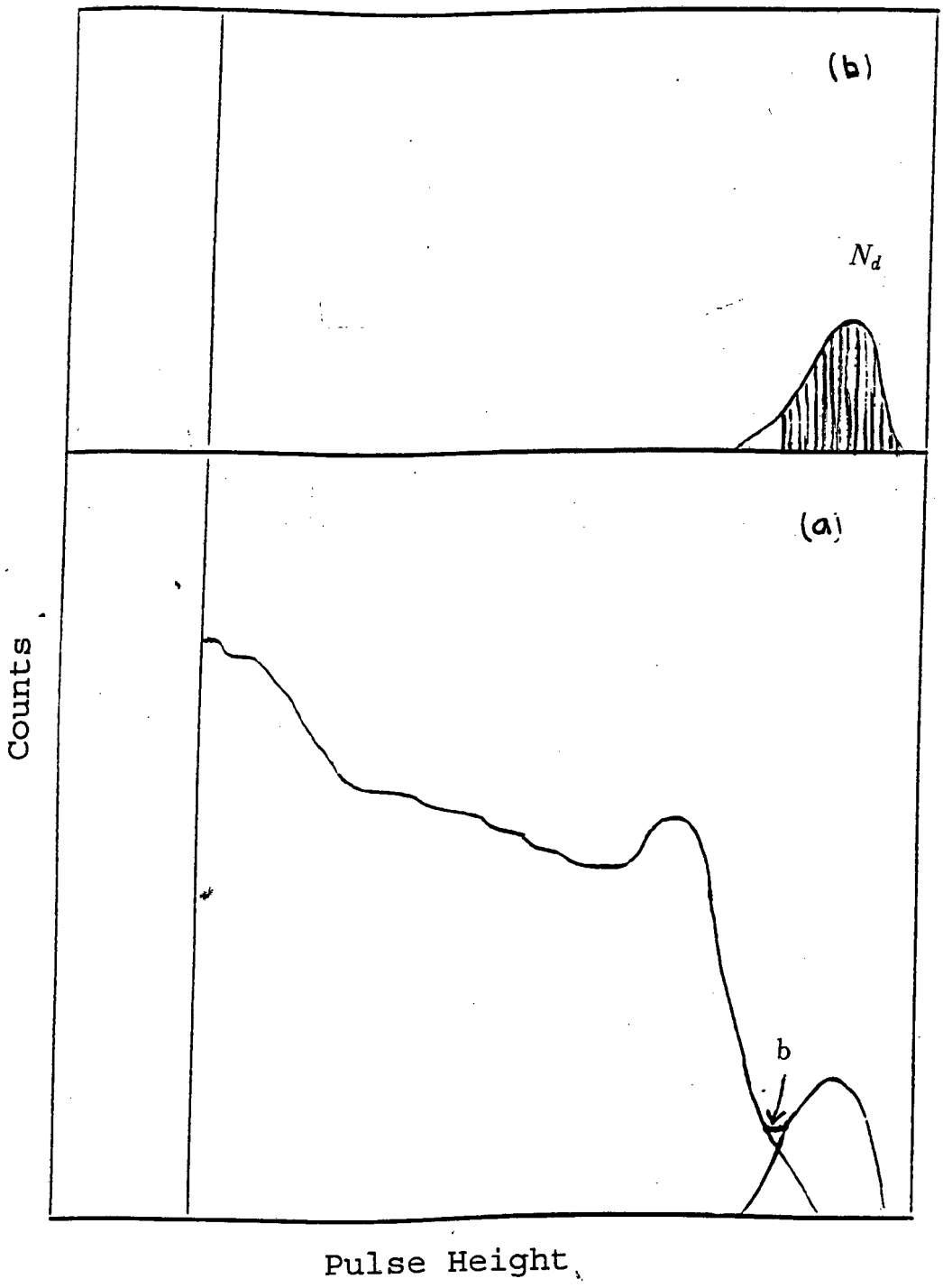

Figure 5.7: *Schematic plot of the expected pulse height spectrum for singles events identified as deuterons by PSD in the NE230 scintillator. Shown in (a) is the overall pulse height spectrum which would be observed for deuterons, (b) show the component of the spectrum which is attributed to the forward recoil deuterons from n-d elastic scattering. The integral of the shaded region would give the number of forward recoil deuterons (N_d), see text for details.*

$$N_{3\alpha} = \epsilon_{3\alpha} N_o (1 - T) \frac{n_c \sigma_{3\alpha}}{(n_c \sigma_{nc} + n_d \sigma_{nd})} \quad (5.2)$$

$$N_d = \epsilon_d N_o (1 - T) \frac{n_d \sigma_{fwd}}{(n_c \sigma_{nc} + n_d \sigma_{nd})} \quad (5.3)$$

where:

n_c : number of carbon nuclei per unit area perpendicular to beam in the scintillator
n_d : number of deuterons per unit area perpendicular to beam in the scintillator
σ_{nc} : total cross-section for n-^{12}C interactions
σ_{nd} : total cross-section for n-d interactions
σ_{fwd} : cross-section for deuterons in the forward recoil deuteron peak (see text above)
ϵ_α, $\epsilon_{3\alpha}$, ϵ_d : efficiencies of separation of the peaks (see text below)
σ_α, $\sigma_{3\alpha}$: cross-sections for the production of alpha particles

The fraction of incident neutrons transmitted through the scintillator without an interaction of any kind, T, is given by the relation:

$$T = e^{-(n_c \sigma_{nc} + n_d \sigma_{nd})} \quad (5.4)$$

Taking the ratios between equations 5.1, 5.2 and 5.3 gives:

$$\sigma_\alpha = \frac{\epsilon_d}{\epsilon_\alpha} \frac{N_\alpha}{N_d} \frac{n_c}{n_d} \sigma_{fwd} \quad (5.5)$$

for the ^{12}C(n,α)^{9}Be$_{gs}$ reaction.

and

$$\sigma_{3\alpha} = \frac{\epsilon_d}{\epsilon_{3\alpha}} \frac{N_{3\alpha}}{N_d} \frac{n_c}{n_d} \sigma_{fwd} \quad (5.6)$$

for the ^{12}C(n,n')3α reaction.

The number of particles corresponding to a particular reaction is found by selecting the peak corresponding to those particles (see figures 5.2 and 5.3) and integrating the area in the peak as shown in figures 5.6 and 5.7. The points marked "b", "b_1" and "b_2" in figures 5.6 and 5.7 indicate cut-off points used in the estimation of N_α, $N_{3\alpha}$ and N_d.

In the equations above, ϵ_α, $\epsilon_{3\alpha}$ and ϵ_d are the efficiencies for the measurements of the integrals in order to obtain the number of charged particles N_α, $N_{3\alpha}$ and N_d in the pulse height spectra. These efficiencies were calculated using:

$$\epsilon = \frac{I_{measured}}{I_{total}} \quad (5.7)$$

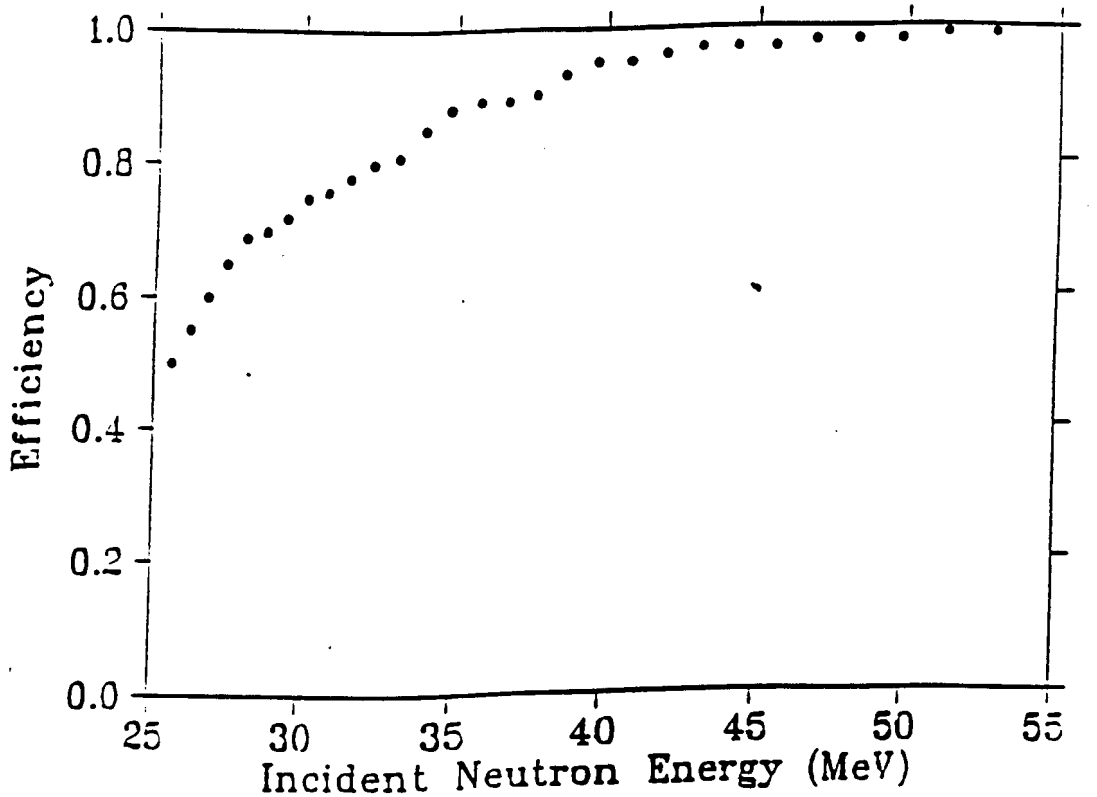

Figure 5.8: *Estimated efficiency ($\epsilon_{3\alpha}$) as a function of incident neutron energy for the detection of alpha particles from the* ^{12}C(n,n')3α *reaction. There is a scale uncertainty of about* 1% *on these efficiency values.*

$I_{measured}$ in equation 5.7 is the integral of the number of events within the boundaries "b", "b_1" and "b_2" shown in figures 5.6 and 5.7, and I_{total} is the total number of events in the peak in the pulse height spectrum. The integral (I_{total}) includes the estimated number of events below the detector threshold ("b_2" in figure 5.6) in the pulse height spectrum. The area below the detector threshold ("b_2" in figure 5.6) was estimated by fitting a Gaussian to the peak next to the detector threshold as shown in figure 5.6. The number of events below the detector threshold was estimated by finding the ratio of the area below point "b_2 and the area above point "b_2" in the fitted Gaussian.

Figure 5.8 and table 5.1 show the efficiency for the measurement of alpha particles from the ^{12}C(n,n')3α reaction as a function of incident neutron energy. The measurement of this efficiency have a systematic uncertainty of about 1%, which is due to the rough estimation of the fitted Gaussian on the peaks on the peaks next to the detector threshold in the alpha pulse height spectrum ("see figure 5.6 and A_2 in figure 5.2). Using equation 5.7 the efficiency for measurement of alpha particles from the ^{12}C(n,α)^{9}Be$_{gs}$ reaction was found to be unity at all incident neutron energies. The efficiency for the measurement of the n-d forward recoil deuterons, ϵ_d, is assumed to be unity in the energy range 25 to 52 MeV because of the relatively good separation of the forward recoil peak from the other peaks in the spectrum. Above 52 MeV the efficiency decreases because of the overlap

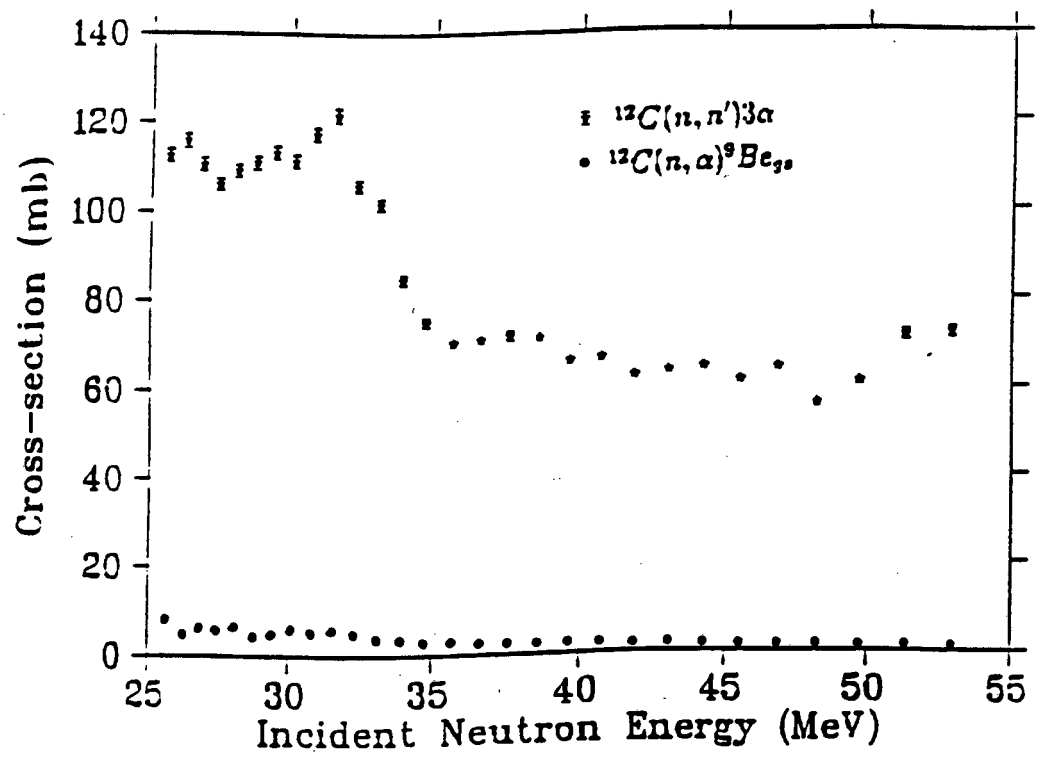

Figure 5.9: *Alpha production cross-sections as a function of incident neutron energy, measured in this work, for the* ^{12}C(n,α)^{9}Be$_{gs}$ *and* ^{12}C(n,n')3α *reactions. The error bars show the statistical uncertainties in the measurements, the systematic uncertainties in the measurements are not included.*

of the peak from the ^{12}C(n,d)^{11}B reaction and the n-d forward recoil deuteron peak (see figure 3.9).

Figure 5.9 and table 5.1 show the cross-section data obtained in this work, namely cross-sections for the production of alpha particles from the two alpha producing reactions as a function of E_n. The projected alpha pulse height spectrum could only be analysed for incident neutron energies above 25 MeV because of the insufficient separation of alpha particles and deuterons in the LS spectra at low pulse height region, the detector bias and the electronic thresholds. Above 52 MeV, there is a greater overlap of the peak corresponding ^{12}C(n,d)^{11}B$_{gs}$ reaction with the n-d forward recoil deuteron peak. There would thus be a large uncertainties in the measurement of the integral for the observed number of forward recoil deuterons N_d for incident neutron energies above 52 MeV.

E_n (MeV)	$\sigma_{n\alpha}$ (mb)	$\sigma_{n3\alpha}$ (mb)	σ_{fwd} (mb)	$\epsilon_{3\alpha}$
25.64	8.07 ± 0.18	112.5 ± 1.4	32.56	0.50
26.27	4.72 ± 0.13	115.8 ± 1.5	30.35	0.55
26.86	6.22 ± 0.15	110.5 ± 1.4	28.34	0.60
27.46	5.53 ± 0.14	106.0 ± 1.3	26.94	0.65
28.08	6.46 ± 0.16	109.1 ± 1.4	26.33	0.69
28.73	4.28 ± 0.12	110.9 ± 1.4	26.33	0.70
29.39	4.88 ± 0.13	113.1 ± 1.4	26.94	0.72
30.08	5.93 ± 0.15	111.3 ± 1.4	27.14	0.75
30.80	4.99 ± 0.14	117.5 ± 1.4	27.74	0.76
31.54	5.71 ± 0.15	121.8 ± 1.6	26.53	0.78
32.31	4.77 ± 0.13	106.0 ± 1.3	24.52	0.80
33.12	3.66 ± 0.11	101.7 ± 1.3	21.71	0.81
33.94	3.40 ± 0.10	84.5 ± 1.1	19.19	0.85
34.74	2.66 ± 0.08	75.1 ± 1.0	17.17	0.88
35.68	2.86 ± 0.08	70.5 ± 0.9	15.76	0.89
36.61	2.36 ± 0.08	71.0 ± 0.9	14.95	0.89
37.57	2.41 ± 0.08	71.9 ± 1.0	14.34	0.90
38.57	2.12 ± 0.07	71.4 ± 0.9	13.74	0.93
39.62	2.21 ± 0.07	65.9 ± 0.9	12.73	0.95
40.69	2.00 ± 0.07	66.5 ± 0.9	12.32	0.95
41.83	1.66 ± 0.06	62.6 ± 0.9	11.72	0.96
43.01	1.82 ± 0.06	63.6 ± 0.9	11.11	0.97
44.23	1.54 ± 0.06	64.4 ± 0.9	10.91	0.97
45.51	1.41 ± 0.05	61.3 ± 0.9	10.30	0.97
46.85	1.35 ± 0.05	64.1 ± 0.9	9.89	0.98
48.25	1.29 ± 0.05	55.9 ± 0.8	9.69	0.98
49.71	1.14 ± 0.05	60.9 ± 0.9	9.69	0.98
51.24	1.16 ± 0.05	71.4 ± 1.1	9.49	0.99
52.84	1.05 ± 0.05	72.1 ± 1.1	9.49	0.99

Table 5.1: *Alpha production cross-section data as measured in this work for the* ^{12}C(n,α)^{9}Be$_{gs}$ *and* ^{12}C(n,n')3α *reactions. Shown also in the table are* σ_{fwd} *values from calculations by Pauletta [Pa73] and efficiency values calculated for* $\epsilon_{3\alpha}$ *as a function of incident neutron energy. Statistical uncertainties are also shown in the table.*

5.3 Uncertainties

The statistical uncertainties in the calculation of the alpha production cross-sections are mainly due to the uncertainties in the measurement of the integrals (N_α, $N_{3\alpha}$ and N_d) of the peaks in the alpha and deuteron pulse height spectra (figures 5.6 and 5.7). These uncertainties were calculated as follows:

$$\Delta\sigma_\alpha = \sigma_\alpha \sqrt{\left(\frac{\Delta N_\alpha}{N_\alpha}\right)^2 + \left(\frac{\Delta N_d}{N_d}\right)^2} \tag{5.8}$$

As explained in section 3.3.1, the background count rate is negligible (see figure 3.5), thus the uncertainty in the integral of the peaks is calculated using:

$$\Delta N = \sqrt{N}$$

and equation 5.8 becomes

$$\Delta\sigma_\alpha = \sigma_\alpha \sqrt{\frac{1}{N_\alpha} + \frac{1}{N_d}} \tag{5.9}$$

The error bars in figure 5.9 indicate the statistical uncertainties in the cross-section measurements as calculated above. These statistical uncertainties are less than 2% (figure 5.9 and table 5.1) at all incident neutron energies. Systematic uncertainties arising from the separation of peaks corresponding to alphas from ^{12}C(n,α)^{9}Be$_{gs}$ and ^{12}C(n,n')3α reactions at incident neutron energies below 30 MeV and above 50 MeV are larger than at 30 to 50 MeV due to the overlap of the different alpha production channels at these energies as explained in chapter 4. This uncertainty is estimated to be about 2%. Systematic uncertainty arising from n-d forward recoil elastic cross-section data used in the calculations is estimated to be about 5% [Pa73].

Another source of uncertainty is the efficiency of pulse shape discrimination to separate the different charged particles, especially at the low pulse height region where there is an overlap in the loci corresponding to the different charged particles (see figure 3.3).

Cross-section measurements for production of alpha particles from ^{12}C(n,α)^{9}Be$_{gs}$ and ^{12}C(n,n')3α reactions were made for incident neutron energies ranging from 25 to 52 MeV. The statistical uncertainties in the measurements are less than 2% and the systematic uncertaities from the reference standard used are estimated to be 5%. In the next chapter cross-section measurements from this work are compared with measurements from other experiments and calculations in the literature.

Chapter 6

Discussion and Conclusions

The cross-sections for the production of alpha particles from the interaction of carbon-12 with neutrons in the energy range 25 to 52 MeV were measured (chapter 5) at twenty nine incident neutron energies. The cross-section measurements were made for the production of alpha particles from $^{12}C(n,\alpha)^{9}Be_{gs}$ and $^{12}C(n,n')3\alpha$ reactions. These measuremets provide a significant increase in data at this energy range, where there is a shortage of experimental measurements for these reactions. These cross-section measurements could be used as tests for the existence of alpha clusters in light nuclei. The L-S spectra for singles and coincidence events were analysed (chapter 4) at different neutron energies using scatter plots to resolve the structure in the loci. The analyses of the L-S spectra gave information about the energy distribution of alpha particles released from the $^{12}C(n,n')3\alpha$ reaction, which in turn gave information about the mechanism for decay of the ^{12}C nucleus into three alphas.

6.1 Comparison of Results

The alpha production cross-section measured in this work were compared with the measurements from the other authors. Comparisons were made with the nuclear emulsion measurements of Frye [Fr55], the measurements of Davis [Da63], Al-Kital [Al63] and Kitazawa [Ki69]. Comparisons were also made with the nuclear emulsion measurements of Antolkovic [An83] which have been reanalysed by Brenner *et al* [Br84] using the intranuclear cascade model with Fermi breakup. The calculations from the Monte Carlo fit of Del Guerra [De76] on the measurements of Frye [Fr55], Davis [Da63], Al-Kital [63], Kitazawa [Ki69] and Kellogg [Ke53] were also used for comparison.

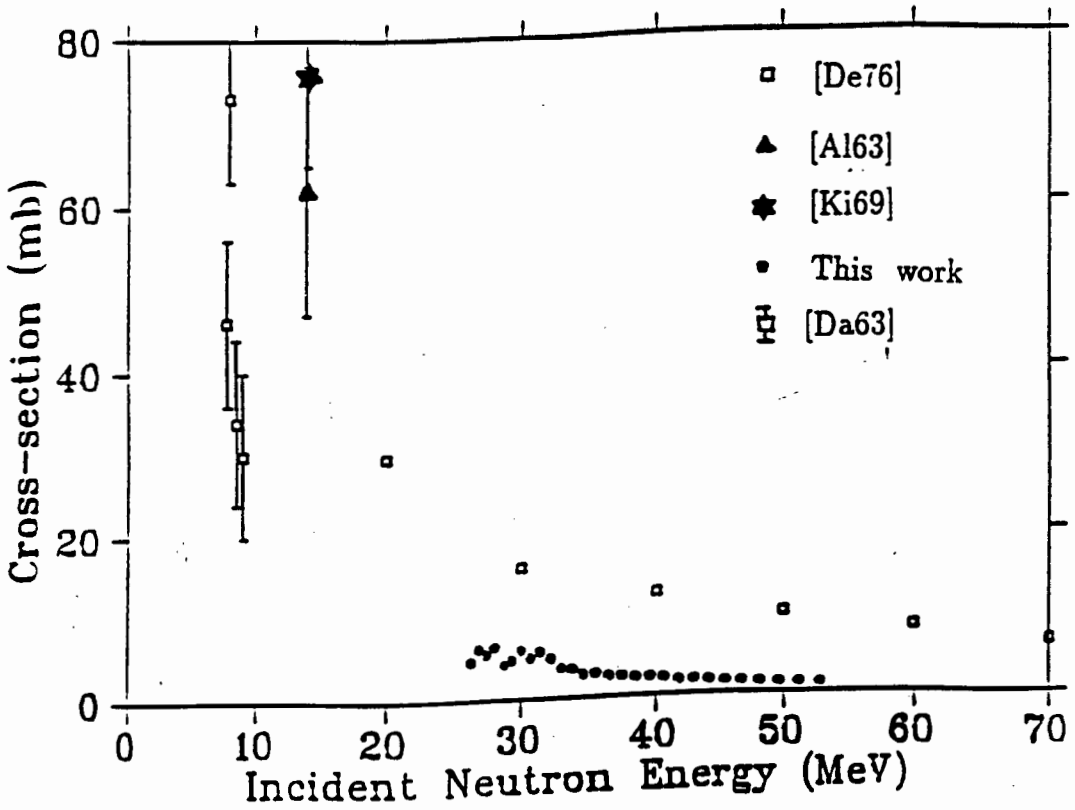

Figure 6.1: *Cross-section measurements for the production of alpha particles from the* $^{12}C(n,\alpha)^{9}Be_{gs}$ *reaction as a function of incident neutron energy. The error bars in the measurements are not visible in the plot because of the scale used. There is a scale uncertainty of about 5% from systematic uncertainties in the reference standard used in the cross-section measurements. Shown also are the results and calculations from other authors*

6.1.1 Cross-section for the $^{12}C(n,\alpha)^{9}Be_{gs}$ reaction

Figure 6.1 shows the cross-section data obtained in this work for the $^{12}C(n,\alpha)^{9}Be_{gs}$ reaction together with measurements and calculations from other authors. The error bars in the measurements are statistical uncertainties, these uncertainties are less than 2% and are not visible in the plot. Shown in figure 6.1 are measurements of Davis [Da63] (open squares with error bars), Al-Kital [Al63] (triangles), Kitazawa [Ki69] (stars) and the data from the Monte Carlo fit of Del Guerra [De76] (open squares without error bars). The previous experimental measurements are limited to the incident neutron energies below 20 MeV. The cross-sections measured in this work are systematically lower than the Monte Carlo calculation of Del Guerra [De76] by a factor ranging from $\sim$ 3 at E_n =30 MeV to $\sim$ 5 at E_n = 50 MeV.

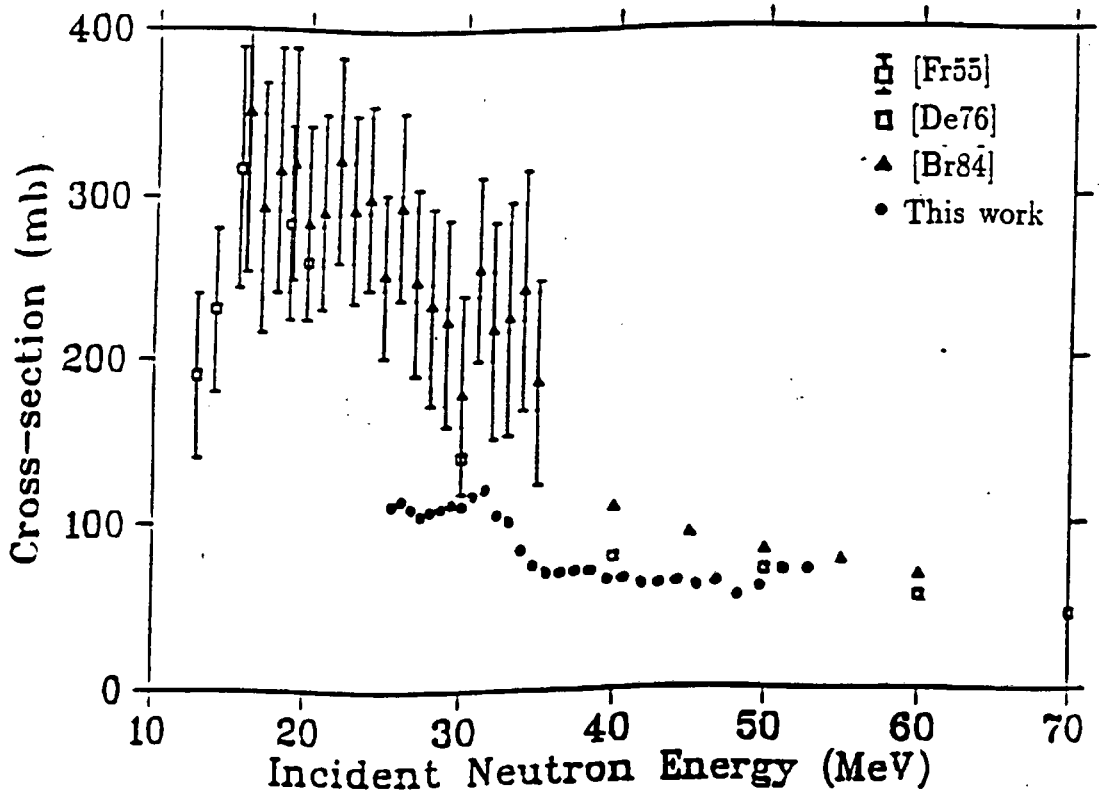

Figure 6.2: *Cross-section measurements for the production of alpha particles from the* ^{12}C(n,n')3α *reaction as a function of incident neutron energy. The error bars in the measurements are not visible in the plot because of the scale used. There is a scale uncertainty of about* 5% *from systematic uncertainties in the reference standard used in the cross-section measurements. Shown also are results and calculations from other authors.*

6.1.2 Cross-sections for the ^{12}C(n,n')3α reaction

Figure 6.2 shows the cross-section data for the ^{12}C(n,n')3α reaction together with measurements and calculations from other authors. The error bars in the measurements are statistical uncertainties, these uncertainties are less than 2% and are not visible in the plot. The comparison is made with the nuclear emulsion measurements of Frye [Fr55] (open squares with error bars), the nuclear emulsion measurements of Antolkovic [An83] which have been reanalysed by Brenner [Br84] using the intranuclear cascade model with Fermi breakup (triangles with error bars) and the calculations by Brenner (triangles without error bars) using the same model. The comparison is also done with the extrapolated measurements from the Monte Carlo fit of Del Guerra [De76] on the nuclear emulsion measurements of Kellogg [Ke53] and Frye [Fr55] (open squares without error bars).

The cross-section measurements for the production of alpha particles from the ^{12}C(n,n')3α reaction are systematically lower than the measurements from other

authors. Taking into consideration the scale uncertainty of 5% in the cross-section measurements from this work, measurements from this work and extrapolated values from Monte Carlo fit of Del Guerra [De76] are within 10% of each other. The results from this work are lower than the results by Antolkovic [An83] which have been reanalysed by Brenner [Br84]. At incident neutron energies below 30 MeV the measured cross-sections are lower than the published results by 50%. There is a small rise in the cross-section measurements above 50 MeV which could be attributed to the decrease in the efficiency of stripping of the n-d forward recoil peak at these energies, which is caused by the overlap from the $^{12}C(n,d)^{11}B_{gs}$ reaction peak.

6.2 Conclusions

The cross-sections for the production of alpha particles from the $^{12}C(n,\alpha)^{9}Be_{gs}$ and $^{12}C(n,n')3\alpha$ reactions were succesfully measured. The statistical uncertainty in the measurements is about 2%, and the systematic uncertainties contribute more than 5% to the uncertainties in the cross-section measurements. Cross-section for production of alpha particles from the $^{12}C(n,\alpha)^{9}Be_{gs}$ reaction are lower than the Monte Carlo fit of Del Guerra [De76] by a factor ranging from 3 to 5 in the energy range 30 to 50 MeV. Cross-section measurements for the production of alpha particles from the $^{12}C(n,n')3\alpha$ reaction are within 10% of the Monte Carlo fit of Del Guerra [De76]. These results show that a larger fraction of alpha particles is released through the $^{12}C(n,n')3\alpha$ reaction and only a small fraction is released through the $^{12}C(n,\alpha)^{9}Be_{gs}$ reaction.

The alpha particle spectra for the singles events (figure 3.11) and the L-S spectra (figures 4.2 and 4.3), measured with the NE230 scintillator in this experiment, strongly indicate that there is a change in the energy distribution of alpha particles released from the $^{12}C(n,n')3\alpha$ reaction. One alpha particle is released first followed by the emission of two alpha particles. As the incident neutron energy increases the first alpha particles is released with an increasingly larger fraction of the available energy and the remaining energy which is shared by the other two alpha particles decreases as the incident neutron energy increases. These results indicate that the ^{12}C breakup into three alpha particles is either via the $^{12}C(n,\alpha)^{9}Be^{*}(n',^{8}Be^{*}(2\alpha))$ pathway or the $^{12}C(n,n')^{12}C^{*}(\alpha,^{8}Be(2\alpha))$ pathway, or both in different proportions.

The separation of the alpha locus in the L-S plots (figures 4.2 and 4.3) shows that

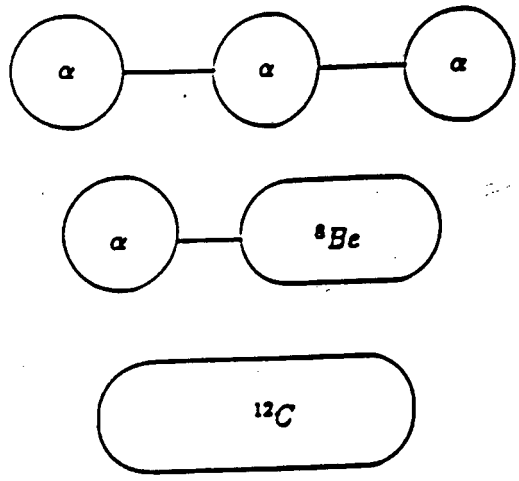

Figure 6.3: *The cluster model for the carbon-12 nucleus.*

pulse shape discrimination can be used to separate the two alpha producing reactions. The three alpha particles from the ^{12}C(n,n')3α reaction have a larger pulse shape (S) value than a single alpha particle from the ^{12}C(n,α)^{9}Be$_{gs}$ reaction. The alpha particles from the ^{12}C(n,n')3α reaction thus lie on the high pulse shape (S) region of the alpha locus and the alpha particles from the ^{12}C(n,α)^{9}Be$_{gs}$ reaction lie on the lower pulse shape region of the alpha locus.

The cross-section for production of alpha particles is greater than the cross-sections for the (n,p) and (n,d) reactions when a ^{12}C nucleus interacts with neutrons of energy 10 to 25 MeV (see figure 1.3). This can be explained by regarding the carbon-12 nucleus as a cluster of alpha particles (figures 1.4 and 6.3). In the interaction of carbon-12 with neutrons, the ^{12}C nucleus is excited to higher energies above the minimum energies for formation of different clusters, leading to the decay of ^{12}C nucleus into respective clusters. At low incident neutron energies the ^{12}C nucleus can be raised to excited states above the minimum energy for $\alpha-^{8}$Be cluster formation (figure 6.3). Above this energy the ^{12}C nucleus decays by emission of a single alpha particle and ^{8}Be nucleus. As the incident neutron energy increases the ^{12}C reaches the minimum energy for formation of alpha particle clusters (figure 6.3). Above this energy the ^{12}C nucleus decays by the emission of three alpha particles.

6.3 Further Work

The data obtained from the coincidence experiment can also be used to calculate the alpha production cross-section from the ^{12}C(n,n')3α reaction relative to the n-d elastic scattering at $\theta_{lab} = 90^0$. This can be done in the same way as it was done in this work, by using the integrals of the projected pulse height spectra for the alphas (N_α) and deuteron (N_d) which are in coincidence with the scattered neutrons. This should give a better measurement of the alpha production cross-section from the ^{12}C(n,n')3α reaction, since this method will decrease the uncertainty in the stripping of the peaks from the two reactions. The cross-section for the production of alpha particles from the ^{12}C(n,α)^{9}Be$_{gs}$ reaction will then be obtained by subtracting the alpha production cross-section from the ^{12}C(n,n')3α reaction from the total alpha production cross-section. This will, however, result in the increase of the statistical and systematic uncertainties in the cross-section measurements for the ^{12}C(n,α)^{9}Be$_{gs}$ reaction.

The scattered neutron time of flight spectrum from the coincidence experiment, if measured with sufficient resolution, could be used to select the neutrons scattered from the different energy levels in the ^{12}C nucleus, by setting cuts on peaks corresponding to the different excited states in carbon (figure 6.4). The coincidence experiment data with cuts on the scattered neutron time of flight spectrum can then be used to calculate partial alpha production cross-section from different excited states in carbon. This will however require a long flight path (figure 6.4) to get a better resolution in the time of flight spectrum. This could not be done in this work because of the very short flight path used (0.474 m).

The separation of the events from the ^{12}C(n,α)^{9}Be$_{gs}$ and ^{12}C(n,n')3α reactions in the alpha particles locus of the L-S plots could be used to separate the two alpha producing reactions. This could be done by setting up software cuts in the L-S plot to select events corresponding to a particular alpha producing reaction and projecting it on the L axis to obtain a pulse height spectrum. The integrals of the peaks in the projected pulse height spectra would then be used to calculate the alpha production cross-sections. This method was not used in this work because of the insufficient resolution in the L-S spectra for the separation of the events from the two alpha producing reactions.

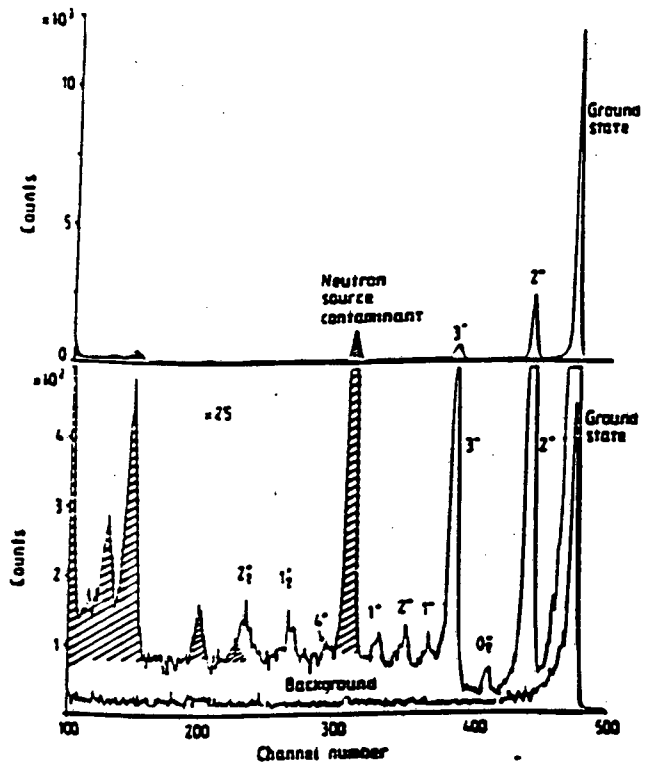

Figure 6.4: *The neutron time of flight spectrum for neutrons scattered from* ^{12}C *and* ^{12}C(n,n')^{12}C *at* $E_n = 24$ MeV, $\theta_{lab} = 44°$, *flight path = 15 m [Me84].*

Appendix A

Pulse Shape Discrimination

The light output from most organic scintillators is made up of two components (figure A.1): the fast component (with a pulse decay time of a few nanoseconds) and the slow component (with a pulse decay time of several hundred nanoseconds). The fast component is characterized by the decay of the excited states of the molecules in the scintillator by the prompt fluorescence from the singlet states and the slow component by the delayed fluorescence. The delayed fluorescence is caused by the excitation of the long-lived triplet states in the molecules of the scintillator [Kn89] which occurs through a transition called intersystem crossing (figure A.2). In this transition the excited singlet state is converted into the triplet state. This state can decay through normal phosphorescence; some molecules may be excited back to the singlet state and subsequently decay through normal flourescence. This delayed flourescence of the singlet state contributes to the slow component.

The excitation of the states in the molecules of the scintillator depends on the rate of the energy loss, dE/dx, of the ionizing particle. It has been observed that particles with a large rate of energy loss, dE/dx, have a larger slow component. This means that the fraction of light contributing to the slow component often depends on the nature of the ionizing particle. This is the basis of the pulse shape discrimination technique. Figure A.3 from Lynch [Ly75] illustrates the different decay times and hence different pulse shapes, exhibited by a stilbene crystal and a NE213 liquid scintillator.

In pulse shape discrimination systems, a pulse shape parameter, S, which depends on the ratio of the fast and slow component of the scintillation light output is generated. The pulse shape parameter is generated from the L and F signals from the LINK module (see chapter 2). The L signal is generated by integrating the scintilating pulse from the LINK for about 500ns. The fast component (F) of the

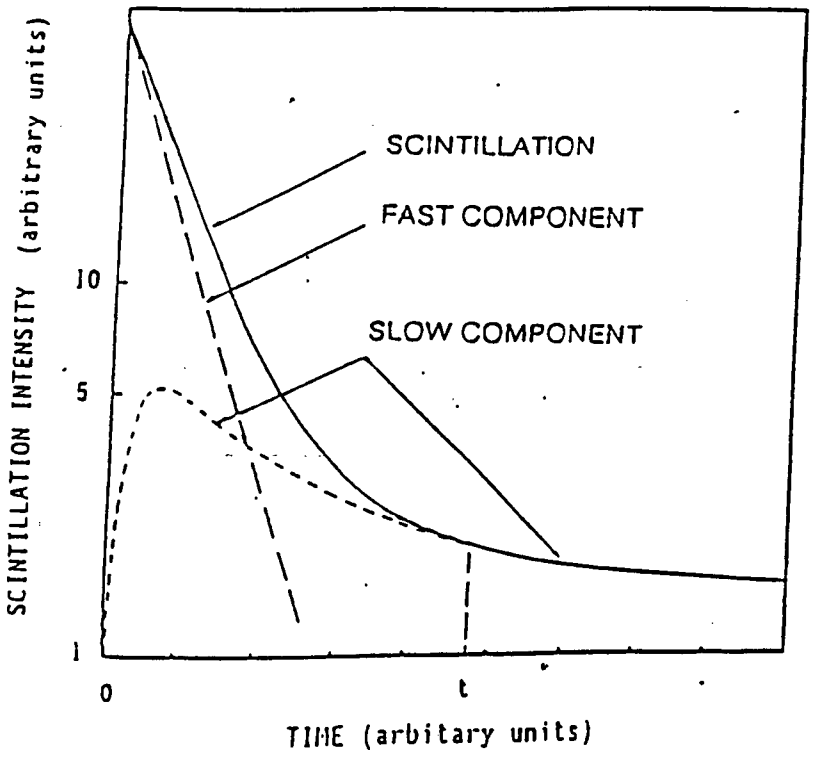

Figure A.1: *Schematic representation of the of the scintillation decay of the organic scintillator showing the total light output, the fast and the slow components. Reproduced from [Vo68].*

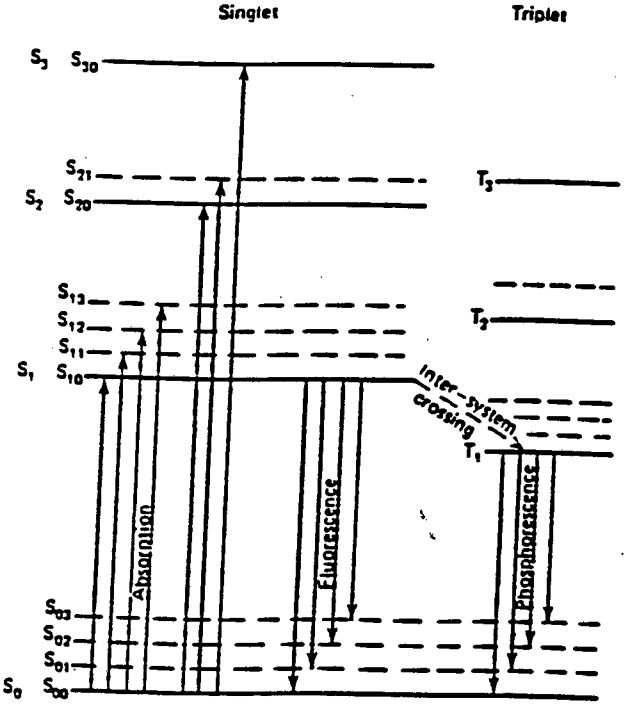

Figure A.2: *Energy levels of an organic scintillator with π-electron structure [Bi64].*

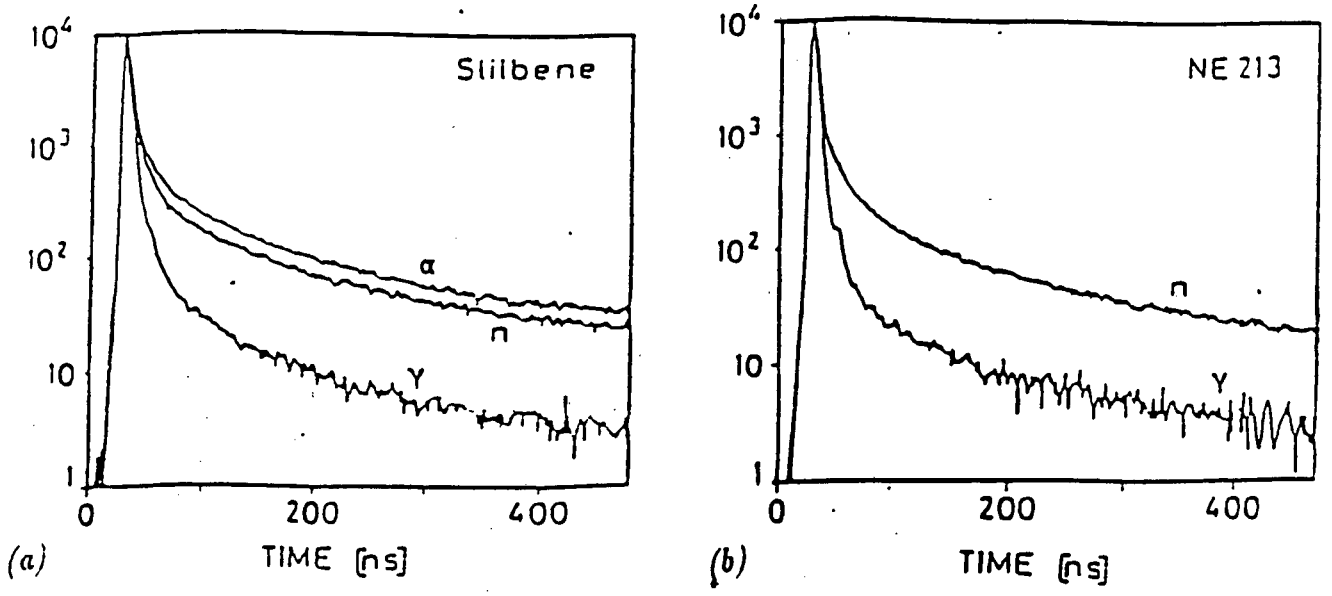

Figure A.3: *(a) Pulse shape of stilbene light for alpha particles, neutrons and gamma rays. (b) Pulse shape of NE213 liquid scintillator for neutrons and gamma rays.*

scintillation pulse is the integral over the prompt component of the scintillation pulse which is about 20ns [Br79]. There are several methods of generating the pulse shape parameter, see for example [Br79], one of which is to use the following relationship:

$$S = L - kF + C \tag{A.1}$$

where:
L : Sum of fast and slow components
F : fast component of the scintillation pulse
k, C : arbitrary constants

A plot of pulse height (L) versus pulse shape (S) for events measured by the scintillator make discrete loci on the plane corresponding to the different charged particles which are detected by the scintillator. Shown in figure A.4 is a perspective plot of counts as a function of pulse height and pulse shape for events measured by a NE213 liquid scintillator when exposed to 63 MeV neutrons. The ridges in the figure correspond to protons, deuterons, tritons, ^{3}He nuclei, alphas and escaping protons i.e protons which do not come to rest in the scintillator. The constants k and C are chosen and introduced into the software to suit the data. The value of k determines the angle of the loci in the L-S spectra and the value of C determines the position of these loci along the S-axis. Figure A.5

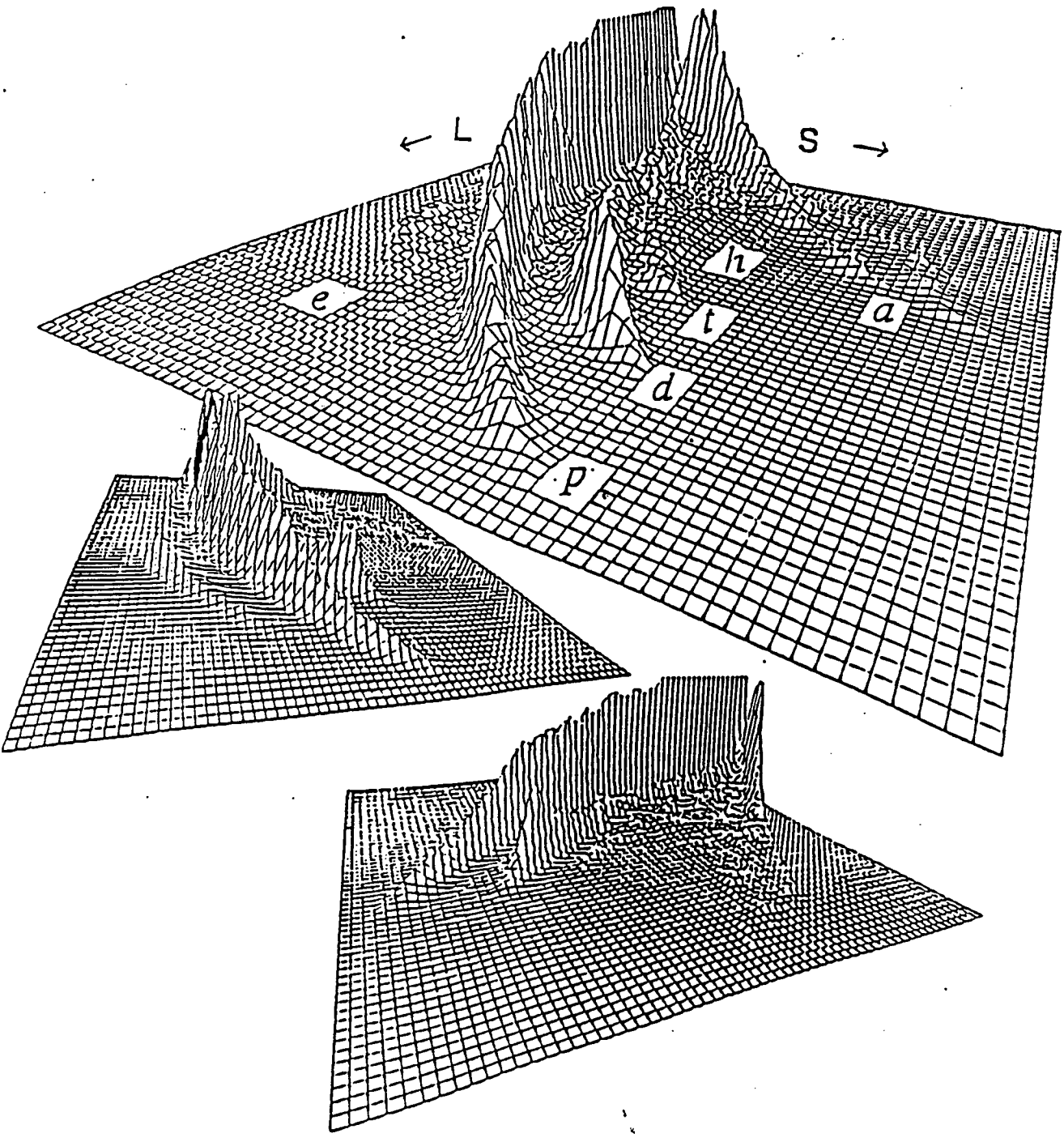

Figure A.4: *Perspective views of counts (vertical) as a function of pulse height (L) and pulse shape (S) for events in an NE213 scintillator. The ridges in the figure correspond to (p) protons, (d) deuterons, (t) tritons, (h)* ^{3}He *nuclei, (a) alphas and (e) escaping protons i.e protons which do not come to rest in the scintillator.*

shows the L-S scatter plots for events measured by a NE230 liquid scintillator when exposed to neutrons of energy E_n = 40 MeV. The ridges correspond to alphas, protons, deuterons and escaping protons. The plot shows the rotation of the loci and the shift in the positions of the loci as the values of k and C are changed.

Pulse shape discrimination was used in this work to identify and separate the different charged particles and the reaction products. The scatter plots were used to investigate the feasibility of distinguishing different alpha production modes such as ^{12}C(n,α)^{9}Be and ^{12}C(n,n')3α in the L-S plane.

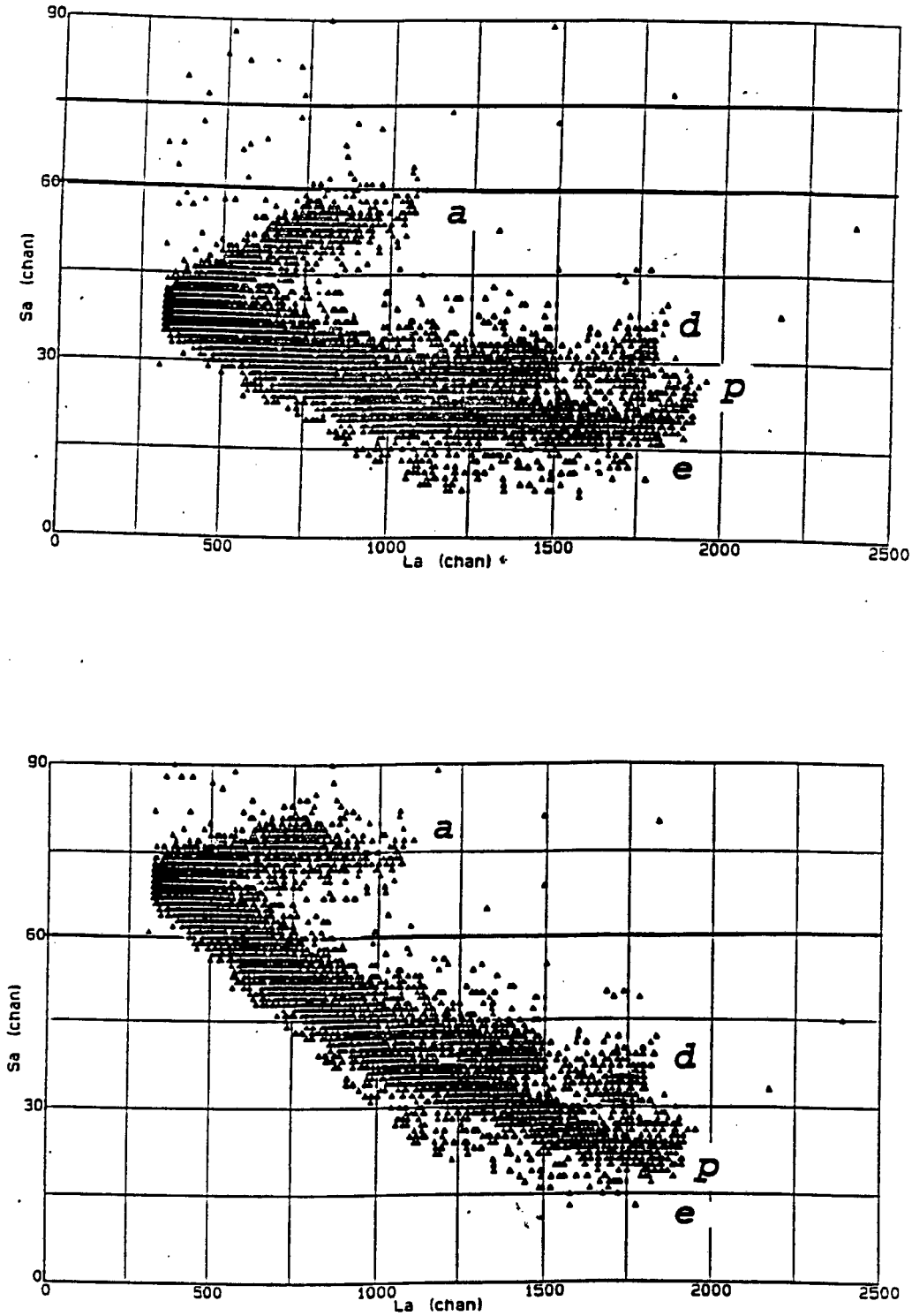

Figure A.5: *Scatter plots of pulse height (L) and pulse shape (S) for different values of k and C. The loci associated with different particles are (p) protons, (d) deuterons, (a) alphas and (e) escaping protons.*

Appendix B

The non-relativistic expressions for the energetics for nuclear reactions

(Reproduced from Marion and Young [Ma68])

ψ, ζ in laboratory frame
θ, ϕ in centre-of-mass frame

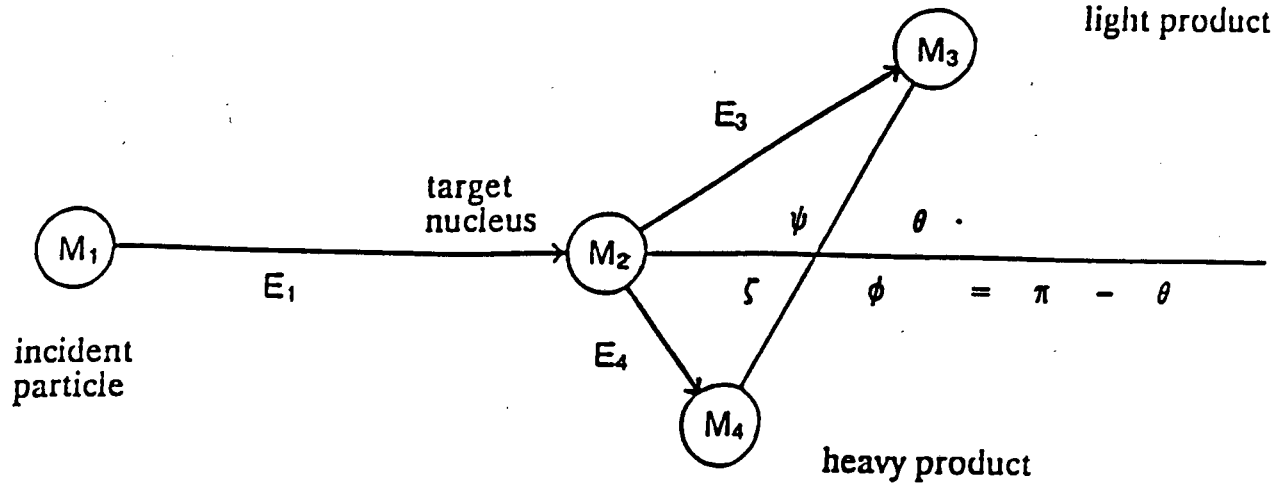

$$Q = M_1 + M_2 - M_3 - M_4$$

$$E_T = E_1 + Q = E_3 + E_4$$

Define:

$$A = \frac{M_1 M_4 (E_1 / E_T)}{(M_1 + M_2)(M_3 + M_4)}$$

$$B = \frac{M_1 M_3 (E_1 / E_T)}{(M_1 + M_2)(M_3 + M_4)}$$

$$C = \frac{M_2 M_3}{(M_1 + M_2)(M_3 + M_4)} \left(1 + \frac{M_1 Q}{M_2 E_T}\right)$$

$$D = \frac{M_2 M_4}{(M_1 + M_2)(M_3 + M_4)} \left(1 + \frac{M_1 Q}{M_2 E_T}\right)$$

$$A + B + C + D = 1$$

Then the laboratory energy of the light product, E_T, is given by:

$$E_3 = E_T \{ B + D + 2(AC)^{1/2} \cos\theta \}$$

$$= E_T \{ B [\cos\psi + (D/B - \sin^2\psi)^{1/2}]^2 \}$$

Appendix C

Detector Calibrations

The schematic diagram of the experimental geometry for the measurement of the cross-section from the interaction neutrons with carbon-12 is shown in figure 2.1. The NE230 and NE213 scintillators were calibrated to measure the energy of the incident and scattered neutrons respectively, using the time-of-flight technique. The response (pulse height) of the detectors were calibrated as a function of energy deposited by charged particles using gamma ray sources of known energies.

C.1 Time (Energy) Calibrations

The time-of-flight channel scales in the incident and scattered neutrons time-of-flight spectra (figures 3.4 and 3.5) could be calibrated to nanosecond scales by operating the TACs in the self-stopped mode with two different delays respectively between the start and stop pulses, and observing the change in the position of the gamma peak. This method was used for the calibration of the NE213 detector. The method was not considered to be accurate enough for the calibration of the time-of-flight for incident neutrons. The NE230 detector was calibrated using the method described in section C.1.1.

C.1.1 Calibration for the NE230 Detector

The time-of-flight spectrum for incident neutrons measured by a NE230 scintillator is shown in figure 3.4. The time-of-flight channel scale of the spectrum measured by a NE230 scintillator was calibrated to a nanosecond scale by using positions and times of flight of gamma peak and of the most energetic neutrons in time-of-flight spectrum. This method was used instead of the standard method of using delay cables and TAC described above, because it was considered to be more accurate. The time-of-flight spectrum measured by a NE230 detector has

a sharp neutron edge (t_{nm} in figure 3.4) which corresponds to maximum neutron energy (63 MeV) detected. These neutrons are released from ground state transition of ^{9}Be(p,n)^{9}B reaction. The energy of these neutrons was determined by non-relativistic kinematics equations (appendix B). Their time-of-flight was determined by using non-relativistic time-of-flight equation (C.2) and was found to be 52.6 ns. Using differences in positions of neutron edge (t_{nm}) and gamma peak, and differences in their calculated times of flight the time calibration was found to be 0.111 nanosecond/channel. The neutron time of flight T_n was then given by the relationship:

$$T_n = k\,(T_e - n) + 52.6\ ns \tag{C.1}$$

where:
- n : ADC channel number
- T_e : position of the neutron edge (ADC channel number)
- k : 0.111 nanosecond/channel

The neutron energy E_n (in MeV) corresponding to time-of-flight T_n, was calculated using non-relativistic time-of-flight equation:

$$E_n = \left\{\frac{72.3\ d}{T_n}\right\}^2 \tag{C.2}$$

where:
- T_n : as in equation C.1 (in ns)
- d : flight path of the neutrons (in m)

The uncertainty ΔE_n (FWHM) in neutron energy measurement depends on the timing resolution, ΔT_γ (FWHM) of the system, and the uncertainty in flight path Δd (FWHM). FWHM ΔT_γ of the gamma peak was used as an estimate of the timing uncertainty obtainable for neutrons selected by time-of-flight.

In the limit $\Delta T_\gamma / T_n \gg \Delta d/d$, the energy uncertainty is given by:

$$\Delta E_n = 0.028\ \frac{\Delta T_\gamma}{d}\ {E_n}^{3/2} \tag{C.3}$$

where:
- ΔT_γ : FWHM of the gamma peak
- d : as for equation C.1 above
- E_n : neutron energy in MeV

Figure C.1 shows ΔE_n as a function of E_n for incident neutron energies considered in this work, calculated using equation C.3.

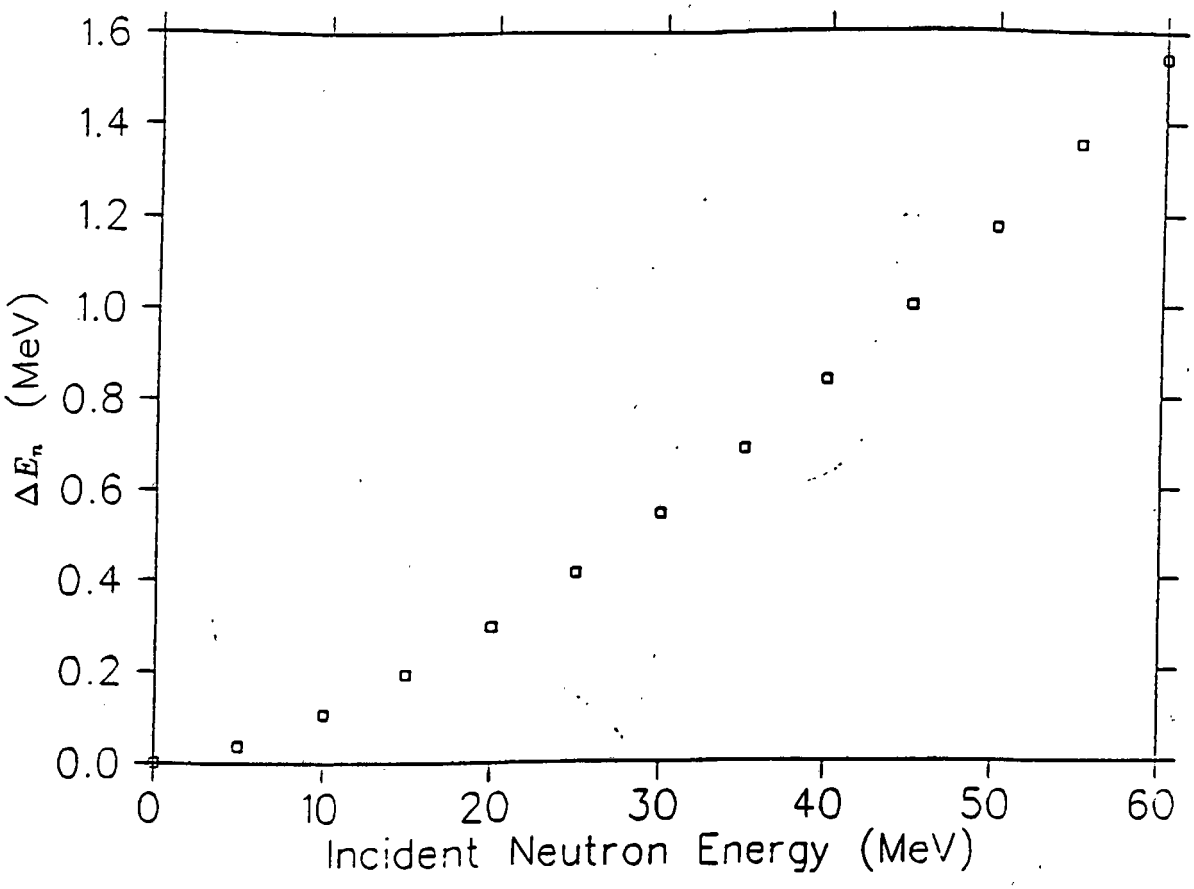

Figure C.1: *The energy resolution, ΔE_n, as a function of E_n for the incident neutron energies considered in this work.*

C.1.2 Calibration for the NE213 Detector

The scattered neutron time-of-flight spectrum measured by the NE213 scintillator, with a flight path of 0.474 m, is shown in figure 3.4. The time-of-flight channel scale was calibrated to a nanosecond scale by changing time delay of stop signal going into the TAC, and observing the change in position of neutron edge in time-of-flight spectrum. The channel scale was thus calibrated to nanosecond scale and the linearity of TAC was also verified. A time calibration of 0.11 nanoseconds/channel was calculated for this detector. The scattered neutron energy E_c corresponding to time-of-flight T_c, was calculated by using the time-of-flight equation (C.2).

The uncertainty in scattered neutron energy measurement, ΔE_c, was found in a similar way as for incident neutrons.

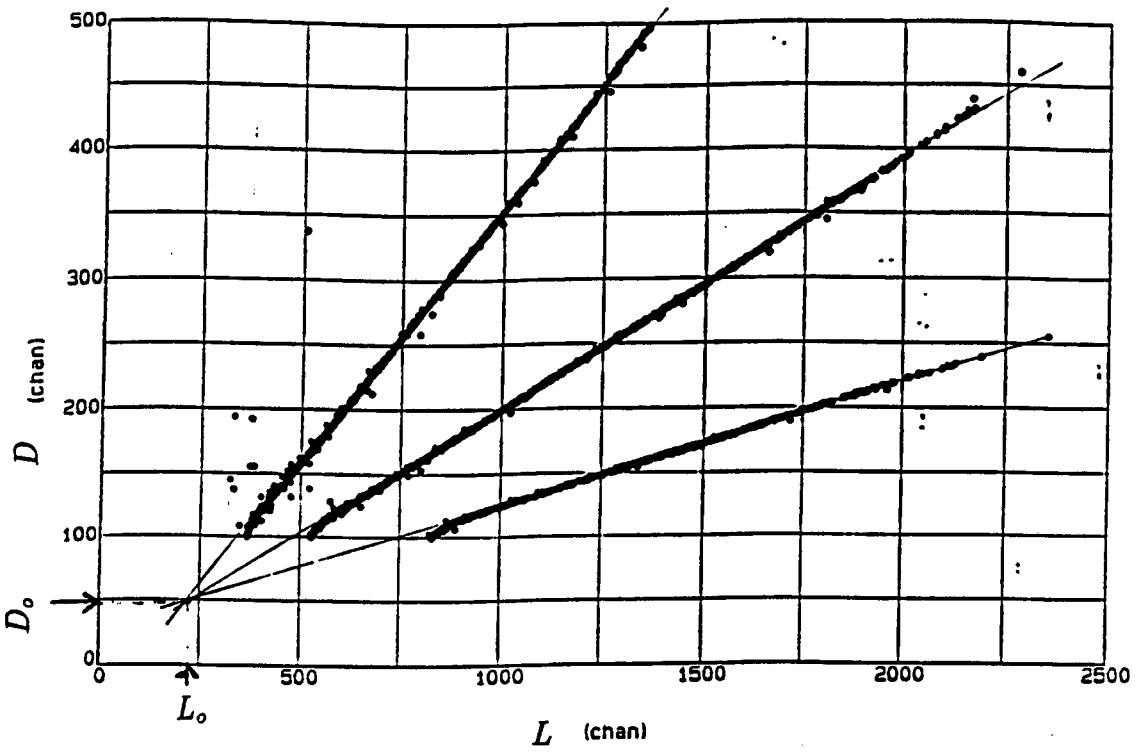

Figure C.2: *Event scatter plot of pulse height, L, as a function of the dynode signal, D, recorded with the NE230 scintillator to determine the true zero, L_o.*

C.2 Pulse Height Calibrations

Outputs from LINK modules were corrected for zero offset. The electronic configuration (figure 2.6) of the experiment was altered slightly for zero calibration runs. Preamplifiers were connected to LINK inputs to generate dynode signals (D). D and L are related by the following equation:

$$D - D_o = K\,(L - L_o) \tag{C.4}$$

where D_o and L_o are true zeroes and K is the gain in preamplifier. Changing K in preamplifier results in lines pivoting about true zeroes in the plots of D versus L (see figure C.2). Figure C.2 shows scatter plot of L as a function of D used in zero calibration of a NE230 scintillator. The zero calibration for NE213 scintillator was done in a similar way as for the NE230 scintillator.

The light output and therefore pulse height produced in organic scintillators by heavily ionizing particles is not a linear function of energy lost by charged particle [Ma78], thus it is necessary to calibrate the response of a scintillator as a function of energy deposited by the particles. Since the light output produced from an organic scintillator is known to be a linear function of energy deposited by an electron of energy above 100 keV, it is customary to state the response of

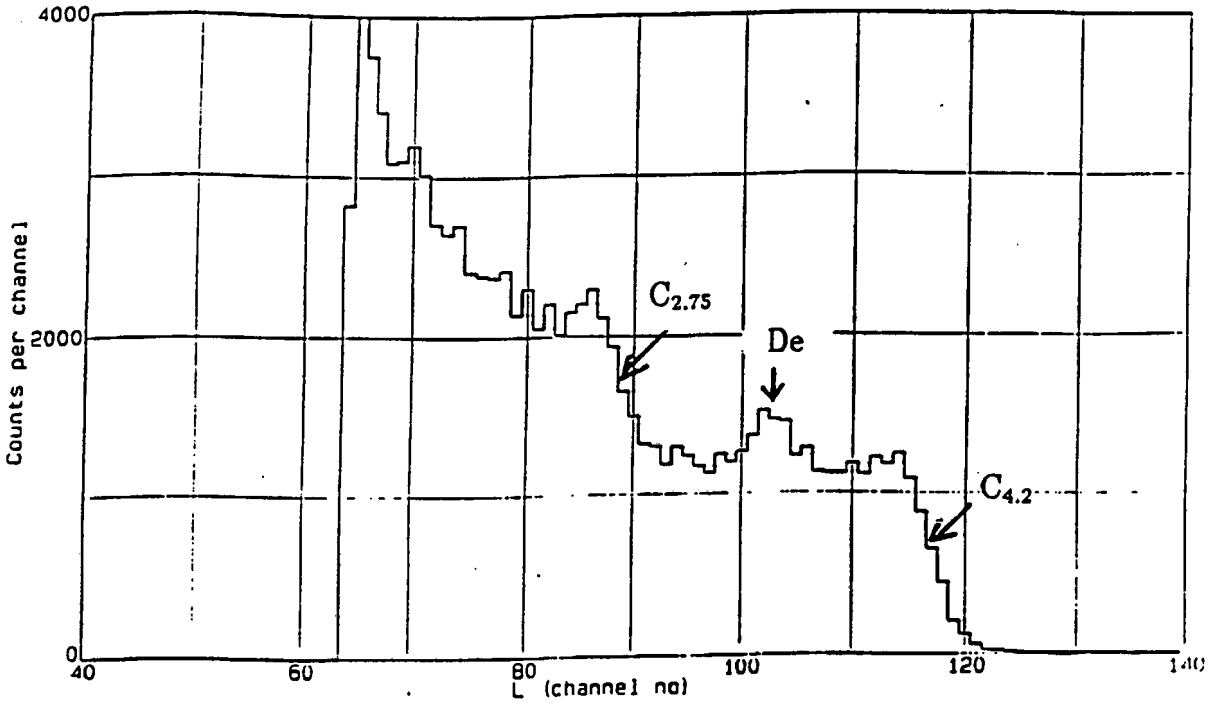

Figure C.3: *Pulse height spectrum recorded with the NE230 scintillator for the gamma rays from the AmBe and* ^{24}Na source.

a scintillator to a charged particle in terms of an equivalent electron energy, in units of MeVee (MeV electron equivalent). This is the electron energy that produces same light output or pulse height as charged particles. A few calibration measurements made using gamma sources of known energy suffice to calibrate the pulse height in this way. In this work, we calibrated the NE230 scintillator by recording the pulse height for the 4.44 MeV γ-rays from the AmBe source and the 2.75 MeV γ-rays from ^{24}Na under the same experimental conditions. The NE213 scintillator was calibrated in the same way, but only using the 4.44 MeV γ-rays from the AmBe source.

Figure C.3 shows a pulse height spectrum recorded, for gamma rays only from the AmBe source by the NE230 deuterated liquid scintillator, in a capsule of 50 mm length and 42 mm diameter. Features in the spectrum are (i) the 4.2 MeV compton edge ($C_{4.2}$) corresponding to the 4.44 MeV γ-rays from a AmBe source, (ii) the 3.42 MeV double escape peak (De), which arises from pair production interaction of 4.44 MeV on the carbon component of NE230 scintillator and (iii) the 2.75 MeV compton edge ($C_{2.75}$) from gamma rays from ^{24}Na which is produced by an interaction of incident neutrons with the aluminium housing of the scintillator through ^{27}Al(n,α)^{24}Na reaction. The energy of the compton edge,

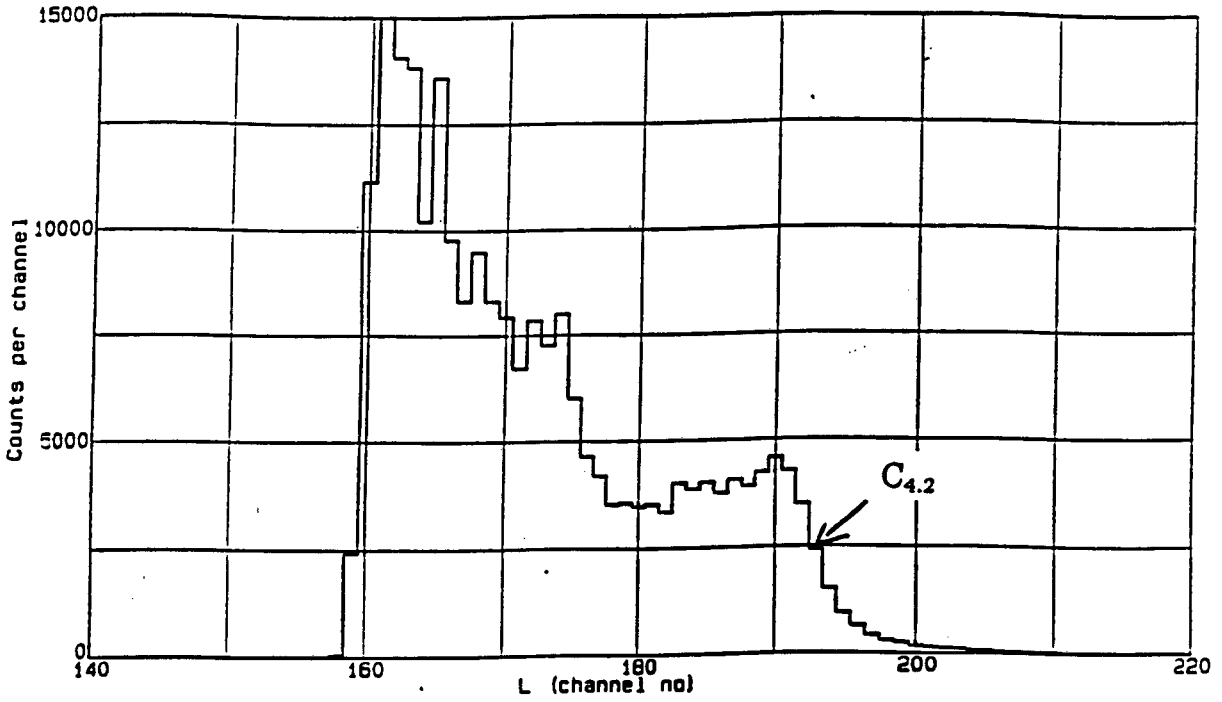

Figure C.4: *Pulse height spectrum recorded with the NE213 scintillator for the gamma rays from the AmBe source.*

E_c, was calculated using:

$$E_c(MeV) = \frac{2\,E_\gamma{}^2}{2\,E_\gamma\,+\,m_e c^2} \qquad \text{(C.5)}$$

where $m_e c^2 = 0.511$ MeV is the electron rest mass energy. This gives $E_c = 4.20$ MeV for the 4.44 MeV γ-rays of the AmBe source.

For the NE213 scintillator we can only identify the compton edge associated with the 4.44 MeV γ-rays of the AmBe, which is sufficient for our purpose see figure C.4. The three measurements; two compton edges and double escape peak in a NE230 scintillator are plotted in figure C.5. The data are consistent with the expected linear relation between scintillation light output and electron energy, thus pulse height scale can be calibrated in units of MeVee. Figure C.6 shows pulse height (in units of MeVee) as a function of charged particle energy for events measured by a NE230 scintillator. The deuteron and alpha particles response data deviate from the expected linear dependence [Br79] at higher pulse heights. This effect is caused by space charge saturation in the photomultiplier.

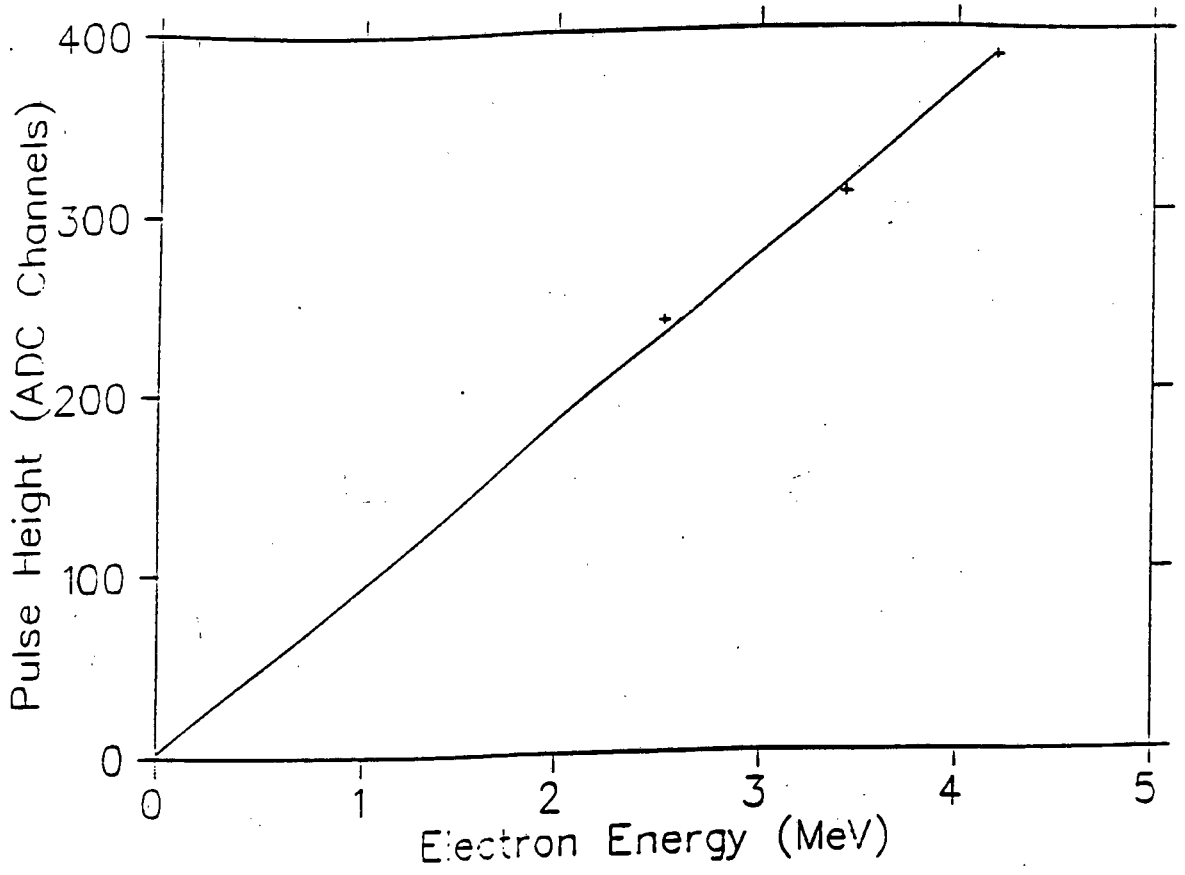

Figure C.5: *Calibration of pulse height channel to electron energy for the NE230 scintillator.*

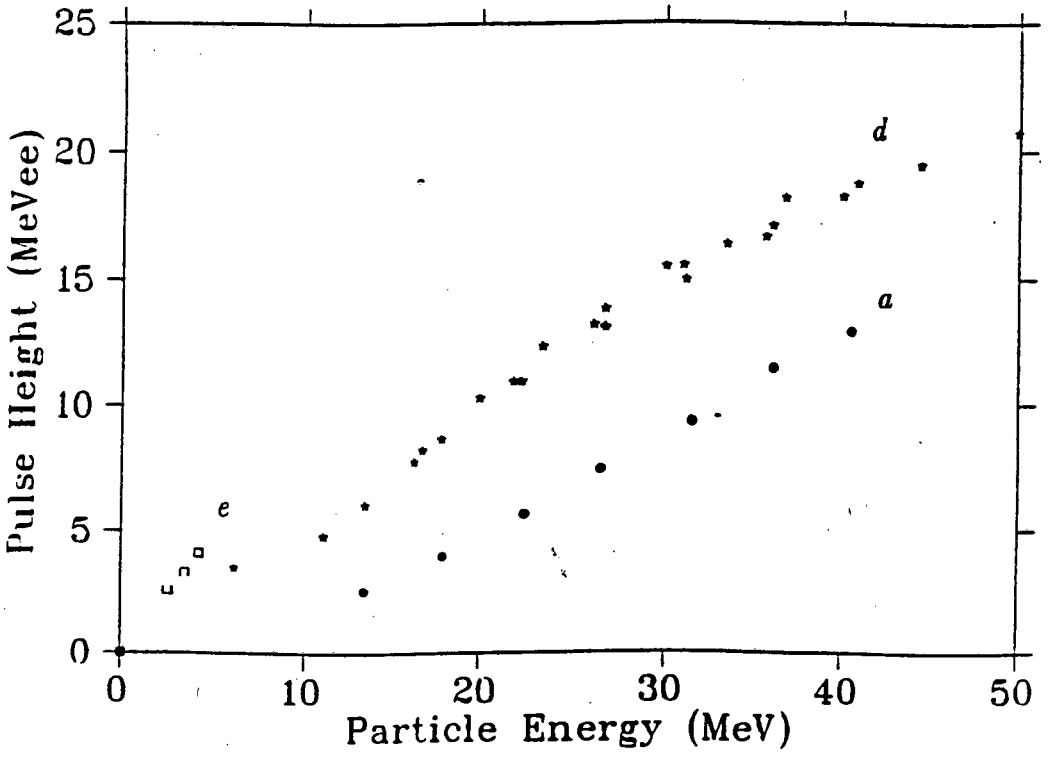

Figure C.6: *Measurements of the response (pulse height) of a NE230 detector as a function of charged particle energy for electrons (e), deuterons (d) and alphas(a).*

Bibliography

[Al63] R.A. Al-Kital and R.A. Peck Jr *Phys.Rev. 130 (1963) 1500.*

[An75] B. Antolkovic and Z. Dolenec. *Nucl.Phys. A237 (1975) 235*

[An76] B. Antolkovic. *Fizika 8 (1976) 163*

[An83] B. Antolkovic, I. Slaus, D. Plenkovic, P. Macq and J.P. Meulders. *Nucl.Phys. A394 (1983) 87*

[An91] B. Antolkovic, H. Dietze and H. Klein. *Nucl.Sci.Eng. 107 (1991) 1*

[Ax87] E.J. Axton. *National Physics Laboratory, Teddington, U.K., Private Communication (1987).*

[Ba89] M. Baba, M. Ishikawa, J. Kikuchi, H. Wakabashayi and N. Hirakawa. *"Double Differential Neutron Scattering Cross-section of Beryllium, Carbon and Oxygen". Proc.Int.Conf. Nuclear data for Science and Technology, Mito, Japan May 30 - June 3, 1988; and Private Communications (1989).*

[Bi51] J.B. Birks *Proc.Phys.Soc. A64 (1951) 874.*

[Bi64] J.B. Birks *The Theory and Practice of Scintillation Counting. Copyright 1964 by Pergamon Press. Ltd.*

[Bo86] R. Bottger, H.J. Brede, H. Klein, H. Scholermann and B.R.L. Siebert. *"Elastic and Inelastic Scattering of Fast Neutrons on Carbon", Proc.Int.Conf. Nuclear data for Basic and Applied Science, Santa Fe, New Mexico, May 13-17, 1985, Vol.II. p1455, Gordan and Breach Science Publishers (1986).*

[Br70] D.M. Brink, H.Friedrich, A.Weisgung and C.W. Wong. *Phys.Lett. 33b (1970) 143*

[Br64] J.A. Brinkley, B.A. Robson and E.W Titterson. *Proc.Phys.Soc. 84 (1964) 201*

[Br79] F.D. Brooks *Nucl.Inst. and Meth 162 (1979) 477*

[Br84] D.J. Brenner and R.E. Prael. Nucl.Sci.Eng. 88 (1984) 97

[Br91] H.J. Brede, G. Dietze, H. klein and H. Scholermann. *Nucl.Sci. and Eng. 107 (1991) 22*

[Bu75] B. Buck, C.B. Dover and J.P. Vary. *Phys.Rev. C11 (1975) 1803.*

[Bu90] A. Buffler, MSc. Thesis, University of Cape Town (unpublished). 1990.

[Buc90] B. Buck, A.C. Merchant and S.M. Perez. *Phys.Rev.Lett. 65 (1990) 2975.*

[Bu94] B. Buck, A.C. Merchant and S.M. Perez. *Phys.Rev.Lett. 72 (1994) 1326.*

[DA63] E.A. Davis, T.W. Bonner, D.W. Worley Jr, and R. Bass. Bull *Am.Phys.Soc (1963) 115.*

[De76] A. Del Guerra. *Nucl.Inst. and Meth. 135 (1976) 337*

[ENDF/B-V] *"Evaluated Nuclear Data File, ENDF/B-V" Brookhaven National Laboratory (1979).*

[Ep69] M.B. Epstein, H.D Holmgren, M.Jaus, H.G. Pugh, R.G. Roos, N.S. Wall and C.D. Goodman. *Phys.Rev. 178 (1969) 1968*

[Fin85] R.W. Finlay,A.S. Meigooni, J.S. Petler and J.P. Delaroche. *Nucl.Inst. and Meth. B10/11 (1985) 396*

[Fr55] G.M. Frye, L. Rosen and L.Steward. *Phys.Rev. 99 (1955) 1375*

[Gl82] D.W. Glasgow, F.O. Purser, H. Hogue, J.C. Vlement, K. Stelzer, M. Mack, J.R. Boyce, D.H. Epperson, S.G. Glendinning, E.G. Bilpuch, H.W. Newson and C.R. Gould, *Triangle University National Laboratory, Private Communication (1982).*

[Gr49] L.L Green and W.M Gibson. *Proc.Phys.Soc. 62 (1949) 296*

[Ha84] R.C. Haight, S.M. Grimes, R.G. Johnson and H.H. Barschall. *Nucl.Sci. and Eng. 87(1984) 41*

[Ha86] L.F. Hansen. *"Recommended Set of Neutron Differential Cross-sections for Carbon at 14.1 MeV" UCRL-95890, Lawrence Livemore National Laboratory (1986).*

[Ho80] R.H. Howell, F.S. Dietrich and F. Petrovich *Phys.Rev. C21 (1980) 1158.*

[Hod88] P.E. Hodgson. *Proceedings of the fifth international Conference on "Clustering Aspects in Nuclear and Subnuclear Systems", Kyoto, Japan, July 25-29 (1988). Physical Society of Japan.*

[Hor88] H. Horiuchi. *Proceedings of the fifth international Conference on "Clustering Aspects in Nuclear and Subnuclear Systems", Kyoto, Japan, July 25-29 (1988). Physical Society of Japan.*

[Ik68] K. Ikeda, N.Takigawa and H. Horiuchi. *Prog.Theor.Phys.Suppl. Extra number (1963) 464.*

[Ik89] K. Ikeda *Proceedings of the fifth international Conference on "Clustering Aspects in Nuclear and Subnuclear Systems", Kyoto, Japan, July 25-29 (1988). Physical Society of Japan. J. Phy.Soc.Jpn 58 (1989) Suppl. 277-287.*

[Ja53] J.D. Jackson and D.I. Wanklyn. *Phys.Rev. 90 (1953) 381*

[Jo92] D.T.L. Jones, J.E. Symons, T.J. Fulcher, F.D. Brooks, M.R. Nchodu, M.S. Allie, A Buffler and M.J. Oliver. *J.Med.Phys. (1992).*

[Ke53] D.A. Kellogg. *Phys.Rev 90 (1953) 224*

[Ki69] H. Kitazawa and N. Yamamuro. *J. Phys.Soc.Jap. 26 (1969) 600.*

[Kn89] G.F. Knoll *Radiation Detection and Measurement, second edition, John Wiley and sons, 1989, USA.*

[La75] J. Lachkar, F. Coci, G. Haouat, P le Floch, Y. Patin and G. Sigaud. *'An Evaluation of the Neutron-Induced Scattering, Reaction and Photon-Production Cross-Section of Carbon' NEANDC (E) 168 "L" (1975).*

[Lu70] R.L. Ludin, B.A. Wooten, R. Goloskie and R.G. La Montague *Phys.Rev. C5 (1970) 1740.*

[Ly75] F.J. Lynch *IEEE Trans, Nucl.Sci. NS-22, 58 (1975).*

[Ma68] J.B. Marion and F.C Young *Nuclear Reaction Analysis (North Holland, Amsterdam. 1968)*

[Ma78] R. Madey, F.M. Waterman, A.R. Baldwin, J.N. Knudson,J.D. Carlson and J. Rapaport *Nucl.Inst. and Meth. 151(1978) 445*

[Mc75] M.W. McNaughton, N.S.P. King, F.P. Brady and J.L. Ullman *Nucl. Inst. and Meth. 129 (1975) 241.*

[Me67] Dn.F. Measday and J.N. Palmieri *Phys. Rev. 161 (1967) 4 161.*

[Me84] Ali. S. Meigooni, J.S. Petler and R.W. Finlay *Phy.Med.Bio. 29 (1984) 6 643.*

[Mo56] H. Morinaga. *Phys.Rev. 101 (1956) 254.*

[Nac87] *Annual Report of the National Accelerator Centre, Faure, South Africa (1987).*

[NE] Table of Physical Constants of Scintilators, available from NUCLEAR ENTERPRISES Technology Limited, Sighthill, Edinburgh, Scotland EH11 4BY.

[Ol89] N. Olson,B. Trostel and E. Ramstrom. *Phys.Med.Biol. 34 (1989) 909.*

[Pa73] G. Pauletta, Thesis, University of Cape Town (unpublished). 1973.

[Pa75] G. Pauletta and F.D. Brooks. *Nucl.Phys. A255 (1975) 267*

[Pe51] J.L. Perkin. *Phys.Rev. 81 (1951) 892*

[Pe79] L.J. Perkins and M.C. Scott *Nucl.Inst. and Meth. 166 (1979) 451*

[Ra88] W.D.M. Rael. *Int.J.Mod.Phys. 3 (1988) 1343*

[Sh60] R.K. Sheline and K. Wildermuth. *Nucl.Phys. 21 (1960) 196.*

[Sh70] D. Shackleton. PhD Thesis, University of Cape Town (unpublished). 1970.

[Sm86] F.D. Smit. PhD thesis (unpublished), University of Cape Town (1986).

[St76] A.P. Stevens. MSc Thesis, University of Cape Town (unpublished). 1976.

[Su83] T.S. Subramanian, J.L.Romero, F.P. Brady, J.W. Watson, D.H. Fitzgerald, R. Garret, G.A. Needham, J.L. Ullmann, C.I. Zanelli, D.J. Brenner and R.E. Prael. *Phys.Rev. C28 (1983) 521*

[Ta71] N. Takigawa and A. Arima. *Nucl.Phys. A168 (1971) 593.*

[Ta88] A. Takahashi, E. Ichimura, Y. Sasaki and H. Sugimoto. *J.Nucl.Sci. and Technol. 25 (1958) 25.*

[To88] W. Tornow. *Triangle University National Laboratory, Private Communication (1988).*

[Va58] S.S. Vasilev, V.V. Komarov and A.M. Popova. *Sov.Phys. JETP, 6 (1958) 1016.*

[Wu92] A.H. Wuosmaa, R.R.Betts, B.B. Back, M. Freer, B.G. Glagola, ThrHapp, D.J. Henderson, P. Wilt and I.G. Bearden. *Phys.Rev.Lett. 68 (1992) 1295.*

[Va67] W.T.H. Van Oers and R.W. Brockman *Nucl.Phys. A92 (1967) 561.*

[Vo68] R. Volts, H. du Pont and G. Laustrait *J.Physique 29 (1968) 297.*